Fall 2021

Alkalinity and Buffering in Estuarine, Coastal and Shelf Waters

Christopher Hunt
University of New Hampshire, Durham

ALKALINITY AND BUFFERING IN ESTUARINE, COASTAL, AND SHELF WATERS

By

CHRISTOPHER W. HUNT

M.S. Chemical Oceanography, University of New Hampshire, 2003

B.S. Chemistry, Trinity College, 2000

DISSERTATION

Submitted to the University of New Hampshire

in Partial Fulfillment of the Requirements for the Degree of

Doctor of Philosophy

in

Earth and Environmental Sciences

September 2021

This dissertation has been examined and approved in partial fulfillment of the requirements for the degree of Doctor of Philosophy in Earth and Environmental Sciences by:

Dissertation Director, Joseph Salisbury,
Research Professor of Earth Sciences

University of New Hampshire

Robert Byrne,

Distinguished University Professor of Marine Science

University of South Florida

Peter Raymond,

Professor of Ecosystem Ecology

Yale School of the Environment

Douglas Vandemark,

Research Professor of Earth Sciences

University of New Hampshire

Wilfred Wollheim

Associate Professor of Natural Resources and the Environment,

University of New Hampshire

On July 23, 2021

Approval signatures are on file with the University of New Hampshire Graduate School.

ACKNOWLEDGEMENTS

I would like to begin by giving special thanks to my dissertation committee: Doctors Douglas Vandemark, Robert Byrne, Wil Wollheim and Peter Raymond. Their support, help and guidance made this dissertation vastly better. Particular thanks and gratitude go to my advisor, Dr. Joe Salisbury, who has been my boss, supervisor, and colleague through my career at UNH, both before and after my PhD program. Joe has always been so generous in providing me with both a job and the freedom and encouragement to pursue my research interests, and this work would not exist without his support.

A huge number of people have helped me along the way. UNH colleagues Shawn Shellito, Marc Emond, Melissa Melendez, and Nate Rennels helped make all these projects run. Chris Taylor, Mark Bradley, and Katherine McGinnes from NOAA and Jeff Robinson from the Downeast Institute were invaluable contributors to fieldwork. Sherwood Liu from the University of South Florida spent time in the field and many hours in the lab figuring out the mysteries of organic alkalinity.

Finally, my family are both the inspiration for this work and the reason I could get it done. From my parents to parents-in-law to brother to aunts and uncles and cousins, everyone gave me tremendous encouragement along my way. And of course, the center of my world are my two sons Sam and Max, who gave me motivation when I needed it, and my amazing wife Jess who always believed in me and is the light of my life. I love you all!

Funding for this work was provided by several generous grants: NOAA TTP Project NA15NOS0120155- Tracking Ocean Alkalinity using New Carbon Measurement Technologies (TAACT), NOAA project NA16NOS0120023, NOAA project N18NOS0120156, NOAA project 940846421 and NSF OCE-1658377.

TABLE OF CONTENTS

LIST OF TABLES

LIST OF FIGURES

ABSTRACT

ALKALINITY AND BUFFERING IN NEARSHORE, COASTAL, AND SHELF WATERS

By

Christopher W. Hunt
University of New Hampshire

As anthropogenic climate change continues to elevate the amount of carbon dioxide (CO_2) in the Earth's atmosphere, the absorption of a large portion of this CO_2 by Earth's oceans has resulted in a steady decrease in pH. The consequent phenomenon of ocean acidification (OA) is a result of shifts in the carbonate chemistry system of the ocean- a system which can be analytically described by several factors, including total alkalinity (TA). TA in the oceans has been measured for over a century, but analytical and operational constraints have limited these measurements in time and space. Additionally, recent work has highlighted gaps in our knowledge of the species which collectively comprise TA. This dissertation describes efforts to examine TA through several novel applications: by deploying an automated TA analyzer aboard a survey vessel to map East Coast USA TA distributions, using the same analyzer in a long-term fixed coastal location to build a timeseries and examine seasonal biogeochemical dynamics, and measuring the concentrations and properties of the poorly understood organic component of TA in two Gulf of Maine estuaries.

East Coast regional distributions of salinity (S) and TA generally agreed with prior findings, but linear TA:S regressions varied markedly over time and deviated from previously developed models. This variability is likely due to a combination of biological, seasonal, and episodic influences and indicates that substantial errors of ±10-20 μmol kg^{-1} in TA estimation from S can be expected due to these factors. This finding has likely implications for numerical ecosystem modeling and inorganic carbon system calculations. New results presented in Chapter 1 provide refined surface TA:S relationships, present more data in space and time, and improve TA modeling uncertainty.

Coastal timeseries observations were collected hourly over 28 months representing all seasons between May 2016 and December 2019. Results presented in Chapter 2 indicated that endmember mixing explained most of the observed variability in TA and dissolved inorganic carbon (DIC), concentrations of which varied strongly with season. For much of the year, mixing dictated the relative proportions of salinity-normalized TA and DIC as well, but a fall season shift in these proportions indicated that aerobic respiration was observed, which would decrease buffering (β-H) by decreasing TA and increasing DIC. However, fall was also the season of weakest statistical correspondence between salinity and both TA and DIC, as well as the overall highest salinity, TA and β-H. Potential biogeochemically-driven β-H decreases were overshadowed by increased buffering capacity supplied by coastal ocean water. A simple modeling exercise showed that mixing processes controlled most monthly change in TA and DIC, obscuring impacts from air-sea exchange or metabolic processes. Advective mixing contributions, more than biogeochemically-driven

changes, are critical to observe when evaluating local estuarine and coastal ocean acidification.

Chapter 3 describes the first comparison study of both organic alkalinity (OrgAlk) distributions and acid-base properties in contrasting Gulf of Maine estuary-plume systems: the Pleasant (Maine USA) and St. John (New Brunswick CA). Four surveys of each estuary were conducted between May 2018 and October 2019. Substantial amounts of OrgAlk were measured in each estuary, whose distributions were sometimes not conservative with salinity. Two measures of OrgAlk produced consistently differing results, indicating acid-base characteristics that may be inconsistent with the definition of TA. OrgAlk and dissolved organic carbon (DOC) concentrations varied seasonally in the St. John Estuary, but not in the St. John. The fraction of TA represented by OrgAlk ranged from a maximum of 78% at low salinity in the St. John Estuary to less than 0.4% at the coastal ocean endmember. While the range of St. John OrgAlk concentrations was comparable to other studies, the St. John Estuary demonstrated a broader distribution. The acid dissociation constant (pK_a) of the estuary samples was modeled according to a combined speciation and mixing approach, while the organic carbon acid dissociation constant (pK_{DOC}) was estimated using a separate method. Results showed general agreement, but with some notable exceptions in the St. John estuary. OrgAlk modeling results from the Pleasant Estuary were more consistent than the St. John, despite St. John OrgAlk, DOC and pH results exhibiting much less seasonal variability. The mean OrgAlk pK_a was higher in the Pleasant than in the St. John, while the mean Pleasant pK_{DOC} was higher or lower than that in the St. John depending on which OrgAlk analysis approach was employed.

Application of a bulk pK_a or pK_{DOC} to model OrgAlk from more common measurements such as pH, salinity, or DOC may offer promise (as in the Pleasant), but should be undertaken with caution as variability can pose challenges (as in the St. John).

Future work should blend the analyses described in the chapters of this dissertation. For example, by collecting discrete samples aboard the survey vessel or at the coastal laboratory organic alkalinity contributions could be used to refine carbonate system calculations. Regional shifts in TA:S could be used to differentiate local and remote coastal endmember TA shifts. While this work utilized novel TA and OrgAlk analyses in three specific applications, the applicability of these analyses is broad and offers the potential to greatly enhance monitoring efforts and ecosystem biogeochemical studies.

INTRODUCTION

The work presented in this dissertation was conducted during a period of great change in the global environment, including changes in the oceans which cover more than two-thirds of the planet and provide vital ecosystem services such as food, transportation, temperature regulation, element and nutrient cycling, and recreation. Human activities have increased the amount of anthropogenic carbon dioxide (CO_2) stored in the atmosphere, leading to a cascade of effects upon Earth's ecosystems and the human population which relies on them (IPCC 2014). One of these effects is ocean acidification (OA), which results from the exchange between CO_2 in the atmosphere and CO_2 dissolved in the upper ocean, where the natural buffering provided by ocean alkalinity and resulting CO_2 absorption has led to a decrease in global upper ocean pH by about 0.002 yr^{-1} (Feely et al. 2004, Doney et al. 2011). OA poses widespread threats to aquatic flora and fauna that are just beginning to be understood.

Just as environmental changes are accumulating rapidly at the time of this writing, changes in humankind's ability to study, monitor, and perhaps remediate the effects of climate change are also accelerating. The important role of oceans- and specifically ocean alkalinity- in regulating climate has become more apparent in recent years, as oceans are estimated to have absorbed about 25% of anthropogenic carbon dioxide (CO_2) between 2006-2015 (Le Quéré et al. 2016), with higher alkalinity waters providing enhanced buffering and CO_2 sequestration. Ocean alkalinity acts as a powerful counter to anthropogenic climate change: increased alkalinity simultaneously

neutralizes the acidity generated by OA and promotes the further absorption of more atmospheric CO_2, reducing the primary driver of climate change. Vast stores of alkalinity in deep ocean waters represent more than enough neutralizing capacity to both mitigate anthropogenic ocean OA and sequester the anthropogenic atmospheric CO_2, but relatively languid ocean circulation means these stores of alkalinity will not neutralize the anthropogenic atmospheric CO_2 for thousands of years (Zeebe 2012).

In the short term, less-buffered upper ocean and coastal waters and the organisms living in them will be most susceptible to OA. But there is a converse to this vulnerability: coastal waters and the upper ocean are also sites of an opportunity to counteract both the result of anthropogenic climate change (i.e. OA) and anthropogenic climate change itself (via enhanced CO_2 absorption). An increasing amount of attention is being paid to plans to enhance upper ocean and coastal alkalinity (a process termed Ocean Alkalinity Enhancement, OAE) to simultaneously mitigate OA and sequester atmospheric CO_2 (Renforth 2017). These plans currently exist as theoretical designs or model evaluations and would require an unprecedented global effort to enact; however, climate change is an unprecedented threat requiring equally ambitious solutions. Upper ocean and coastal alkalinity in particular represent chemical systems that are sensitive to atmospheric CO_2 in ways that simultaneously offer a global acidification risk and a partial global climate solution.

Coastal areas may be especially vulnerable to the impacts of OA (Mathis et al. 2015, Breitberg et al. 2015) and important in the application of OAE; however the dynamics of OA and the buffering capacity in coastal areas are still poorly understood relative to the open ocean, due to the complex interplay between a number of additional

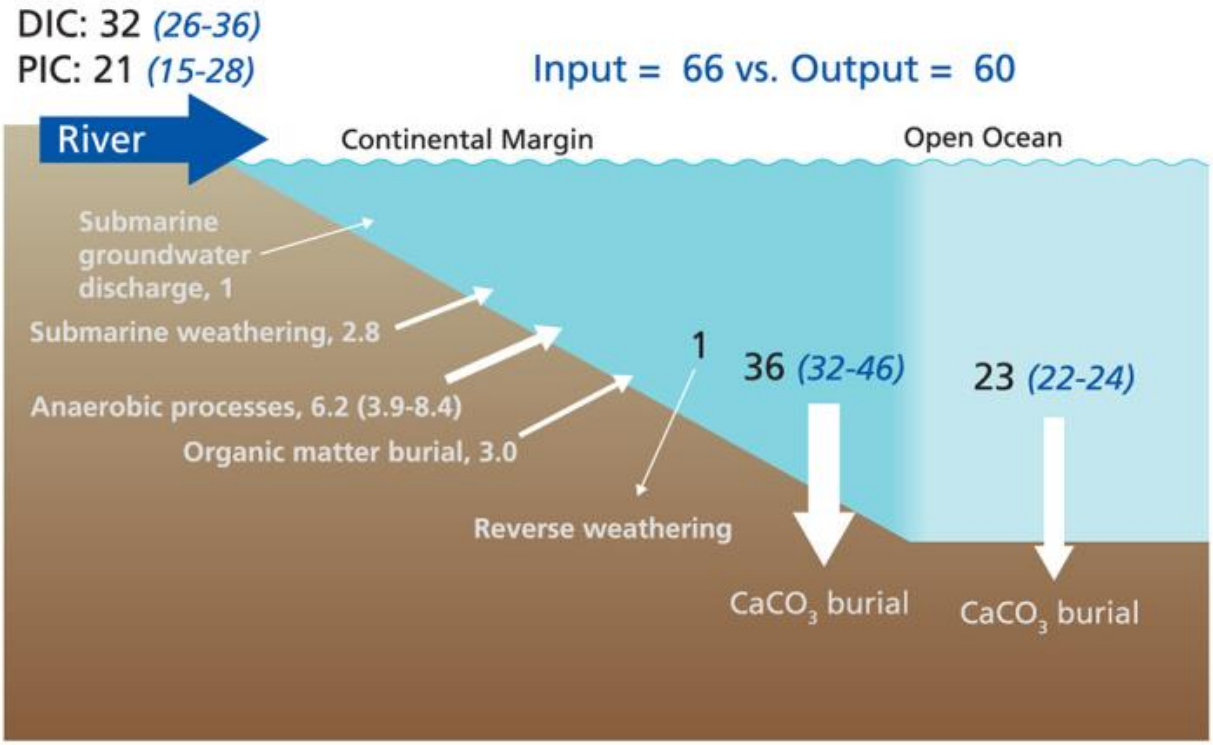

Figure 1- The ocean alkalinity balance. Note all fluxes are in Tmol C year^{-1}. From Middleburg et al. (2020).

coastal processes (Figure 1), including calcium carbonate production and dissolution (Cross et al. 2013), anaerobic alkalinity generation (Thomas et al. 2009), river inputs (Salisbury et al. 2008), organic contributions to total alkalinity (Song et al. 2020), and intertidal marsh exchanges (Wang et al. 2016). This complexity, together with the large range of variability in coastal ocean alkalinity and pH, produces substantial uncertainties in the ability to predict changes brought on by OA (Wallace et al. 2014, Hagens et al. 2015, Breitburg et al. 2015) and sensitivity of coastal ocean waters to changes in alkalinity. Figure 1 also illustrates the outside influence that coastal margins have upon the global carbon and alkalinity cycles relative to the much larger open ocean; the coastal ocean is where the dynamics are strongest and changes most difficult to anticipate.

Historically, alkalinity has been one of the most fundamental concepts in the study of the chemistry of the sea. The concept of alkalinity as the buffering capacity or acid neutralizing capacity of seawater has been used since the early 1900s (e.g., Thompson and Bonnar 1931, Mitchell and Solinger 1934), and indeed alkalinity was one of the measurements made on the first oceanographic expedition aboard the Meteor (1925-1927) by ship's chemist Herman Wattenberg. More recently, a formal chemical definition of seawater total alkalinity (TA) has been used for over thirty years with little modification (Dickson 1981, Equation 1), while measurement methods have steadily improved, especially with the introduction of a readily available Certified Reference Material which researchers can use to assess the accuracy of measurements (Dickson et al. 2003). This TA definition centers on inorganic alkalinity contributors but includes a term for organic contributors; however, these organic species and their influence on TA measurements are infrequently studied, and a refined understanding of the importance and behavior of organics is especially pressing in the coastal ocean and estuaries where watershed inputs of organics may be substantial.

For nearly two decades researchers in the Ocean Process Analysis Group at the University of New Hampshire have maintained monitoring assets and conducted sampling surveys along the coast of the Gulf of Maine and its contributing estuaries in an effort to better understand the inorganic carbon and alkalinity systems in these dynamic coastal environments. These efforts have led to insights into air-sea CO_2 exchange (Vandemark et al. 2011, Hunt et al. 2013), estuary inorganic carbon mixing (Salisbury et al. 2009), organic alkalinity distributions in coastal rivers (Hunt et al. 2011), impacts of OA on organisms (Salisbury et al. 2008) and broader Gulf of Maine coastal

OA (Salisbury and Jönsson 2018). However, a more complete understanding of coastal alkalinity and carbon chemistry, as well as changes in these factors over space and time, requires new tools and approaches.

Fortunately, recent technological developments have provided a new tool for the accurate, rapid measurement of TA. The first two chapters of this dissertation employ this new TA tool in different applications. Chapter 1 describes the collection of coastal and shelf TA data over broad spatial scales, spanning several seasons, aboard a ship of opportunity. This work led to the collection of more TA data for several East Coast regions than had ever been collected previously, and the richness of this data set allowed for the determination of shifts in regional alkalinity distributions not previously reported. The results from this study can be used to enhance the assessment of East Coast OA vulnerability, or potential for OAE.

Chapter 2 moves closer to the coast, using the same novel TA instrument to collect a years-long timeseries of TA data together with complimentary pCO_2 and other associated parameters. This unique dataset provided an unprecedented view into the alkalinity and buffering dynamics at a location situated at the confluence of land and the coastal ocean. These dynamics proved to be highly seasonal, influenced both by physical mixing and temperature changes, and potentially impacted by shifting biogeochemical processes.

Chapter 3 moves further inland yet, and departs from Chapters 1 and 2 to focus on a specific, understudied component of TA. Organic alkalinity was examined in two Gulf of Maine estuaries, to quantify both the concentrations of organic alkalinity and its

acid-base characteristics. Until a comprehensive understanding of the role of organic material in TA is achieved the use of TA data will carry increased uncertainties, especially in certain applications such as estimating pCO_2 or pH. The work contributes to the increasing evidence that organic alkalinity is nearly universally present in river, estuary, and seawater, and even in reference materials.

While these three studies describe relatively small areas of the ocean, they serve to fill knowledge gaps in the understanding of spatial alkalinity distributions along a coastal margin, time-varying changes in alkalinity and buffering at the land-ocean interface, and a potentially important component of the alkalinity system. They should serve as important pieces of the foundation of knowledge needed to measure, understand, and perhaps ameliorate the ongoing anthropogenic changes to the global environment.

VARIABILITY OF USA EAST COAST SURFACE TOTAL ALKALINITY DISTRIBUTIONS REVEALED BY AUTOMATED INSTRUMENT MEASUREMENTS

1.1 Introduction

The important role of ocean alkalinity in regulating climate has become more apparent in recent years, as oceans are estimated to have absorbed about 25% of anthropogenic carbon dioxide (CO_2) between 2006-2015 (Friedlingstein et al. 2019). Waters containing higher alkalinity concentration relative to CO_2 provide enhanced buffering and CO_2 sequestration potential. This sequestration has led to a decrease in global upper ocean pH by about 0.002 yr^{-1} (Feely et al. 2004, Doney et al. 2011), a process termed ocean acidification (OA). Vast stores of alkalinity in deep ocean waters represent more than enough neutralizing capacity to mitigate anthropogenic OA over millennial time scales (Zeebe 2012). Over decadal time scales, the less-buffered upper ocean and coastal waters, where high biological production occurs, are more susceptible to OA and its consequences. Coastal areas may be especially vulnerable to the impacts of OA (Mathis et al. 2015, Breitburg et al. 2015), but the dynamics of OA and buffering capacity in these areas are still poorly understood relative to the open ocean. This is due to the complex interplay between a number of additional coastal biogeochemical and physical processes, including biological calcium carbonate production and dissolution (Cross et al. 2013), anaerobic alkalinity generation (Thomas et al. 2009), river inputs (Salisbury et al. 2008), intertidal marsh exchanges (Wang et al. 2016), bottom-water acidification from metabolic CO_2 accumulation (Cai et al. 2011,

Mucci et al. 2011), as well as cross-shelf exchange (Chen and Wang 1999). These processes, combined with the large range of variability in coastal ocean alkalinity, pH, and hydrography, can lead to substantial uncertainties in ecosystem models used to predict future OA impacts in these areas (Wallace et al. 2014, Hagens et al. 2015, Breitburg et al. 2015).

TA and dissolved inorganic carbon (DIC) distributions along the United States East Coast ocean margin (henceforth shortened to East Coast) have been extensively studied during several transects, including the four GOMECC (Gulf of Mexico and East Coast Carbon) and ECOA (East Coast Ocean Acidification) cruises (Cai et al. 2010, Wang et al. 2013, Wanninkhof et al. 2015) and the Ocean Margins Program in the MAB (Chipman et al. 1995). These ongoing surveys provide a synoptic view of conditions in the region, but they were confined to the summer season, were resource- and labor-intensive, and were spaced several years apart. Methods that can expand temporal and spatial coverage of inorganic carbon system parameters would greatly enhance model estimates of East Coast DIC and CO_2 exchange (Signorini et al. 2013).

Recent developments in both ocean observation and data synthesis efforts offer the promise of vastly improved East Coast TA and inorganic carbon estimates. In-situ data compilations such as GLODAP (Olsen et al. 2016, Key et al. 2015) provide extensive collections of in-situ TA, DIC, and pH measurements. These datasets have been used to construct statistical relationships between TA and practical salinity (hereafter referred to as “salinity” in this work and abbreviated as “S”) and sometimes temperature for major ocean basins (Lee et al. 2006, Millero et al. 1998, Takahashi et al. 2014), smaller sub-basins (Takahashi et al. 2014, Jiang et al. 2014, Cross et al.

2013), and even segmented coastal areas (DeGrandpre et al. 1997, Cai et al. 2010, Joesoef et al. 2017). In particular, Millero et al. (1998) presented an 'Atlantic' relationship assembled using surface data from 60°S to 80°N, whereas Lee et al. (2006) presented a 'North Atlantic' relationship using data from 30°N to 80°N.

These relationships have been used to estimate TA from either *in situ* salinity observations, salinity climatologies (Zweng et al. 2019), or space-based satellite measurements (Signorini et al. 2013, Fine et al. 2017, Salisbury and Jönsson 2018, Land et al. 2019, Reul et al. 2020). Satellite missions offer the potential for synoptic salinity estimates over vast spatial scales (Salisbury et al. 2015, Grodsky et al. 2018), which can then be used to derive estimates of surface ocean TA. The statistical relationships used to produce these estimates are, however, regionally and temporally variable (e.g., Land et al. 2019, Cai et al. 2010, Li et al. 2020). An additional source of high-quality TA data for the USA East Coast, collected at a higher frequency than the three-to-five year interval of the previous GOMECC/ECOA cruises, could inform the temporally variable nature of regional relationships. Recent technological advances and development efforts have provided a commercially available tool for this purpose: an automated TA analyzer (the CONTROS HydroFIA® TA, -4H-JENA Engineering GmbH, Jena, Germany, formerly of Kongsberg Maritime Contros GmbH, Kiel, Germany, hereafter referenced as HydroFIA TA). Deployed aboard a ship of opportunity, the collected underway surface TA measurements allow us to re-examine regional TA distributions along the East Coast and test existing statistical models relating salinity to TA. Here, we evaluate the performance of the HydroFIA TA instrument on multiple cruises aboard a ship of opportunity, present recommendations for future deployments,

compare findings to previous studies as well as to a newly-assembled database of historical East Coast TA measurements, and discuss how data collected during this effort help to inform our understanding of TA variability along the East Coast.

1.2 Methods

1.2.1 Study Regions

This study reports on observations from four East Coast oceanographic regions: Gulf of Maine, Nantucket Shoals/George's Bank, Middle Atlantic Bight, and offshore Shelf Break Front (Figure 1.1). Delineations of the boundaries between these regions follow the methods of Signorini et al. (2013) and Hofmann et al. (2008). The Gulf of Maine (GOM, Figure 1.1) is a highly productive, semi-enclosed shelf sea, encompassing the area between Cape Cod in Massachusetts and the Canadian province of Nova Scotia. The area east of the Scotian shelf and also east of the more northern Newfoundland and Labrador shelf system is where the warm, salty, northeast-flowing Gulf Stream and the colder, fresher, southwest-flowing Labrador Current interact (Loder et al. 1998). GOM circulation is typically cyclonic, with upstream Scotian Shelf and Atlantic slope water entering the region through the Northeast Channel and across the western Scotian Shelf, following the Maine coast southward, and exiting the GOM around the eastern flank of George's Bank and the Great South Channel between the Nantucket and George's Bank shoals. The area of George's Bank and Nantucket Shoals (GBN) comprises two shallow regions which together geographically separate the GOM from the Middle Atlantic Bight, bisected north-to-south by the Great South

Channel. This region supports an active commercial fishery. The Middle Atlantic Bight (MAB) extends roughly from Cape Cod in Massachusetts to Cape Hatteras in North Carolina. This area also resides at the intersection of two major ocean currents: the colder, fresher inshore modified Labrador coastal current from the north (flowing first through the GOM and GBN regions) and the warmer, saltier offshore Gulf Stream from the south (Wang et al. 2013). These two currents are separated by the inshore shelf areas and slope sea further offshore, which stretches from Cape Hatteras to the Grand Banks. Warm core rings, shed from the Gulf Stream into the slope sea, are a frequent source of warm, high salinity water to the MAB region via cross-shelf exchange (Hofmann et al. 2008). The MAB is characterized by springtime phytoplankton blooms and low pCO_2 during the winter and spring months (DeGrandpre et al. 2002, Wang et al. 2013). The offshore Shelf Break Front (SBF) region delineates a band of slope sea stretching from south of Cape Hatteras northeastward nearly to Nova Scotia, encompassing the area where the seafloor deepens from several hundred meters to more than 2000 m, and forming a boundary region between the inshore GOM, GBN and MAB regions and the offshore slope sea.

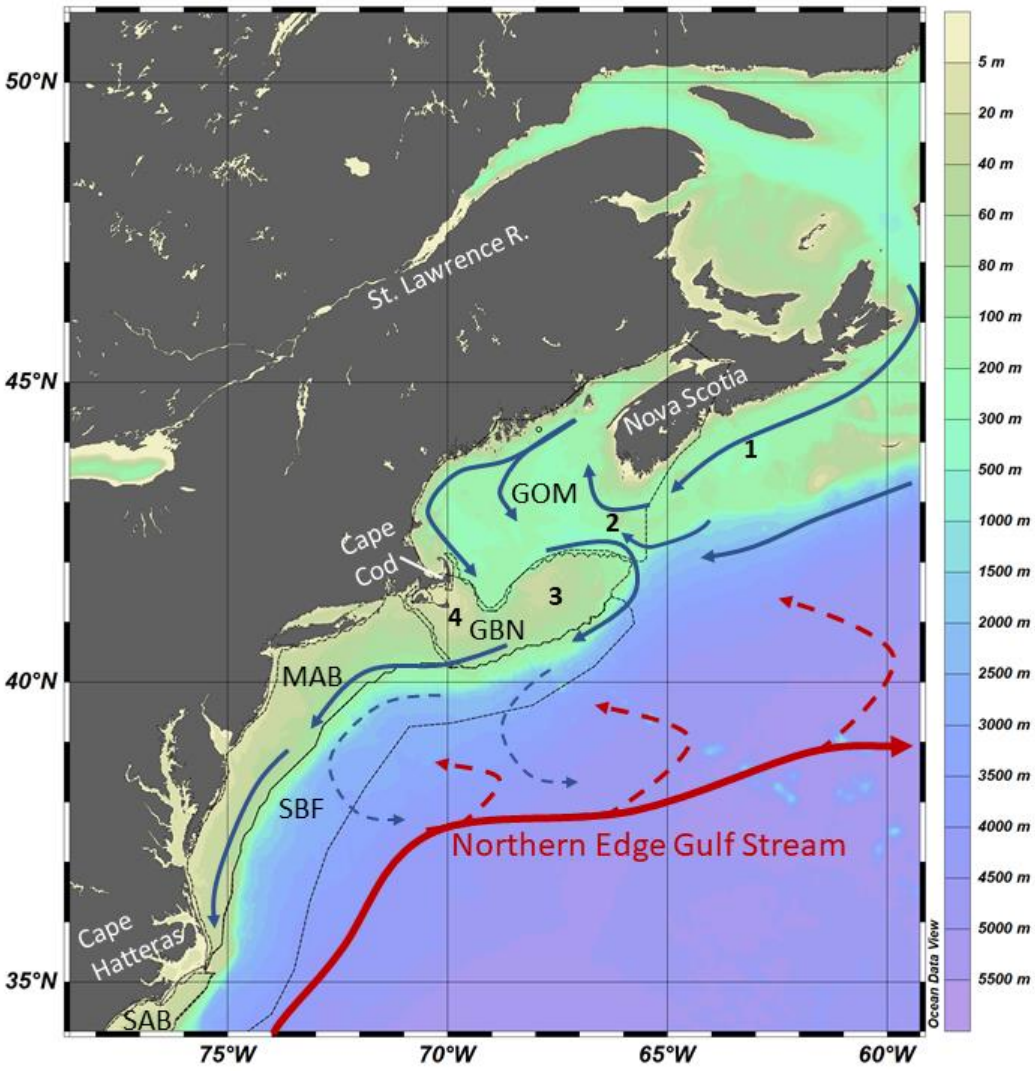

Figure 0.1: Study area map with bathymetry, adapted from Townsend et al. (2006), with study subregions outlined. The study subregions are the Gulf of Maine (GOM), George's Bank/Nantucket Shoals (GBN), Middle Atlantic Bight (MAB), and Shelf-Break Front (SBF). The South Atlantic Bight (SAB) region is also shown south of Cape Hatteras. Numbers indicate specific locations found in the text: 1: Scotian Shelf; 2: Northeast Channel; 3: George's Bank; 4: Great South Channel. General positions of major currents are shown as red and blue arrows. The position of the Gulf Stream's northern edge is approximate, dashed red and blue arrows show the presence of cross-shelf mixing and not locations of actual currents.

1.2.2 Analytical Methods for Practical Salinity, Water Temperature, and pCO_2

Measurements in 2017 were collected on seven cruises of opportunity aboard the National Oceanic and Atmospheric Administration (NOAA) Ship *Henry B. Bigelow* (hereafter referred to as the *Bigelow*), a 64-meter fisheries research vessel. A summary of these cruises is provided in Table 1.1. Surface seawater temperature and practical salinity (hereafter referred to as salinity) were measured from a continuous surface seawater supply (intake depth about 3 m) using a Seabird SBE-45 thermosalinograph (Sea-bird Electronics, Bellevue WA, manufacturer precision of ±0.0001°C and ±0.0002, respectively). Measurements of the partial pressure of carbon dioxide (pCO_2) were made from the same continuous surface seawater supply using a General Oceanics (Miami, FL) pCO_2 measurement system operated by the NOAA Atlantic Oceanography and Meteorological Laboratory (AOML), with a measurement accuracy of 2 µatm, as detailed in Pierrot et al. (2009).

Table 1.1: Cruise summaries for the 2017 and ECOA-2 efforts, all aboard the NOAA Ship Henry B. Bigelow.

	Dates	Cruise Duration (days)	Latitude Range (°N)	Longitude Range (°W)	n TA observations	TA Range (µmol kg-1)	Salinity Range	T Range (degrees C)
Cruise 1	Feb 11 - Feb 22, 2017	12	37.15 - 42.51	-75.67 - -65.42	1585	2136 - 2356	31.46 - 36.08	2.495 - 14.969
Cruise 2	Mar 7 - Mar 22, 2017	16	34.43 - 40.32	-76.29 - -72.76	1575	1888 - 2400	22.97 - 36.55	4.765 - 24.003
Cruise 3	Mar 28 - Apr 6, 2017	10	39.04 - 41.48	-74.01 - -70.51	1544	2068 - 2332	30.11 - 34.88	3.728 - 11.209
Cruise 4	Apr 12 - Apr 26, 2017	15	39.93 - 42.68	-71.38 - -65.76	1679	2171 - 2294	31.49 - 34.83	2.1483 - 11.211
Cruise 5	May 5 - May 11, 2017	7	42.64 - 44.39	-70.74 - -66.57	536	2169 - 2217	31.2 - 32.52	4.504 - 8.167
Cruise 6	Jun 10 - Jun 22, 2017	13	40.62 - 44.23	-70.72 - -65.86	897	2156 - 2262	30.84 - 35.28	9.010 - 15.044
Cruise 7	Jul 6 - Jul 19, 2017	14	39.20 - 41.76	-73.38 - -65.27	1134	2156 - 2274	31.02 - 36.58	11.317 - 25.457
ECOA-2	Jun 26 - Jul 29, 2018	34	26.81 - 45.01	-80.98 - -61.4	1656	2001 - 2403	26.61 - 36.42	6.38 - 31.77

1.2.3 Discrete TA Sample Collection and Analysis Methods

Discrete samples for independent instrument evaluation were collected from the ship's underway seawater supply on two cruises and analyzed by two laboratories. Samples from Cruise 1 in 2017 were collected and analyzed by the NOAA Atlantic Oceanographic and Meteorological Laboratory (AOML). Samples during the 2018 ECOA-2 cruise were analyzed by the laboratory of Dr. Wei-Jun Cai (University of Delaware, referred to hereafter as U.Del.). Water from the shipboard seawater supply was transferred without bubbling into previously-flushed 500 mL (AOML) or 250 mL (U.Del.) glass BOD bottles with greased stoppers. These were filled to leave less than 1% headspace in the bottle. Samples analyzed by AOML were preserved with 200 µl of saturated mercuric chloride solution and analyzed several weeks later; those analyzed by U.Del. were unpreserved and analyzed within 24 hours. A detailed description of the AOML TA analysis is provided by Barbero et al. (2017), specific analysis details for AOML Cruise 1 samples are described by AOML (2020), and U.Del. methods are described by Cai et al. (2010). Briefly, each lab performed open-cell titrations, measuring the e.m.f. during titration via glass pH electrodes, with results calibrated via comparison to certified reference material. AOML titrations were performed with 0.2N hydrochloric acid (HCl) prepared in a 0.55 molal NaCl solution. U.Del. titrations were performed with 0.1N HCl in a 0.5 molal NaCl solution. The TA endpoint of the titrations were determined according to calculation of the Gran function (Gran 1952) with a nonlinear least squares correction for the presence of sulfate and fluoride ions (Dickson

et al. 2007). AOML and U.Del. instrument performance statistics are discussed below and presented in Table 1.2.

1.2.4 Analytical Method for Underway Total Alkalinity

Total Alkalinity (TA) was measured using a CONTROS HydroFIA® TA analyzer (Aßmann et al. 2013, Seelmann et al. 2019), modified for regular automated reference measurements as described below. Seelmann et al. (2019) provide a comprehensive account of instrument theory, design, and operation, and include extensive technical details we will not repeat here. Briefly, the HydroFIA TA instrument performs a single-point titration of seawater with 0.1N hydrochloric acid prepared in deionized water, using bromocresol green (BCG) as the indicator for spectrophotometric pH detection, a technique developed by Yao and Byrne (1998) and refined by Li et al. (2013).

As part of the NOAA/OTT TAACT project (Tracking Ocean Alkalinity using New Carbon Measurement Technologies), the HydroFIA TA instrument was improved to allow for the automated, periodic measurement of certified reference material (CRM) by adding CRM input and exhaust ports, liquid switching valves, and a digital controlling device connected to an external computer (Appendix Figure A1). This capability is now a standard feature of the commercial version of the instrument. The CRM was obtained from the Scripps Institute of Oceanography laboratory of Dr. Andrew Dickson (Dickson et al. 2003), and its regular measurement supported assessments of instrument stability and accuracy over the course of multi-week deployments. Triplicate CRM measurements were typically made each day, while underway seawater TA

measurements were made every 10-15 minutes. A customized software program controlled the HydroFIA TA instrument by switching between seawater and CRM sample streams, starting and stopping HydroFIA TA analysis, collecting salinity, water temperature, and location data from the ship's centralized data system, supplying real-time salinity to the HydroFIA TA analyzer, and emailing data to shoreside researchers. The HydroFIA TA instrument was serviced by NOAA personnel between each cruise, who replaced the supplies of HCl and BCG, refilled the 2l CRM reservoir (which was stoppered to limit evaporation), and re-calibrated the instrument with CRM. After these steps, the instrument was placed in standby mode until the *Bigelow* was underway, at which time a shipboard technician used the customized software program to begin data collection.

1.2.5 Filtration of Underway Seawater for Total Alkalinity Analysis

Unfiltered seawater was supplied to the HydroFIA TA instrument for the first five cruises. This resulted in a steady increase in pH readings and corresponding TA readings using the same batch of CRM, presumably due to fouling of the instrument's optical cell. CRM absorbance spectra over these cruises showed decreased BCG absorbances at the isobestic point over time, which were closely correlated with increased CRM TA concentration. As the CRM TA concentration and volumes of BCG and HCl added did not change over time, we believe that accumulation of material on the optical cell resulted in increased absorbance at the indicator wavelengths. A blank spectrum measurement is made before BCG and HCl addition, and subtraction of this blank resulted in decreased calculated BCG absorbance as the blank absorbance

increased. Drifts in the HydroFIA TA instrument have been observed by other investigators (Seelmann et al. 2019). CRM measurements from Cruises 1-5 showed clear, steady instrument drift of up to 93 µmol kg^{-1} by the end of Cruise 2, or a drift of nearly 3 µmol kg^{-1} per day (Appendix Figure A.2, Table A.1). After the fifth cruise an inline cross-flow filter (0.2 µm) connected to a small 50 mL reservoir for filtered seawater was installed which eliminated the instrument drift during Cruises 6 and 7. The HydroFIA TA sample analysis time was 10 minutes, and flow rate supplied to the filter had to be adequate to replenish the reservoir within the analysis time frame. The cross-flow filter (currently supplied by 4H-JENA engineering GmbH, Jena, Germany, formerly Kongsberg Maritime Contros GmbH, Kiel, Germany) uses tangential flow filtration, where unfiltered seawater flowed continuously across the filter surface (in this case, a series of tubes of filter material) at positive pressure, with filtrate moving through the walls of the tubes and collected in a reservoir for analysis. This method allowed the same filter to be used for all subsequent cruises.

To account for instrument drift over the first five cruises, the differences between the CRM TA concentration and the mean of periodic triplicate instrument CRM readings were linearly interpolated; the interpolated CRM difference corresponding to each individual TA measurement was then retrieved from the HydroFIA TA timestamp and subtracted from the observed reading.

1.2.6 Statistical Calculations

In order to evaluate the performance of the HydroFIA TA instrument and reference titration systems from two laboratories, several statistical quantities were calculated following the approach of Seelmann et al. (2019). Complete descriptions and equations are presented in the Supplementary Material. Briefly, five statistical parameters will be discussed. First, precision (σ) was determined as one standard deviation of repeated measurements of certified reference material (CRM). Second, instrument accuracy (or also the uncertainty between two measurement methods, such as HydroFIA TA and laboratory TA measurements) was determined as the root mean square error (*RMSE*) of either repeated CRM measurements relative to the certified CRM TA or the difference between paired TA analyses. Third, the uncertainty in instrument bias, *u(bias)*, incorporates the instrument *RMSE* and the known uncertainty of the certified TA of the CRM. Fourth, the combined method uncertainty, *uc*, incorporates *u(bias)* together with σ. Finally, the overall uncertainty between two TA measurement methods, such as HydroFIA TA and laboratory TA analyses, including factors such as replicate uncertainty and unknown uncertainties, is presented as $u_{c(HydroFIA\ TA,\ B)}$.

1.2.7 HydroFIA TA Analyzer and Discrete Sample Uncertainty Evaluation

Triplicate periodic CRM measurements were automatically made on a roughly daily interval by the HydroFIA TA while underway during each cruise, permitting an assessment of precision (σ, Equation 1). The CRM used in 2017 was Batch 159. For

Cruises 1-5, the σ of triplicate CRM measurements ranged from ±0.2 to ±9.2 µmol kg^{-1}, with a mean σ of ±2.0 µmol kg^{-1}. Addition of the filter resulted in no substantial change in the σ of CRM measurements for Cruises 6 or 7 in 2017 (mean CRM σ ±0.8 and ±1.8 µmol kg^{-1}, respectively). Accuracy of the HydroFIA TA during Cruises 1 through 7 in 2017, determined as the RMSE of periodic CRM readings which were corrected as described above, ranged from ±1.0 to ±3.8 µmol kg^{-1} with a mean value of ±2.2 µmol kg^{-1}. These precision and accuracy levels matched or exceeded those given by the manufacturer (±2 and ±5 µmol kg^{-1}, respectively).

Discrete TA samples were collected on two cruises from the same underway seawater supply sampled by the HydroFIA TA (Table 1.2). AOML measurements of CRM Batches 129 and 144 resulted in an uncertainty (u_c) of ±2.8 µmol kg^{-1}. Analysis of duplicate seawater samples returned an AOML sampling uncertainty, u(rep), of ±5.2 µmol kg^{-1}. The RMSE of paired AOML-HydroFIA TA analyses was ±7.0; solving Equation 5 resulted in an estimated contribution of ±2.9 µmol kg^{-1} of 'other' uncertainty to the total uncertainty between AOML and HydroFIA TA measurements, beyond the combined uncertainties of instrument precisions, biases, CRM uncertainties, and sampling or replicate uncertainties.

Table 1.2: Analytical uncertainties of paired discrete bottle sample and HydroFIA TA analyses. Paired sampling was conducted during Cruise 1 (Feb 11-22, 2017) and the 2018 ECOA-2 cruise. Discrete TA analyses were performed by two laboratories: the NOAA Atlantic Oceanographic and Meteorological Laboratory ("AOML") and the laboratory of Dr. Wei-Jun Cai at the University of Delaware ("U.Del."). AOML analyses used CRM Batches 129 and 144; U.Del. used Batch 173. The HydroFIA CRM was Batch 159 in 2017 and 173 during ECOA-2. AOML samples were preserved and analyzed three weeks after Cruise 1, U.Del. samples were not preserved and analyzed on board within 24 hours of collection.

	2017 Cruise 1	ECOA-2
Analyzing laboratory	AOML	U.Del.
σ (CRM)	±2.0	±1.2
RMSE (CRM)	±1.8	±1.2
u(CRM)	±0.52	±0.64
$u(bias)_{CRM}$	±1.9	±1.4
u_c	±2.8	±1.8
RMSE (rep)	±5.6	±1.5
u(rep)	±5.2	±0.9
n_{CRM},n_{rep}	10,9	81,27
σ (HydroFIA CRM)	±2.0	±1.4
RMSE (HydroFIA CRM)	±1.3	±3.8
u (HydroFIA CRM)	±0.59	±0.64
u(bias) HydroFIA	±1.4	±3.9
$u_{c\ (HydroFIA)}$	±2.4	±4.1
n	9	25
RMSE, paired samples	±7.0	±10.3
u(other), paired samples	±2.9	±9.2

The calculations described above were used to compare HydroFIA TA results to those measured onboard by U.Del. during the 2018 ECOA-2 cruise (Table 1.2). U.Del. analyses of CRM Batch 173 showed a low overall method uncertainty (u_c) of ±1.8 µmol kg^{-1} and very good agreement between replicate samples, with a u(rep) of ±0.9 µmol kg^{-1}. Despite an overall HydroFIA TA u_c similar to that from Cruise 1 in 2017 (±4.1 µmol kg^{-}

^{1}, from triplicate measurements of CRM Batch 173), the RMSE between HydroFIA TA and U.Del. measurements was a relatively high ±10.3 µmol kg^{-1}, with a u(other) of ±9.2 µmol kg^{-1}.

HydroFIA TA performance was consistent within ±2 µmol kg^{-1} across cruises, making it challenging to attribute the difference in u(other) between Cruise 1 in 2017 and ECOA-2. Possible factors contributing to u(other) could be the choice to preserve (AOML) or not preserve (U.Del.) discrete samples, the timing of discrete sample collection relative to the intake of sample by the HydroFIA TA, nonlinearity of the HydroFIA TA instrument drift as documented by Seelman et al. (2019), or variable effects of the presence of titratable organic species dependent on the TA analysis method used. It is important to note that organic species represent an unknown but potentially significant contributor to TA (Yang et al. 2015, Kuliński et al. 2014, Fong and Dickson 2019). Neither the HydroFIA TA analyzer nor typical discrete TA titrations are capable of distinguishing organic alkalinity contributions, which may exert a variable influence depending on the acid-base characteristics of the organic species and the TA analysis method employed (Sharp and Byrne, 2020). This topic requires further examination, but for this work we will discuss TA as the inorganic system conforming to the definition set by Dickson (1981).

1.2.8 Data Analysis

Linear regression analysis of TA against salinity was performed using an iteratively weighted least-squares algorithm with a bisquare weighting function (tuning

constant 4.685) and robust fitting options enabled (*fitlm* in Matlab®, Mathworks, Natick MA USA). The robust fitting identified outliers as any point outside 1.5 times the interquartile above or below the 75th or 25th percentile, respectively, and outliers were excluded from the calculation of the r^2 statistic. This outlier analysis excluded outliers at roughly the 10th and 90th percentiles. The regression analysis returned two linear coefficients: the change in TA per unit salinity (i.e., slope, designated "TA:S" hereafter) and the TA calculated at salinity zero (i.e., intercept, designated "TA^0"). All regional and seasonal TA:S regressions were statistically unique according to one-way ANOVA tests, with p-values less than 0.05. Other studies (i.e., Lee et al., 2006) used a second-order polynomial regression with both salinity and temperature as independent input variables, but this approach yielded worse RMSE statistics for our data (results not shown), and we have chosen to use the linear regression approach described above. Data were divided into seasons according to the following: winter (December, January, February), spring (March, April, May), summer (June, July, August), and fall (September, October, November).

1.2.9 Historical Data

To compare the results from this work to past observations in these regions, a historical dataset was assembled. Datasets used in this compilation included several categories: ship-of-opportunity measurements obtained from NOAA's AOML, data from the GOMECC-1 and -2 and ECOA-1 East Coast surveys, newly-available data from Fisheries and Oceans, Canada (DFO), the global-scale GLODAPv2 (2019) synthesis product, and data from the Ocean Margins Project (OMP) in the MAB. The earliest TA

observations made in the four study regions discussed in this work were from 1967, with the number of observations increasing steadily to the present, and with occasional years-long periods having no observations. The dataset contains over 11,000 surface measurements at depths of 10 m or less.

1.3 Results and Discussion

HydroFIA TA measurements were collected on seven *Bigelow* cruises between February 11, 2017 and July 19, 2017 (Figure 1.2), resulting in a total of 8,950 surface seawater TA measurements (Table 1.1) and 167 CRM validation measurements. The same HydroFIA TA instrument used in 2017 aboard the *Bigelow* was also deployed during the 2018 ECOA-2 cruise, for 28 days in July and August 2018, collecting a total of 1,656 TA and 75 CRM validation measurements. The 2018 ECOA-2 cruise occupied the same regions as the 2017 cruises (Figure 1.2) and included a much more spatially comprehensive survey of the SAB region. To exploit the large number of new measurements made by the HydroFIA TA instrument, we examine the data obtained during the deployments aboard the *Bigelow* in the context of previously published analyses of TA distributions, and use these new observations to examine published relationships relating TA to sea surface salinity. We also re-evaluate data from other broad-scale data collections efforts in these regions. These comparisons are not meant to show that one dataset provides a better or worse understanding of TA conditions relative to another; rather, they are meant to show that TA conditions are dynamic in these coastal zones, and the capability provided by the largely unsupervised

deployment of the HydroFIA TA system can help fill in knowledge gaps regarding seasonal and regional dynamics in ways that episodic research cruises collecting a necessarily limited number of discrete water samples cannot.

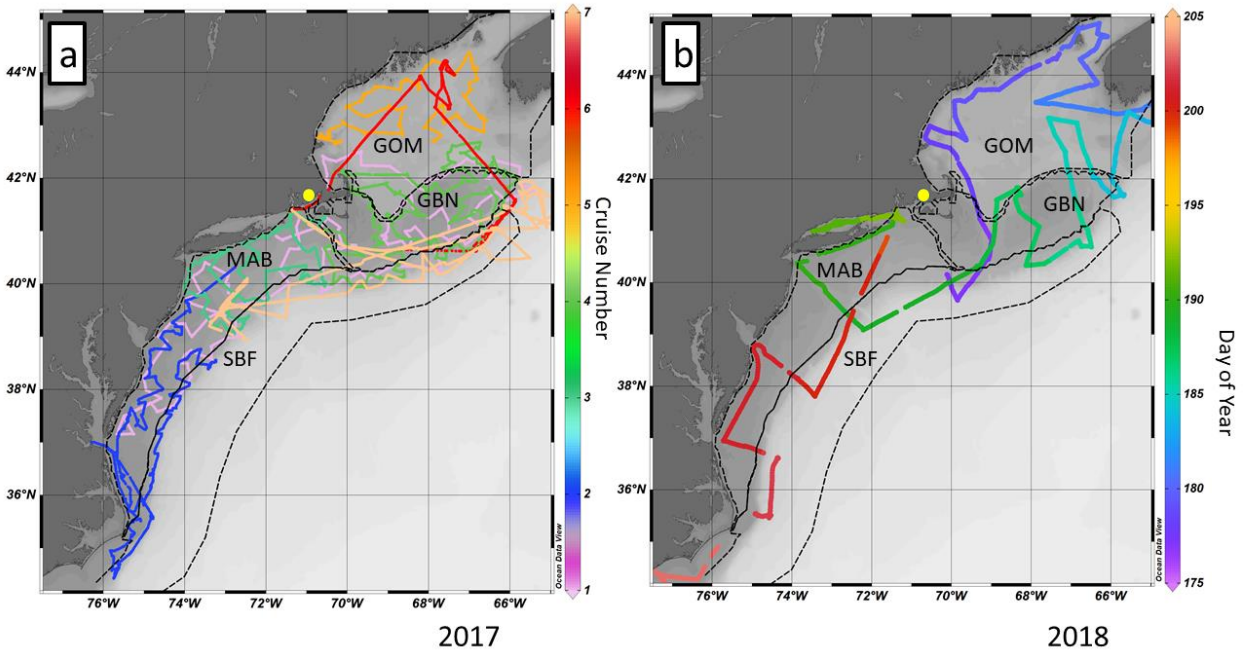

Figure 0.2: Map of 2017 (panel a) and 2018 (panel b) cruise tracks presented in this work with East Coast regions outlined. Note that colors in panel a identify the cruise number (see Table 1.1), while colors in panel b indicate day-of-year. The NOAA Ship *Henry B. Bigelow*'s home port of Newport Rhode Island USA is shown as a yellow circle. A summary of these cruises is provided in Table 1.1.

Salinity, water temperature, and TA generally increased from north to south in 2017, as upstream Scotian Shelf water feeds a coastal current flowing southward through the GOM and GBN regions to the MAB region, while gradually being modified by interactions with local rivers and offshore SBF water masses (Figures 1.3 and 1.4, Table 1.3). Salinity and TA were lowest closer to shore and increased with distance from the coast in the GOM, GBN and MAB regions. The SBF region extends seaward

from the outer boundary of each of the other regions, and was generally warmer, saltier, and higher in TA than the more shoreward regions. The SBF region contains a combination of slope water modified by interaction with the southward-flowing coastal shelf water along the boundary lines between the MAB, GBN and GOM regions (Dupont et al. 2006).

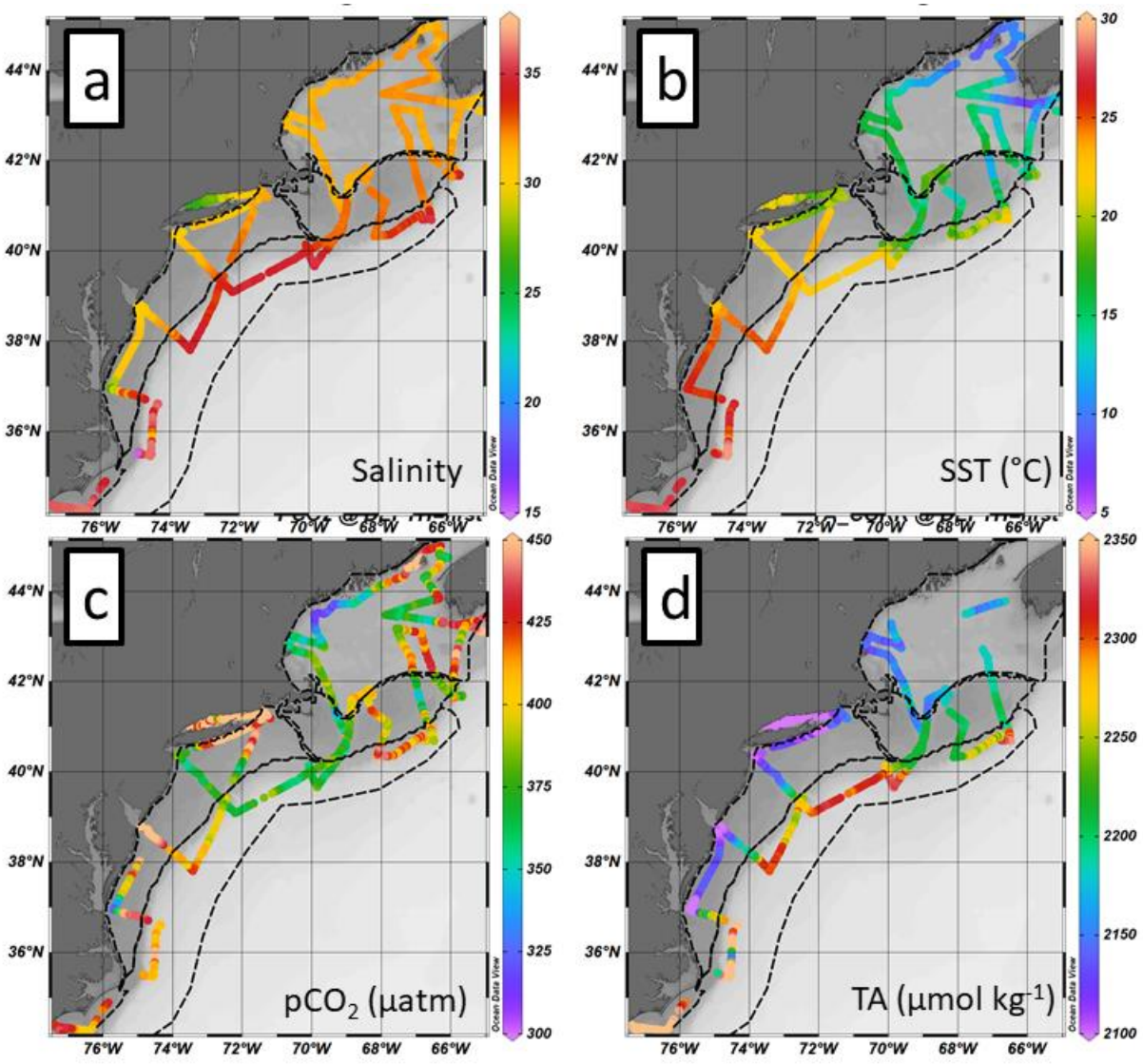

Figure 0.3: Maps of all surface data collected underway in 2017. Parameters shown are sea surface salinity (panel a), temperature (panel b, degrees Celsius), pCO_2 (panel c, µatm), and HydroFIA TA (panel d, µmol kg^{-1}). Black lines represent regional boundaries,

see text and Figure 1.1. Color bars correspond to the data point colors in each panel and are scaled identically to those in Figure 1.4.

The increasing north-to-south trend in salinity, water temperature and TA was generally repeated in 2018, but the MAB region was an exception to this trend, as the MAB mean salinity (31.19±1.07) and TA (2132±43 μmol kg^{-1}) were both lowest among the studied regions (Table 1.3). The ECOA-2 cruise made a shore stop in the MAB region, and the low-salinity data recorded outside the Newport News harbor mouth contributed to the low mean values (Xu et al. 2017). Nonetheless, even when these nearshore data are excluded the mean salinity and TA were still the lowest among the regions.

Table 1.3: Regional summary statistics for 2017 and ECOA-2 data. In order, the data presented for each parameter (e.g., salinity, temperature) are: the regional range of each observation type (minimum and maximum), the statistical mean, one standard deviation around the mean, and total number of measurements in each region. The mean, standard deviation, and measurement number are grouped in parentheses. Results from the 2018 ECOA-2 cruise are in shaded rows. Bold values indicate the highest and lowest values observed for each parameter in 2017 and 2018.

	Dates	Salinity	Temperature (degrees C)	pCO2 (µatm)	TA (µmol kg^{-1})
GOM	Feb 19 - Jun 21, 2017	**24.13** - 33.68 (31.95±0.85 n=2244)	2.87 - 14.54 (8.30±3.26 n=2271)	229 - 448 (335±43 n=1546)	2154 - 2258 (2196±15 n=1857)
GOM	Jun 27 - Jul 7, 2018	30.94 - 32.34 (31.72±0.31 n=497)	**6.37** - 18.91 (13.17±2.96 n=497)	310 - 457 (390±33 n=484)	2112 - 2213 (2158±18 n=185)
GBN	Feb 16 - Jul 19, 2017	31.12 - 33.57 (32.75±0.42 n=1451)	**2.15** - 20.94 (7.96±3.87 n=1460)	202 - 564 (346±54 n=1353)	2166 - 2267 (2211±16 n=1196)
GBN	Jun 26 - Jul 8, 2018	31.48 - 32.80 (32.46±0.33 n=212)	10.14 - 18.71 (15.74±1.87 n=212)	333 - 441 (378±16 n=201)	2146 - 2225 (2204±17 n=196)
MAB	Feb 11 - Jul 19, 2017	28.99 - 35.04 (32.98±0.85 n=3285)	3.73 - **25.45** (9.18±6.16 n=3288)	255 - **599** (331±36 n=3009)	**2087** - **2400** (2225±31 n=2699)
MAB	Jul 8 - Jul 20, 2018	**26.61** - 33.47 (31.19±1.07 n=219)	17.85 - 26.28 (22.23±2.38 n=219)	**307** - **534** (421±52 n=189)	**2001** - 2257 (2132±43 n=193)
SBF	Feb 12 - Jul 18, 2017	31.26 - **36.55** (33.76±1.12 n=2564)	4.85 - 25.19 (13.57±6.1 n=2570)	**196** - 437 (352±42 n=2353)	2183 - 2397 (2247±44 n=2116)
SBF	Jun 26 - Jul 21, 2018	30.77 - **36.20** (34.08±1.06 n=353)	14.37 - **29.14** (22.49±3.1 n=353)	352 - 480 (398±27 n=325)	2138 - **2389** (2285±50 n=325)

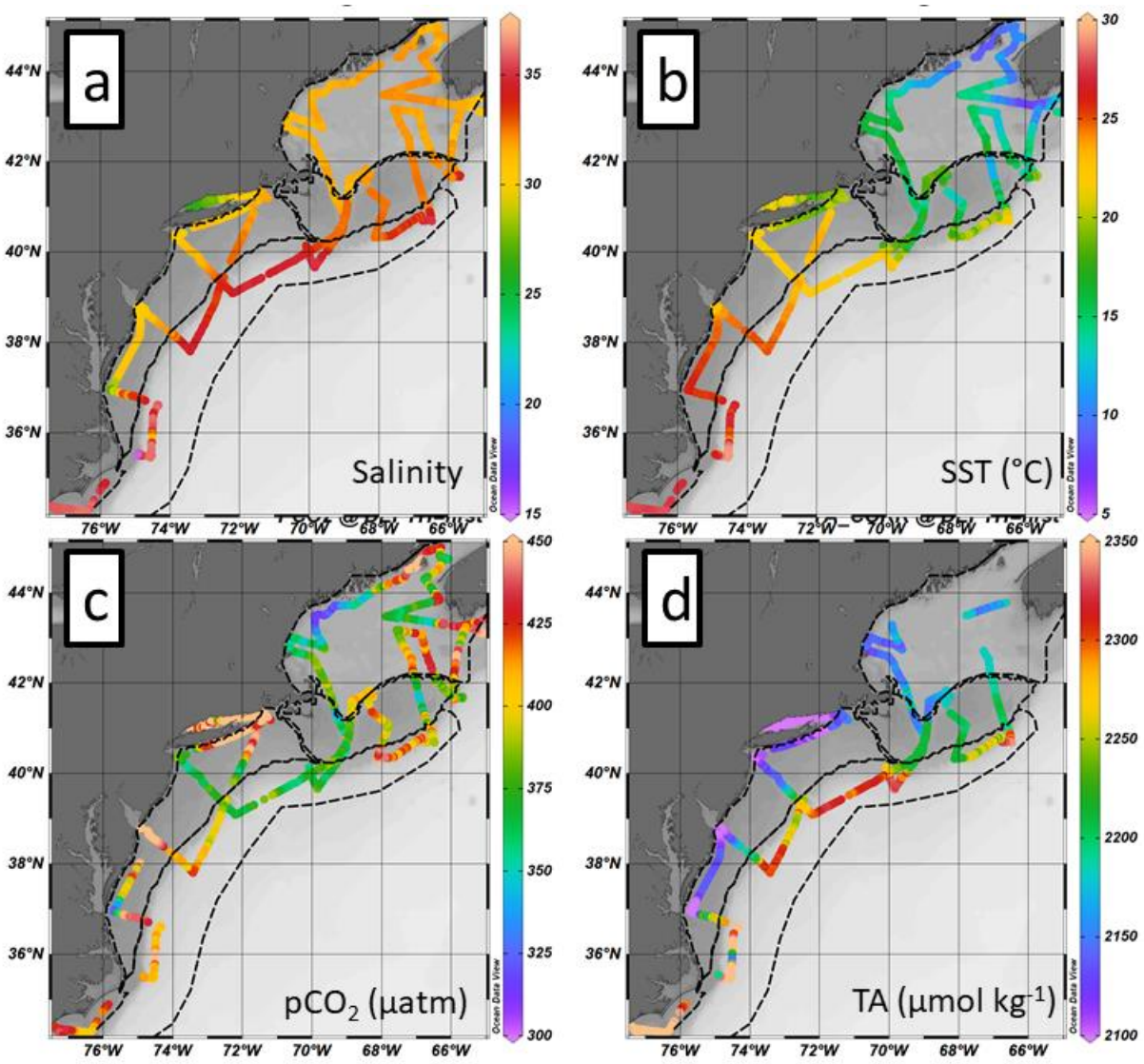

Figure 0.4 Maps of ECOA-2018 sea surface salinity (panel a), temperature (panel b, degrees Celsius), pCO_2 (panel c, µatm), and HydroFIA TA (panel d, µmol kg^{-1}). Black lines represent regional boundaries, see text and Figure 1.1. Color bars correspond to the data point colors in each panel and are scaled identically to those in Figure 1.3. The low-salinity, low-alkalinity data shown in Long Island Sound do not fall within the bounds of the regions discussed in this study, and thus do not influence the discussion of regional findings.

In contrast, seawater pCO_2 showed no clear regional pattern, and was almost always undersaturated or at near equilibrium with respect to the atmospheric CO_2 partial pressure (Table 1.3). Atmospheric pCO_2 measured by the shipboard AOML

system averaged 412±6 µatm. To test for significant differences among regional observations, we employed two-sample t-tests ('ttest2' in Matlab®, Mathworks Inc., Natick MA, USA), at a significance level (p) of 0.01. These tests showed that mean salinity, sea surface temperature, pCO_2 and TA were all statistically different between all regions in the 2017 dataset (Table 1.3). These differences are attributed to circulation patterns, variability of contributions from upstream or offshore water masses, terrestrial inputs, or biogeochemical processes; likely the variability is due to a combination of all these factors. The same t-tests indicated that salinity, water temperature, TA and pCO_2 were all significantly different amongst the regions during ECOA-2.

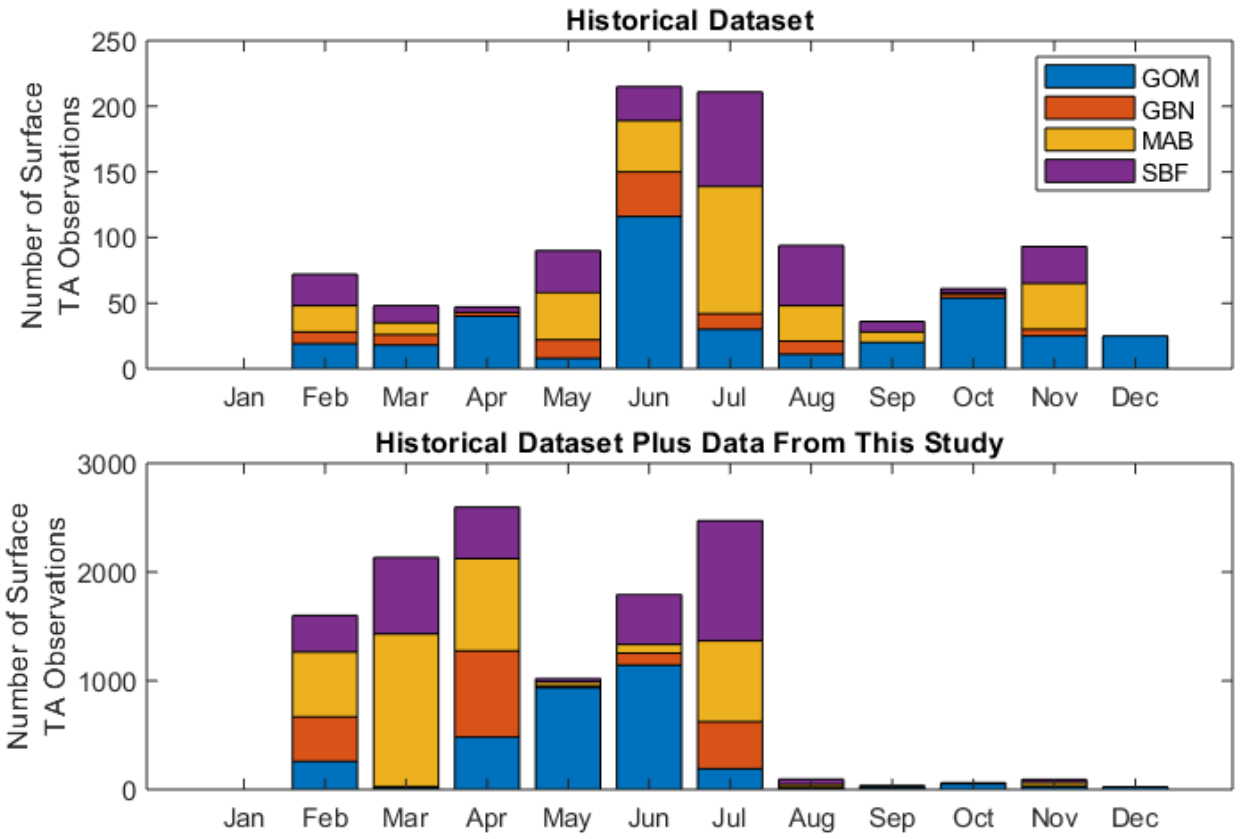

Figure 0.5: Monthly counts of regional surface TA measurements. The top panel shows the counts for each region from the historical dataset described in Section 2.4. The bottom panel shows counts for each region once the HydroFIA TA system measurements from 2017 and 2018 described in this study are included. Note the roughly one order of magnitude difference in y-axis scales between top and bottom panels.

1.3.1 Regional Salinity:TA Regressions

Regressions of regional HydroFIA TA data against salinity showed clear differences between years, regions, and seasons (Figures 1.6-1.9). Broadly, the slope of the TA:S regression line for all 2017 data increased from the GOM (24.9±0.3) to GBN (36.6±0.6) to MAB (36.7±0.3) regions along the path of southward-flowing coastal water, while TA^0 decreased from north to south (1395±8, 1011±19, and 1008±11 µmol

kg^{-1}, respectively). This pattern of increasing slope and decreasing TA^0 from north-to-south is consistent with the results of Cai et al. (2010), but the TA:S regression coefficients were distinctly different from those found by Cai et al. (2010) for all regions, with uniformly shallower slopes and higher TA^0. The 2018 ECOA-2 data showed an opposite pattern to that from 2017, with decreasing TA:S slope from the GOM to GBN to MAB regions (62.7, 52.5, 38.5, respectively) and increasing TA^0 (178, 497, 936 µmol kg^{-1}, respectively). The regressions of surface TA against salinity were again distinctly different from those found by Cai et al. (2010) for all regions, with uniformly shallower slopes and higher TA^0 (Figure 1.10), although the GOM slope (62.7) and intercept (178 µmol kg^{-1}) for 2018 were somewhat similar to the low-salinity GOM slope (65.8) and TA^0 (75.1 µmol kg^{-1}) from Cai et al. (2010). It is important to mention here that the TA-salinity relationships presented in Cai et al. (2010) were constructed from data acquired throughout the water column, from the surface to deeper slope and shelf waters, with the deepest samples ranging from 200-290 m. Thus, direct comparison between the surface measurements presented in this work and the deeper measurements used by Cai et al. (2010) may be unrealistic as contributions from various water masses are likely unequal.

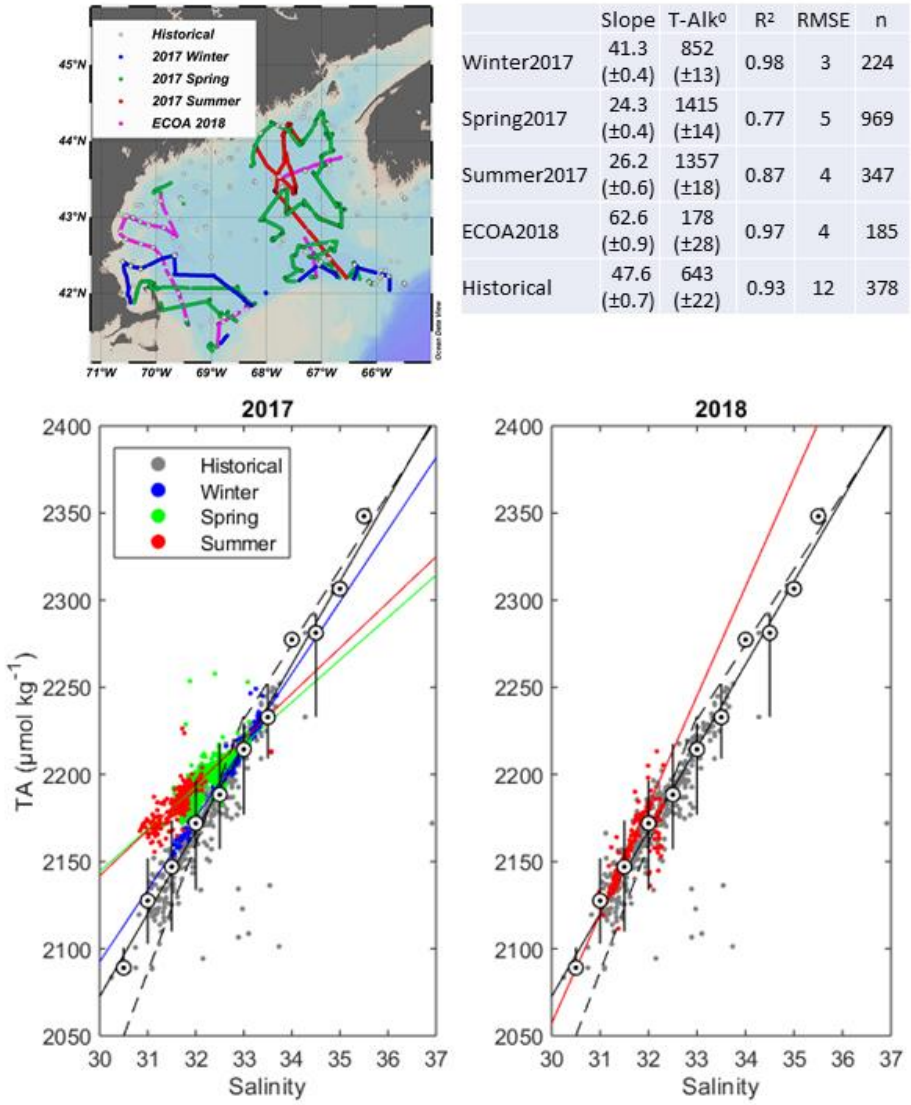

	Slope	T-Alk⁰	R²	RMSE	n
Winter2017	41.3 (±0.4)	852 (±13)	0.98	3	224
Spring2017	24.3 (±0.4)	1415 (±14)	0.77	5	969
Summer2017	26.2 (±0.6)	1357 (±18)	0.87	4	347
ECOA2018	62.6 (±0.9)	178 (±28)	0.97	4	185
Historical	47.6 (±0.7)	643 (±22)	0.93	12	378

Figure 0.6: Gulf of Maine seasonal and historic TA and salinity data. Upper-left panel shows the locations of surface data collections. Lower-left and lower-right panels show scatterplots of seasonal salinity and TA from 2017 and the 2018 ECOA-2 cruise, respectively. Note that the historical data are inclusive of all seasons. For reference, the solid line indicates the robust linear regression of historical data; the dashed lines indicate the mixing lines described by Cai et al. (2010). The slope and TA^0 from Cai et al. (2010) are 65.8 and 75.1±291.2 µmol kg^{-1}, respectively, for sample salinities less than 31.75. The slope and TA^0 from Cai et al. (2010) are 39.1 and 932.7±16.5 µmol kg^{-1}, respectively, for sample salinities greater than 31.75. Whisker plots show the median TA (white circles) at 0.5-salinity intervals of historical data; whiskers indicate the range of TA over each 0.5-salinity interval. Colored lines show the linear regression of measurements for each season. The table in the upper-right lists the linear regression slope and intercept coefficients (with standard errors in parentheses), as well as the r^2, RMSE and *n* statistics. The p-values for all regressions were much less than 0.01.

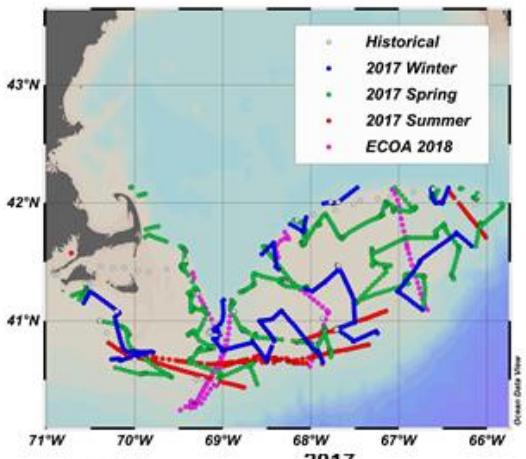

	Slope	T-Alk⁰	R²	σ	n
Winter2017	32.3 (±1.2)	1160 (±41)	0.63	4.4	391
Spring2017	30.2 (±0.8)	1215 (±27)	0.63	6.7	780
Summer2017	18.4 (±1.7)	1600 (±55)	0.40	8.3	181
ECOA2018	52.5 (±0.8)	497 (±25)	0.97	3.4	196
Historical	55.9 (±2.8)	371 (±91)	0.84	12.6	98

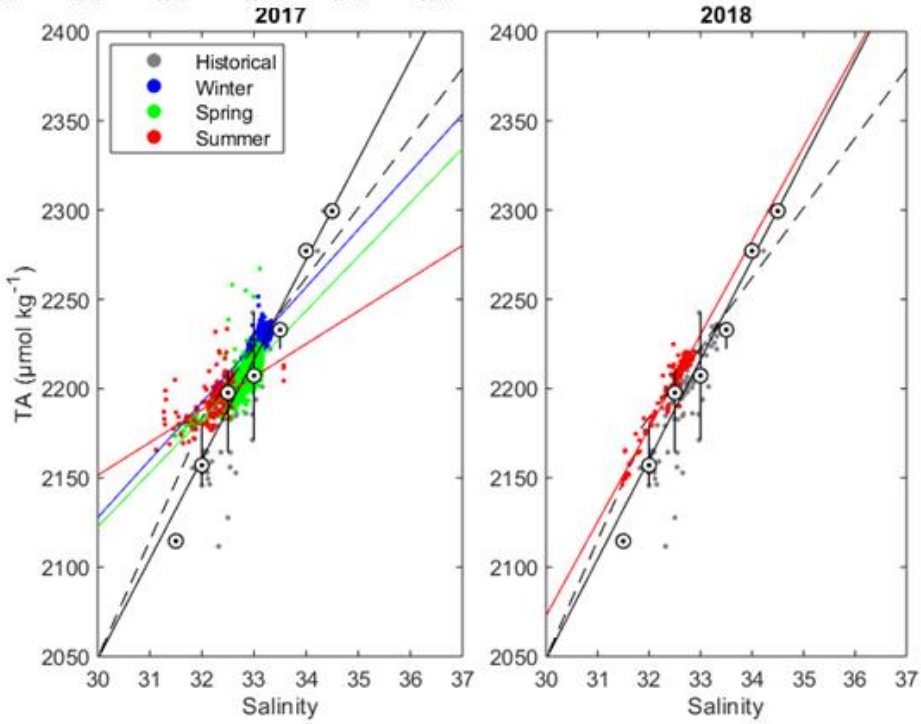

Figure 0.7: George's Bank-Nantucket Shoals (GBN) seasonal and historic TA and salinity data. See the caption of Figure 1.6 for detailed figure explanations. For reference, the solid line indicates the robust linear regression of historical data; the dashed lines indicate the "Woods Hole Transect" mixing lines described by Cai et al. (2010). The slope and TA^0 from Cai et al. (2010) are 73.4 and (-188.7±92.3) µmol kg^{-1}, respectively, for sample salinities less than 33. The slope and TA^0 from Cai et al. (2010) are 43.1 and 809.2±60.9 µmol kg^{-1}, respectively, for sample salinities greater than 33. The p-values for all regressions presented in the table were much less than 0.01.

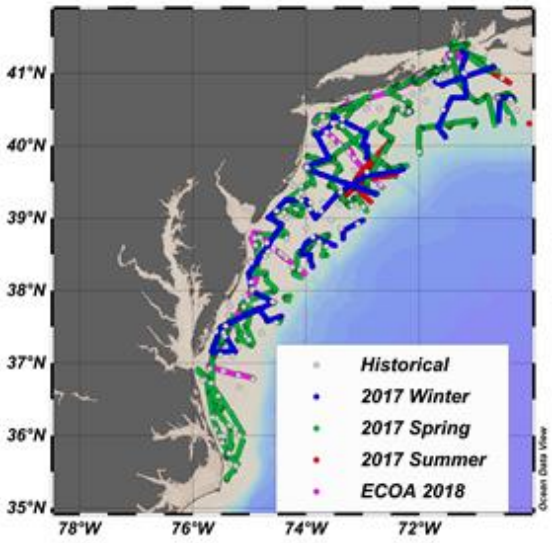

	Slope	T-Alk⁰	R²	σ	n
Winter	40.8 (±0.7)	880 (±25)	0.84	9.2	557
Spring	44.1 (±0.4)	763 (±14)	0.83	11.7	2210
Summer	14.5 (±0.3)	1726 (±8.1)	0.93	1.9	242
ECOA2018	38.5 (±1.2)	935 (39)	0.83	18.2	193
Historical	43.7 (±1.0)	769 (±33)	0.87	18.1	272

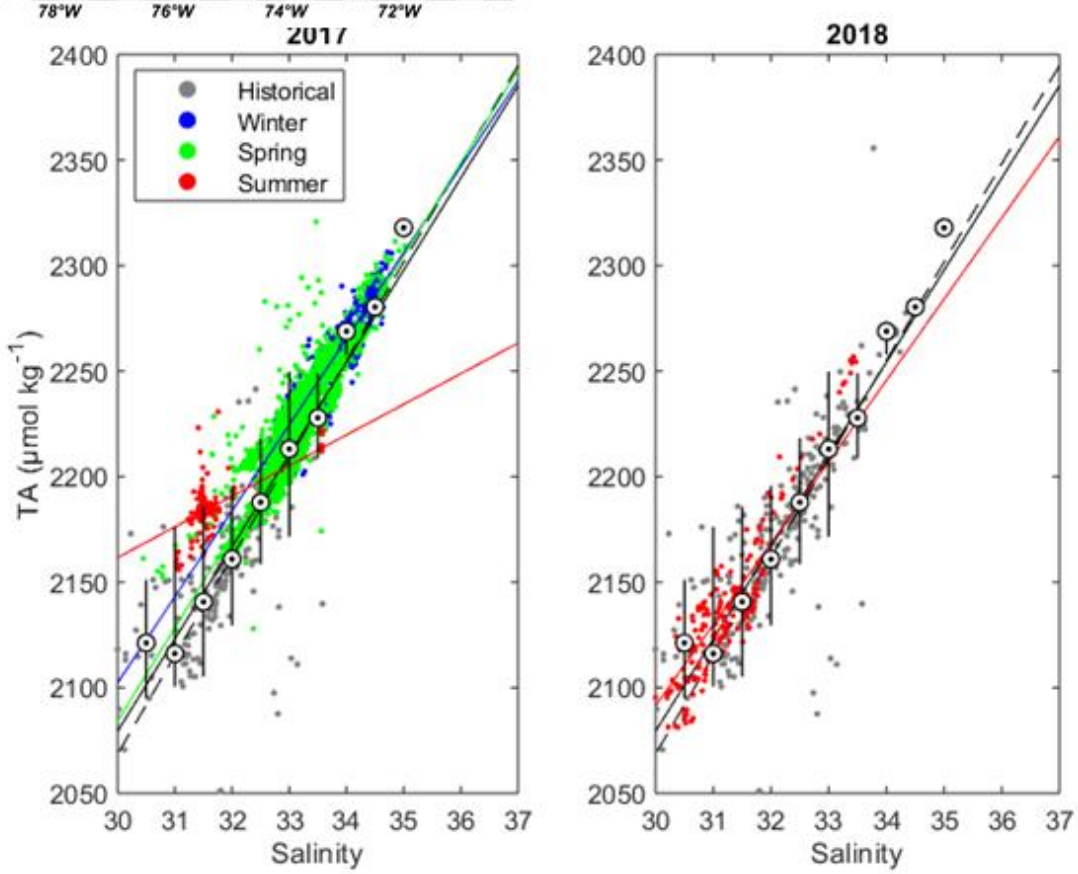

Figure 0.8: Middle Atlantic Bight (MAB) seasonal and historic TA and salinity data. See the caption of Figure 1.6 for detailed figure explanations. For reference, the solid line indicates the robust linear regression of historical data; the dashed line indicates the mixing line described by Cai et al. (2010). The slope and TA^0 from Cai et al. (2010) are 46.6 and 670.6±12.3 µmol kg^{-1}, respectively. The p-values for all regressions presented in the table were much less than 0.01.

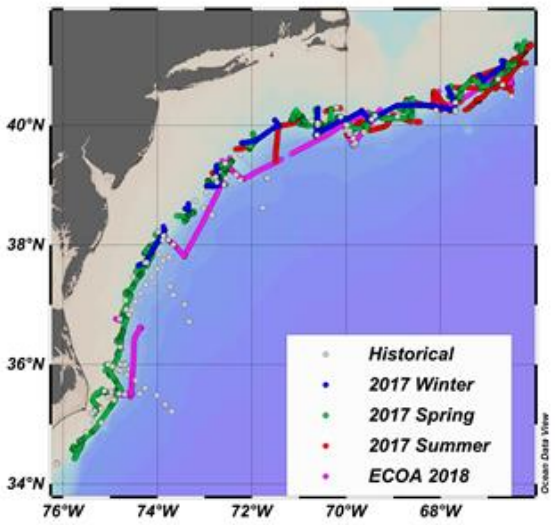

	Slope	T-Alk⁰	R^2	σ	n
Winter	44.2 (±0.3)	761 (±11)	0.98	4.9	303
Spring	42.2 (±0.2)	821 (±8)	0.97	9.7	1139
Summer	21.7 (±0.4)	1497 (±13)	0.82	6.4	704
ECOA2018	46.9 (±0.2)	687 (±8)	0.99	4.8	353
Historical	47.9 (±0.5)	638 (±18)	0.97	10.8	256

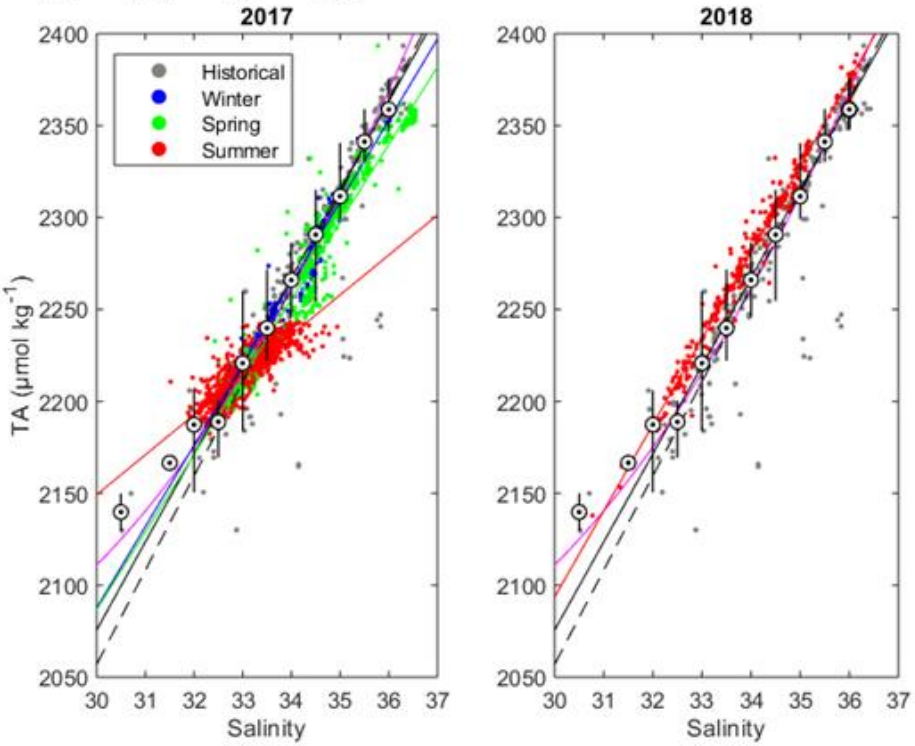

Figure 0.9: Shelf Break Front (SBF) seasonal and historic TA and salinity data. See the caption of Figure 1.6 for detailed figure explanations. For reference, the solid line in the lower two panels indicates the robust linear regression of historical data; the magenta line indicates the mixing line described by Lee et al. (2006, TA = 2305 + 53.97*(S - 35) + 2.74* $(S - 35)^2$ - 1.16 (SST - 20) -0.040 $(SST - 20)^2$, where S is salinity and SST is surface temperature) and the dashed black line indicates the mixing line described by Millero et al. (1998, TA=S*51.24 + 520.1, where S is salinity). The p-values for all regressions presented in the table were much less than 0.01.

Seasonal TA:S shifts were found in the GOM (Figure 1.6). The 2017 winter TA:S slope (41.3) and TA^0 (852 µmol kg^{-1}) were similar to the high-salinity values of Cai et al. (2010, data collected in summer), who reported a slope and TA^0 of 39.1 and 932 µmol kg^{-1}, but during the springtime in 2017 (March through May) the GOM TA:S changed substantially, with a much shallower slope (24.3), higher TA^0 (1415 µmol kg^{-1}), and lower r^2 (0.77). These conditions persisted into the summer of 2017 (June and July) in the GOM, and contrast sharply with the GOM TA:S regression in the summer of 2018. A similar 2017 seasonal shift was seen in the GBN region (Figure 1.7) from winter, through spring and into summer, with progressively shallower slopes (32.3, 30.2, and 18.4, respectively), higher TA^0 (1160, 1215, 1600, respectively), and lower r^2 (0.63, 0.63, 0.40, respectively).

Seasonal regressions from the MAB region in 2017 were lagged in time compared to those from the GOM and GBN regions. MAB winter and spring 2017 TA:S results were quite consistent in 2017 (Figure 1.8), with similar TA:S slopes (40.8 and 44.1, respectively) and TA^0 (880 and 763 µmol kg^{-1}, respectively), and encompassed the MAB slope and TA^0 provided by the historical dataset (43.7 and 769 µmol kg^{-1}, respectively). The summer MAB regression changed substantially in a similar fashion to the GOM and GBN regions, with the TA:S slope dropping from 44.1 to 14.5 and TA^0 increasing from 763 to 1726 µmol kg^{-1}.

SBF TA:S regressions further reinforce the observation that a seasonal shift occurred, as SBF winter and spring slope (44.2 and 42.2, respectively) and TA^0 (761 and 821 µmol kg^{-1}, respectively) were similar in 2017, whereas the summer slope (21.7) and TA^0 (1497 µmol kg^{-1}) were markedly different (Figure 1.9). SBF results are also

notably differentiated by latitude: Steeper SBF winter and spring slopes were influenced by data from latitudes at or below 39°N, whereas the shallower summer SBF slope was mostly controlled by data from latitudes higher than 40°N. Cruise tracks from 2017 (Figure 1.2) showed that the SBF data north of 40°N were collected in a region near the confluence of the SBF, GOM, and MAB regions, whereas the cruise tracks south of 39°N ran very close to the boundaries between the SBF and MAB regions. The SBF slope from 2018 (46.9) was similar to the steeper, lower-latitude 2017 data group and the historical SBF slope (47.9). The 2018 SBF data also followed a uniform linear trend regardless of latitude.

Table 1.4: Deviations between 2017 TA observations and TA estimates from regional models. The models used are those of Cai et al. (2010) and Lee et al. (2006). All differences are calculated as model-derived TA subtracted from the observed TA, thus positive values indicate model underestimate relative to the observed TA. Negative values are shown in parentheses. The third column ("Difference σ") lists one standard deviation of the calculated differences for each region, and the fourth column lists the number of observations. All values are μmol kg^{-1}.

	Difference from Cai et al. (2010)			
Region	Mean Difference	Range of Difference	Difference σ	n
GOM	8	(-33) - 74	14	1546
GBN	-5	(-52) - 90	16	1353
MAB	12	(-60) - 97	16	3009
SBF	-	-	-	-

	Difference from Lee et al. (2006)			
Region	Mean Difference	Range of Difference	Difference σ	n
GOM	13	(-27) - 82	10	1539
GBN	4	(-32) - 67	10	1353
MAB	1	(-66) - 87	12	2764
SBF	-4	(-64) - 53	13	1919

The work of Lee et al. (2006) presented a polynomial expression of both salinity and sea surface temperature for the estimation of TA in North Atlantic surface waters, so direct comparison of linear regression coefficients is not possible here. The GOM equation of Cai et al. (2010) returned TA closer to measured values in 2017 (mean difference 8±14 µmol kg^{-1}, Table 1.4) compared to the Lee et al. (2006) equation including in situ sea surface temperature (mean difference 13±10 µmol kg^{-1}). The reverse was true in the MAB region where the TA calculated according to Lee et al. (2006) was more similar to the observed HydroFIA TA values (mean difference 1±12 µmol kg^{-1}) than TA calculated from the Cai et al. (2010) equation (mean difference 12±16 µmol kg^{-1}). The GBN region was represented equally well in 2017 by the Lee et al. (2006) equation (mean difference 4±10 µmol kg^{-1}) and Cai et al. (2010) equation (mean difference -5±16 µmol kg^{-1}).

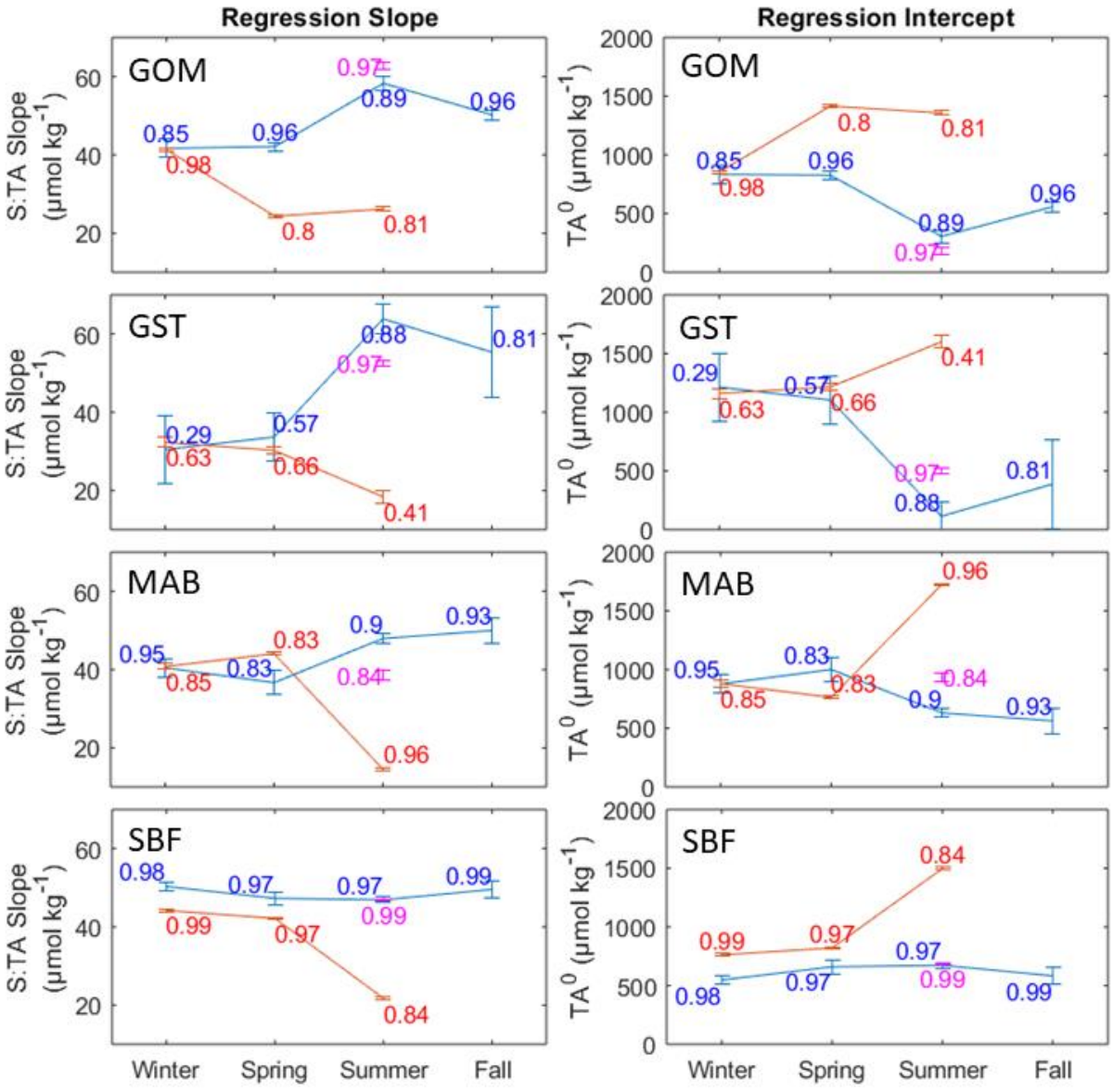

Figure 0.10: Seasonal, regional slope and y-intercept (TA^0) statistics produced from a robust linear regression method (see Section 2.3). Error bars show the standard error around each value, and numbers beside each point correspond to the r^2 statistic. Blue lines and r^2 values were calculated from the historical dataset (see Section 2.4), red lines and r^2 values were calculated from the 2017 HydroFIA TA data, and magenta lines and r^2 were calculated from the 2018 ECOA HydroFIA TA data.

Regional and seasonal changes in TA:S combine to form a cohesive trend in 2017. During winter, the TA:S slope and TA^0 for all regions except the SBF were indistinguishable both from those of Cai et al. (2010, Figures 1.6-1.9) and from historical TA:S trends (Figure 1.10). The winter SBF slope (44.2), while not indistinguishable, still resembled the slope from the historical dataset (47.9) as well as the "Atlantic" slope of 51.2 presented by Millero et al. (1998, Figure 9). Thus, the winter of 2017 data appear to reflect 'typical' conditions consistent with previous findings. In contrast, atypical conditions developed in the GOM in the spring of 2017 and continued into the summer and expanded southward and westward to the GBN, MAB, and SBF regions. By the summer of 2017, all regions showed TA:S conditions quite different from both the historical dataset and the results of Cai et al. (2010). These atypical summer conditions were not reflected in the 2018 ECOA-2 data, so the progression seen in 2017 is likely not due to typical seasonal patterns. Instead, the historical data show that the shifts in 2017 were opposite of the typical seasonal changes in TA:S slope and TA^0.

1.3.2 Seasonal Biases in Data Availability

It is important to note here the paucity of available historical TA observations in winter; despite collecting the broadest extent of data we could find, there were no surface TA measurements in any region in January, and only about 25 GOM measurements in December (Figure 1.5). The vast majority of historical winter measurements were taken in February, and the existing East Coast TA data are overall heavily weighted towards summertime sampling. Data collected aboard the *Bigelow* in

2017 by the HydroFIA TA instrument provided some of the first widely spatially-distributed TA measurements along the East Coast outside the summer months, as the GOMECC and ECOA cruises were all conducted during the summer months of June, July and August. Regular NOAA Ecosystem Monitoring (EcoMon) cruises have been conducted since 2012 during non-summer months, including TA sampling, but with a limited number of stations. Incorporation of the data collected in this work increases available TA observations by more than one order of magnitude during the months when the HydroFIA TA system was deployed. Winter is a difficult time to conduct cruises in Atlantic waters, but it is also a biologically important season, as it sets up conditions for the springtime bloom. The lack of historical evidence of shifts in seasonal TA:S, such as we have shown, may not be because these shifts are rare, but because the data have not been available to detect them.

1.3.3 Mechanisms Affecting Linear TA:S Relationships

A variety of processes can alter ocean TA and salinity, contribute to TA:S variability, and potentially contribute to the observations presented here. Over time scales greater than 100,000 years, alkalinity (and salinity) in the oceans are controlled by geologic weathering and net seafloor sedimentary processes whereas over time scales between 1,000 and 100,000 years surface alkalinity is controlled by variations in biological pumping and interactions with carbonate and silici-clastic sediments (Zeebe 2012). On shorter time scales, Takahashi et al. (2014) described five “oceanographic situations” and their effect upon the linear TA:S relationship. These situations, which will be discussed in terms of their applicability to the findings from this study, are: (a)

evaporation-precipitation (b) mixing in subtropical gyres between subtropical waters (whose TA is depleted by calcareous organism growth) and fresher subpolar waters enhanced in TA due to upwelling (c) biological production and decomposition, especially of $CaCO_3$-containing shells (d) mixing of a source water with river water containing higher or lower TA, and (e) mixing of a source water with another body of water containing higher salinity and reduced TA (such as a warm evaporative basin or upwelled slope waters). As evaporation-precipitation (a) alters salinity and TA in proportion, this process will not affect the TA:S relationship. Neighboring regions exhibiting higher salinity and TA include the coastal SAB region to the south and the more offshore Gulf Stream water mass, providing two possible sources contributing to process (e). The regions in this study are likely not large enough to reflect changes in subtropical-subpolar mixing over seasonal time scales (e.g., Fry et al. 2015), and thus process (b) can be discounted. This leaves the situations of biological production (c), river water mixing (d), or mixing with a higher salinity water mass (e) as the most likely processes affecting the TA:S relationships in these regions.

1.3.4 The Effect of Net Calcification or Dissolution

$CaCO_3$ production events have been shown to lower TA (Bates et al. 1996a, Bates 2001), and therefore alter the slope of the TA:S line. In a regional context, uniform production across the region would result in no change to the TA:S line, whereas higher production in the saltier waters of a region would lead to a decreased TA:S slope, and higher production in the lower salinity waters would lead to an increased slope. This biological utilization in high-nutrient waters can potentially account

for up to a 50 µmol kg^{-1} TA reduction (Takahashi et al. 2014, Bates et al. 1996b, Harlay et al. 2010). It is conceivable that an offshore bloom of a calcifying species (such as a coccolithophore) could have drawn down TA in 2017, reducing the slope of the TA:S mixing line. This could explain the high-salinity data in 2017 that fall well below the Millero et al. (1998) regression line (Figure 1.9), but corresponding $CaCO_3$ dissolution is needed to explain the low-salinity data that fall above the Millero et al. (1998) line. This can be seen especially in the offshore SBF region, where the 2017 summertime TA:S line appears to be rotated about a salinity of 33 relative to the other SBF regression lines, with lower TA above salinity 33 and higher TA below (Figure 1.9). An offshore calcifying bloom could explain the apparent TA drawdown above salinity 33, with corresponding $CaCO_3$ dissolution inshore explaining the elevated TA input below salinity 33. Indeed, reductions in the TA:S slopes in the GOM, GBN and MAB regions all appear to be due to lower-salinity TA enhancement (Figures 1.6-1.8).

The formation of $CaCO_3$ by calcifying species results in elevated pCO_2 through shifts in the DIC:TA ratio, with the opposite effect for $CaCO_3$ dissolution (Zeebe 2012, Bates et al. 1996b); however, the overall net pCO_2 change depends on the amount of $CaCO_3$ formation or dissolution relative to net ecosystem production. Thus, elevated pCO_2 levels would be expected in areas where calcification is the primary mechanism of TA:S variability, and reduced pCO_2 in those areas where dissolution predominates, although other mechanisms may offset some or all of this pCO_2 increase (Balch 2018). In the case of the GOM region, the mean 2017 summer pCO_2 (335 µatm) was lower than any other sampling period within the GOM region for this study, a potential indication of $CaCO_3$ dissolution, or alternatively high net productivity. For a historical

climatological comparison all surface pCO_2 measurements within each study region were extracted for each season from the 2019 Surface Ocean CO_2 Atlas with data from 1957 to 2019 (SOCAT2019, Bakker et al. 2016). The mean GOM pCO_2 in summer 2017 (336 µatm) was significantly lower than the historical (2002-2018) mean GOM summer pCO_2 from the SOCAT database (370 µatm) as well as the mean GOM pCO_2 from the 2018 ECOA-2 cruise (390 µatm, significance determined according to one-way ANOVA tests, see Supplementary Material Figure A.3). Some of this difference may be due to the colder temperature in 2017 resulting in lower pCO_2. Furthermore, the 2017 summer MAB and SBF mean pCO_2 values (376 and 366 µatm, respectively) were significantly lower than the respective values from summer 2018 during the ECOA-2 cruise (421 and 398 µatm, respectively) or seasonal mean pCO_2 from the SOCAT database (411 and 392 µatm, respectively). While the presence of lower pCO_2 concurrent in space and time with the atypical TA:S relationships supports the idea that $CaCO_3$ dissolution resulted in elevated TA:S slopes in the coastal GOM and MAB regions, this mechanism is unlikely given that these surface waters are typically supersaturated with $CaCO_3$ (Wanninkhof et al. 2015).

1.3.5 Potential River or Shelf Mixing Effects

Mechanisms (d), mixing of a source water with river water containing higher or lower TA and (e), mixing with a higher salinity water mass, remain as explanations to the observed seasonal TA:S shifts. Cai et al. (2010) characterized the GOM, GBN and MAB regions as “Current-Dominated Margins”, where freshwater and TA inputs from local rivers are greatly outweighed by those carried by alongshore currents. For regions

in this study, the dominant alongshore current is the southward-flowing Labrador Current, a branch of which travels successively southward through the GOM, GBN, and MAB regions. Recent rapid warming of the Gulf of Maine (Pershing et al. 2015, Pershing et al. 2018) has been linked to increased intrusions of deeper, salty, and warm water through the Northeast Channel and concurrent reductions in Labrador water (Figure 1.1, Townsend et al. 2015, Brickman et al. 2018), the prevalence of which are in turn affected by changes in the Atlantic Meridional Overturning Circulation (Sherwood et al. 2011, Claret et al. 2018) or changes in the strength of the Labrador Current inflows (Jutras et al. 2020). Cai et al. (2010) suggest that continuous mixing of regional surface water with deeper slope and shelf waters would result in the lowering of the TA:S slope, providing a possible explanation of the seasonal shifts seen in this study. This explanation may not be satisfactory, as the regional salinities in 2017 generally decreased from winter to spring and then summer, while the TA at lower salinity gradually rises above the mixing line, suggesting a change in the amount of freshwater and TA being carried into the region.

The seasonal TA:S shifts seen in the 2017 data may have resulted from an increase of upstream shelf water entering the GOM relative to warm slope water. GOM temperature anomaly analyses, updated through 2020 using methods described by Pershing et al. (2015), show that GOM surface temperatures in early 2017 (January and February) were high enough to be judged a ‘heat wave’ (Pershing et al. 2018, updated data presented at https://www.gmri.org/stories/gulf-maine-temperature-update-normal-new-cold/, accessed 10/4/2020). The GOM surface water temperature then fell through the spring and early summer to either lower-than-usual or typical values, indicating a

transition from warmer, saltier source water to colder, fresher shelf water. Cai et al. (2010) report a Labrador TA:S regression slope of 33 and TA^0 of 1124 µmol kg^{-1}. These values are lower than the 2017 summer GOM slope and TA^0 in this study (26.2 and 1357 µmol kg^{-1}, respectively, Figure 1.10). As the Labrador Current travels from the Labrador Sea to our study regions and becomes shelf water, it is modified by other inputs, notably those from the St. Lawrence Estuary, which carries massive amounts of freshwater to the Atlantic coast north of Nova Scotia. St. Lawrence Estuary TA^0 (1124-1314 µmol kg^{-1}, Dinauer and Mucci 2017, 2018) is typically lower than the TA^0 calculated for spring 2017 in the GOM (1415 µmol kg^{-1}) and summer 2017 in all study regions- all TA^0 values which statistically exceed the historical TA^0 for each region by wide margins. Whereas the St. Lawrence experienced a large flooding event in early 2017 (ILO-SLRB 2018), the water transit time of more than six months between the St. Lawrence and the Gulf of Maine discounts the influence of the St. Lawrence on our 2017 observations (Ohashi and Sheng 2013). Measured TA^0 values from local rivers in the GOM, GBN, and MAB regions (Hunt et al. 2011, Cai et al. 2010) are much too low to account for the elevated TA^0 measured in this study, and discharge levels from these rivers are too small to broadly impact the biogeochemistry of these regions (Cai et al. 2010).

We compared surface salinity measured in this study to climatological data from the World Ocean Atlas 2018 (WOA2018) salinity product (Zweng et al. 2019). Gridded monthly North Atlantic and Coastal WOA2018 salinity at 1/4° resolution was retrieved, and the same regional boundaries discussed previously were used to compute seasonal, climatological statistics for the GOM, GBN, MAB and SBF regions. In three of

the four study regions (GOM, GBN, and SBF), the 2017 mean summer salinity was lower than that from winter or spring 2017, and lower than the seasonal mean WOA salinity for winter, spring or summer (see Supplementary Material Figure A.3). The GBN and SBF 2017 mean summer salinities were also lower than those from ECOA-2. The one exception is the MAB region, where the mean 2017 summer salinity was indistinguishable from the mean summer salinity during ECOA-2 or from the WOA, and all were lower than the 2017 mean winter and spring salinities. These exceptionally low salinities show the abnormal levels of freshwater present in the regions, which cannot be accounted for by local river discharge, and instead must be transported southward by upstream sources.

Mixing with freshwater can potentially explain the 2017 changes in TA:S slope but cannot readily explain the relatively low TA at salinities greater than 35, which were observed around Cape Hatteras. Lower than usual pCO_2 suggests that biological uptake through calcification was not likely, and thus another high-salinity endmember, with characteristic TA much lower than the Gulf Stream is needed. One possibility is provided by Cai et al. (2010), who describe TA:S regressions from seven South Atlantic Bight (SAB) shelf cruises resulting in a calculated TA at salinity 36.5 of 2366-2400 µmol kg^{-1}, with a mean value of 2384 µmol kg^{-1}. The same paper lists an unusual TA:S slope and TA^0 from a series of GYRE93 cruises around the intersection of the MAB and SAB regions which result in an unusually low calculated TA at salinity 36.5 of 2300 µmol kg^{-1}, and support the concept that the observed 2017 TA from this study at salinity 36.5 (2355 µmol kg^{-1}) is low but not unprecedented. The SAB thus represents a potential high-salinity/low TA water source, through surface water exchange between coastal

SAB waters inshore of the Gulf Stream and the MAB and SBF regions, or SBF water transported northwards via the Gulf Stream and then eastwards into the MAB region via eddies or warm-core rings (Rasmussen et al. 2005, Hare and Cowen 1996).

Previous work has discussed a mean southward flow of coastal water from the GOM, through the GBN, and into the MAB region (Townsend et al. 2006, Cai et al. 2010, Wang et al. 2013, Wanninkhof et al. 2015), with both salinity and TA enriched by mixing with slope waters along the way. The measurements made as part of this study, as well as the historical data discussed above, indicate that the surface water conditions are substantially more complex between regions and across seasons. In addition to the alongshore gradient in TA, there also appears to be an offshore influence as well, as warmer and saltier north-flowing Gulf Stream water interacts with southward-flowing coastal water masses. The mixing balance between the saltier, TA-enriched northward-flowing Gulf Stream water, the southward-flowing shelf water, and deeper slope water may dictate much of the distribution of salinity and TA along the East Coast.

1.4 Conclusions

Deployment of the CONTROS HydroFIA® TA instrument aboard the *Bigelow* produced high quality (u_c of 2.4-4.1 µmol kg^{-1}) surface TA data over broad spatial and temporal time scales. Results from 2017 and 2018 showed that use of the HydroFIA TA instrument aboard cruises of opportunity can greatly increase regional carbonate system monitoring capacity. Inter-annual and seasonal comparisons showed that TA distributions along the United States East Coast are dynamic, not easily predicted from

physical variables such as salinity, and not yet fully characterized by current studies. Significant seasonal shifts in linear TA:S relationships demonstrate potential problems with any single linear model for the retrieval of TA from salinity. Analysis of a compiled historical regional dataset reinforces the finding that salinity, TA, and TA:S linear relationships shift seasonally, although data availability is extremely sparse in some months and regions. Additional deployments during undersampled months may further advance the understanding of the seasonal nature of TA:S relationship in these regions, and analyses of derived DIC, pH or carbonate saturation state may provide even more insights. Especially when deployed on ships equipped with instrumentation to measure another carbonate system parameter (i.e., pCO_2), the HydroFIA TA instrument represents a substantial advancement in the ability to comprehensively monitor and characterize surface waters.

CHAPTER 2: CONTROLS ON BUFFERING AND COASTAL ACIDIFICATION IN A NEW ENGLAND ESTUARY

2.1 Introduction

Balanced at the confluence of the land and sea, estuaries are dynamic mixing zones, sites of biogeochemical transformations and enrichments, and essential habitats in the life cycles of many species. The continuous, complex journey of dissolved and particulate materials derived from terrestrial sources through an estuary proceeds along a number of dimensions in space and time (Borges 2005, Gattuso 1998). Along one dimension, substances are carried by rivers and groundwater into the estuary, where they are physically mixed with coastal seawater while utilized and altered by pelagic and benthic organisms. Vertical exchanges between the pelagic water column, benthic sediments and the atmosphere add a vertical dimension of complexity (Cai et al. 2017), while mixing of water and associated materials within certain ecosystems such as mangroves and salt marshes provide another lateral dimension (Sippo et al. 2016, Wang and Cai 2004, Wang et al. 2016). Finally, all of the above mechanisms may be altered over time by shifts in temperature and salinity, changes in freshwater discharge and associated changes in constituent loads, seasonal and episodic alterations in net ecosystem productivity, anthropogenic watershed and ecosystem modifications, variations in coastal ocean exchange, and other short- and long-term factors (Lee et al. 2015, Pacella et al. 2018, Waldbusser and Salisbury 2014).

Against this backdrop of complex biogeochemical changes, estuaries are also situated as hotspots of acidification (Cai et al. 2020). The accumulation of

anthropogenic carbon dioxide (CO_2) in the atmosphere has led to a compensatory increased uptake of CO_2 by the global ocean in a process termed ocean acidification (OA, Orr et al. 2005, Doney et al. 2009), which has driven down seawater pH by about 0.1 units since the start of the Industrial Revolution and threatens to further lower pH by another 0.3 by the end of the 21st century (Caldeira and Wickett 2003). In addition to OA, estuaries are also under acidification pressure from coastal-specific processes grouped into the term coastal acidification (CA). CA specifically refers to nutrient-enhanced productivity which can lead to enhanced productivity and subsequent decomposition of the produced organic material (Breitburg et al. 2015) and also refers to shifts in the amount and composition of freshwater discharge (Kaushal et al. 2013, Kaushal et al. 2014, Salisbury et al. 2008). The combined effects of OA and CA are termed ocean and coastal acidification (OCA), which result in changes in pH and other properties due to both local and remote forcing (Gledhill et al. 2015). The capacity of a water body to resist changes in acid level is termed buffering and can be parameterized using the concentrations of total alkalinity (TA) and dissolved inorganic carbon (DIC) in that water body (Egleston et al. 2010). Changes to both the absolute concentrations and the relative proportions of TA and DIC can have potentially profound effects on the buffering capacity (and consequently pH) of an estuary; thus the influences of mixing and biogeochemical transformations of TA and DIC in an estuary are important to understand in light of growing OCA pressures.

Estuaries are generally thought to enrich DIC through the respiration of allochthonous and autochthonous organic carbon and transport of river and coastal wetland DIC (Bauer et al. 2013, Borges et al. 2003, Sippo et al. 2016). Conversely,

primary productivity and carbonate precipitation can draw down DIC. Additionally, several processes have been shown to produce TA within estuaries (Table 2.1), including primary productivity, denitrification, manganese reduction, iron reduction, and sulfate reduction (Raymond et al. 2000, Borges et al. 2003, Sippo et al. 2016). Growth of calcifying organisms, such as oysters, and the harvest or burial of their shells represents a sink of TA (Waldbusser et al. 2013), as does aerobic respiration (Borges et al. 2003). In the Chesapeake Bay, Waldbusser et al. (2013) estimated a TA sink of 225 g m^2 yr^{-1} (assuming the loss was entirely due to calcium carbonate formation). In the temperate York River estuary, Raymond et al. (2000) attributed additions of TA and DIC to sulfate reduction. In mangroves TA export estimates range from –1.2 to 117 mmol m^2 d^{-1} (Leopold et al. 2016, Sippo et al. 2016), while mangroves may account for up to 93% of DIC exports in a watershed (Faber et al. 2014). Several studies have identified sulfate reduction and aerobic respiration as the major drivers of TA and DIC additions in mangroves (Borges et al. 2003, Bouillon et al. 2007, Sippo et al. 2016). Salt marshes have also been described as 'CO_2 Pumps'- absorbing CO_2 from the atmosphere and exporting the resulting inorganic carbon (at least partly as TA) to the coastal zone (Wang and Cai 2004). Several salt marsh systems have been shown to follow this mechanism; however, these studies have been limited to sites containing a large proportion of marsh habitat (Cai and Wang 1998, Wang and Cai 2004), or were based on discrete sampling at monthly or seasonal time scales, which may not capture shorter-scale variability. Estuaries are also frequently mixed-habitat areas, with a wide array of processes and natural and anthropogenic factors combining to affect the TA and DIC exchange with the coastal ocean. Additionally, the dynamics of TA and DIC

production, consumption and exchange may change episodically, seasonally, or on an interannual basis.

Estuaries and coastal waters in New England have been identified as particularly vulnerable to the effects of OCA (Gledhill et al. 2015, Salisbury et al. 2008), and local management agencies have initiated studies of the potential effects of OCA (COMNARE 2017, MSLCOOA 2021) and called for the examination of the contributions of individual processes to overall OCA. Here, we present a study of a New England estuary using novel, highly-resolved time series measurements of TA and derived DIC, and use the ratios of these parameters to examine the seasonality and relative magnitudes of processes that affect buffering, pH, and potential future OCA.

Table 2.1. Aerobic and anaerobic biogeochemical processes and their relative stoichiometric alterations to TA and DIC. Positive values for ΔTA and ΔDIC indicate additions of total alkalinity and dissolved inorganic carbon by the forward reaction, respectively; negative values indicate removal. Values for carbonate transformation are for dissolution/precipitation, respectively. Table compiled after Sippo et al. (2016) and Cai et al. (2017).

Process(es)	Formula	ΔTA	ΔDIC	nTA:nDIC
Primary Production	$106CO_2 + 16HNO_3^- + H_3PO_4 + 122H_2O \leftrightarrow (CH_2O)_{106}(NH_3)_{16}(H_3PO_4) + 106O_2$	+17	-106	-0.16
Aerobic Respiration	$(CH_2O)_{106}(NH_3)_{16}(H_3PO_4) + 106O_2 \leftrightarrow 106CO_2 + 16HNO_3^- + H_3PO_4 + 122H_2O$	-17	+106	-0.16
Sulfate Reduction	$CH_2O + 0.5SO_4^{2-} + 0.5H^+ \rightarrow CO_2 + 0.5HS^- + H_2O$	+1	+1	+1
Carbonate Dissolution/ Precipitation	$CaCO_3 \leftrightarrow Ca^{2+} + CO_3^{2-}$	+2/-2	+1/-1	+2
Denitrification	$CH_2O + 0.8NO_3^- + 0.8H^+ \rightarrow CO_2 + 0.4\ N_2 + 1.4H_2O$	+0.8	+1	+0.8
Nitrification	$0.5NH_4^+ + O_2 \rightarrow 0.5NO_3^- + 0.5H_2O + H^+$	-1	0	n/a
Iron Reduction	$CH_2O + 4Fe(OH)_3 + 8H^+ \rightarrow CO_2 + 4Fe^{2+} + 11H_2O$	+8	+1	+8

2.2 Study Area and Methods

The Great Bay is a macrotidal estuary covering 44 km^2 in southeastern New Hampshire and southwestern Maine, USA. The Great Bay is enclosed by 230 km of generally steep rocky shoreline, bordered by narrow salt marshes, and connected to the neighboring Gulf of Maine via the Piscataqua River (Figure 2.1). Great Bay contains about 9 km^2 of salt marsh, or about 20% of the total estuary area, with the remaining area comprised of clam flats, eelgrass beds, intertidal and subtidal macroalgal cover, mudflats, and rocky outcrops and islands (Jones 2000).

The University of New Hampshire's Coastal Marine Laboratory (CML) is located at the outlet of Great Bay at the mouth of the Piscataqua River. A continuously pumped intake located 0.5 m from the bottom of the Piscataqua channel supplies the CML with seawater. Water depth at this intake ranges roughly between 4 and 6 meters over a typical tidal cycle (DeMeo 2011). Tidal exchange and currents at this location are very strong, and previous work at this same location showed that low tide water pumped to CML was comprised of outgoing Great Bay estuary water, while at high tide the water was near-shore western Gulf of Maine water (Brown 2006).

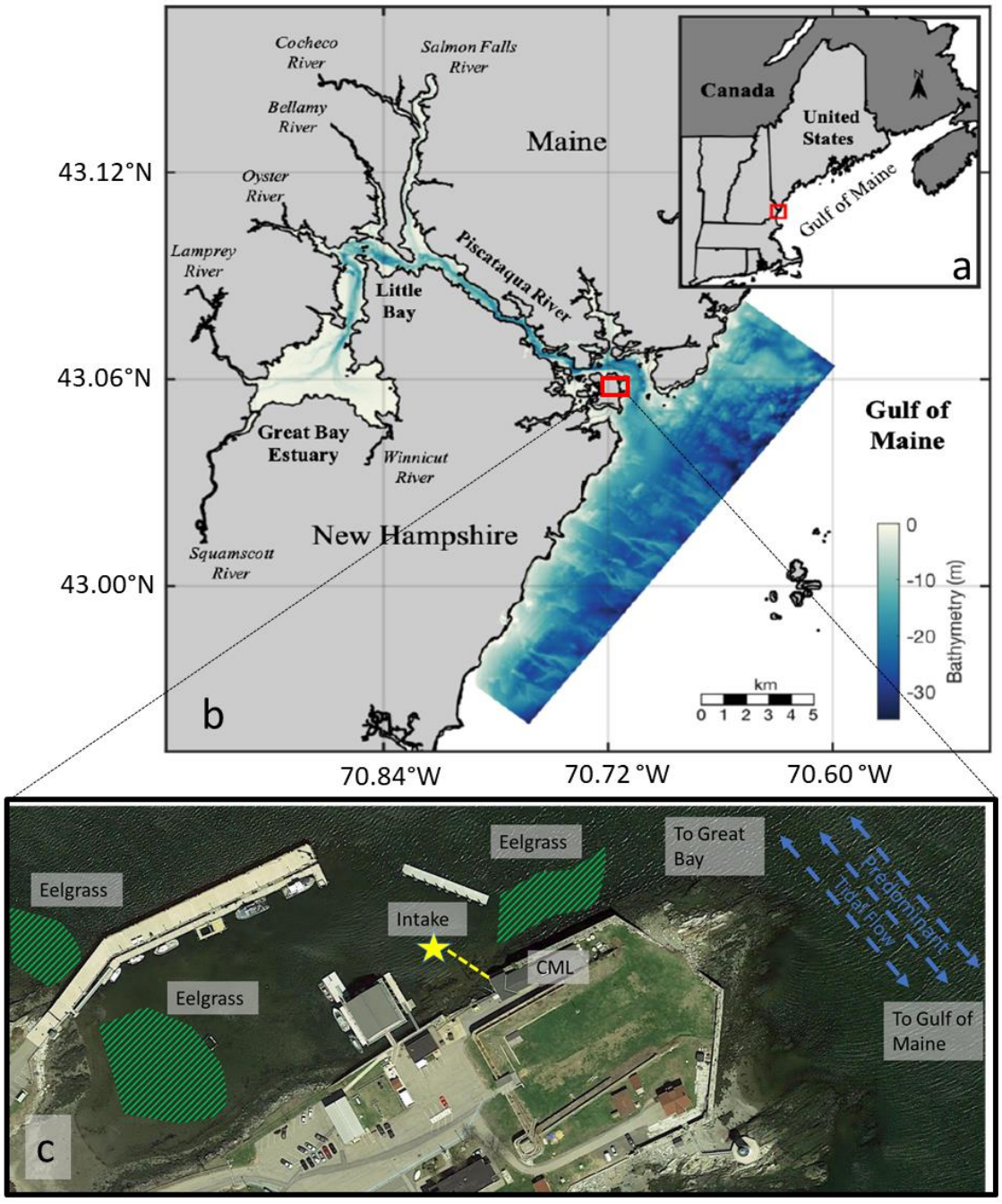

Figure 2.1: The Great Bay estuary. Panel (a) shows the Gulf of Maine region, with Great Bay indicated by a red box. Panel (b) includes Great Bay, its bathymetry, and its contributing rivers, with the Coastal Marine Laboratory (CML) location shown as a red box. Panel (c) shows aerial imagery of the CML and surrounding environs, including the lab water intake (yellow), local eelgrass beds (green), and predominant tidal flow (blue). Panels (a) and (b) used with permission from Cook (2019), panel (c) modified from Google Maps imagery.

Sensors for the measurement of CML intake water temperature and salinity (Aanderaa 4319) and dissolved oxygen (Aanderaa 4835) were suspended in a large 200-liter open tank equipped with a passive debubbling and sediment settling system. Seawater was continuously pumped through this tank at a rate of about 5 liters per minute. Seawater was also pumped to a spray-type seawater gas equilibrator for the measurement of pCO_2, similar to that described by Wanninkhof and Thoning (1993). Equilibrated air was drawn at 100 mL/min through tubing containing a Nafion selectively permeable membrane (Perma Pure, Toms River NJ), with the same analyzed sample stream at lower pressure returned through an outer tubing to carry away the stripped water vapor. This “reflux method” effectively dries the sample gas stream of water vapor with no external supply of drying gas required. No water temperature difference was observed between that measured by the Aanderaa temperature sensor in the open tank and the outflow from the equilibrator (measured with a handheld meter—YSI Yellow Springs, Ohio—manufacturer accuracy ±0.2 °C). Temperature data from the Aanderaa sensor was used in sea-surface temperature corrections during the calculation of pCO_2. After drying, the sample was pumped to a non-dispersive infrared gas analyzer (Li-cor LI-840, Lincoln NE), which measured the molar fraction of carbon dioxide (xCO_2) of the sample stream. The Li-cor was calibrated weekly or biweekly using a tank of pure nitrogen (0 ppm CO_2 molar fraction) and a tank of known CO_2 concentration (span tank). Over the study period we employed a succession of span tanks containing a gas mixture with CO_2 molar fraction between 500 and 850 ppm (Scott-Marin, Riverside, CA), which were calibrated against a primary standard obtained from the National Oceanic and Atmospheric Administration’s Earth System Research

Laboratory. Additionally, a set of switching valves operated by a computer running a custom-built software program allowed for periodic checks of pure nitrogen and span gas to monitor instrument drift. Corrections of data for water vapor pressure and sea surface temperature and conversion from xCO_2 to the partial pressure of carbon dioxide (pCO_2) were carried out according to standard methods (Dickson et al. 2007). The estimated uncertainty of pCO_2 measurements is ±3 µatm.

An automated total alkalinity analyzer (Contros HydroFIA TA) was installed at CML in May 2016 and operated until November 2019, with an extended break in later 2017 when the instrument was returned for service, and a longer break from 2018 into 2019 when fire damaged the CML facility and regular operations were suspended. The HydroFIA instrument performs a single-point titration of seawater with 0.1N hydrochloric acid, using bromocresol green as the indicator for spectrophotometric pH detection, a technique developed by Yao and Byrne (1998) and refined by Li et al. (2013). Filtered seawater (pore size 0.2 µm) was supplied to the HydroFIA instrument from a cross-flow filter supplied by Kongsberg. The HydroFIA instrument was set to perform hourly measurements, and re-calibrated on a one to two week interval with certified reference material from Dr. Andrew Dickson (Dickson et al. 2003). All CML data, including measurements of TA and pCO_2, are hosted by the Northeastern Regional Coastal Ocean Observing System (http://neracoos.org).

2.2.1 Derived parameter calculation

The concurrent measurements of salinity, temperature, pCO_2 and TA at CML allowed for the determination of other carbonate system components. The calculation of dissolved inorganic carbon (DIC) and pH (on the total scale, at a constant 25°C or at *in-situ* temperature) was performed using the CO2SYS program (van Heuven et al. 2011). The K1 and K2 constants chosen were the estuarine constants of Cai and Wang (1998), the KSO_4 and KB constants were those of Dickson et al. 1990 and Dickson 1990 respectively, and the total boron concentration was calculated from salinity according to Uppstrom (1974). Phosphate and silica concentrations were set to zero in CO2SYS, as studies have shown low nutrient concentrations in the study area (Short 1992, PREP 2018). The buffer factor β-H was also calculated by first calculating β-TA (Equation 1) and then applying a proportionality constant to calculate β-H (Equation 2). ß-H and β-TA are buffering factors which quantify the capacity of seawater to resist a chemical change such as the addition of acid. These buffer factors are related to, but not identical to, the Revelle factor which quantifies the change in pCO_2 relative to a change in DIC (Broeker et al. 1979). We used the bicarbonate ($[HCO_3^-]$), carbonate ($[CO_3^{2-}]$), hydrogen ion ($[H^+]$), and borate ($[B(OH)_4^-]$) concentrations and K_B returned by CO2SYS for each pair of observed pCO_2 and TA to calculate the β-TA and β-H according to Egleston et al. (2010):

$$\beta - TA = \left(\frac{\partial \ln[H^+]}{\partial TA}\right)^{-1} = \frac{TA_C^2}{DIC} - F_S \qquad (2.1)$$

where $TA_C = [HCO_3^-] + 2[CO_3^{2-}]$, $DIC = [CO_2] + [HCO_3^-] + [CO_3^{2-}]$, and F_S is a sensitivity factor (denoted simply "*S*" in Egleston et al. 2010, but modified here to avoid confusion with the common salinity notation): $F_S = [HCO_3^-] + 4[CO_3^{2-}] + \frac{[H^+][B(OH)_4^-]}{K_{HB}+[H^+]} + [H^+] - [OH^-]$

β-H, the resistance of pH to change upon addition of a strong acid or base (TOTH), was then calculated according to Egleston et al. (2010):

$$\beta - H = -\left(\frac{\partial pH}{\partial TOTH}\right)^{-1} = -2.3\ x\ \beta - TA \qquad (2.2)$$

The presence of organic constituents contributing to measured titration alkalinity has been shown in estuaries (Cai et al. 1998), coastal waters (Yang et al. 2015), and even reference materials (Sharp and Byrne 2021). While the concentrations of organic alkalinity constituents were shown to be generally low relative to TA, the concentrations were variable and the sources of the organic constituents were unclear. In light of these uncertainties, calculations in this study were performed under the approximation that TA did not contain an organic component.

2.2.2 Salinity Normalization Approach

Some analyses in the following sections required normalization of data to a constant salinity. Various studies have used a simple technique to normalize data (e.g., normalization to a constant salinity of 35, such as described by Millero et al. 1998), but Friis et al. (2003) pointed out that this technique can lead to erroneous results if a non-zero TA intercept is present, as was the case in this study. We adopted the approach of

Friis et al (2003) to calculate salinity-normalized TA (nTA) and DIC (nDIC) according to the following:

$$nTA = \left\{\frac{TA_{obs} - TA_0}{S_{obs}} \times S_{mean}\right\} + TA_0 \quad (2.3)$$

$$nDIC = \left\{\frac{DIC_{obs} - DIC_0}{S_{obs}} \times S_{mean}\right\} + DIC_0 \quad (2.4)$$

where TA_{obs} and DIC_{obs} are the observed TA and DIC, TA_0 and DIC_0 are the zero-salinity TA and DIC determined from linear regression against salinity, S_{obs} is the salinity corresponding to the observation of TA or DIC, and S_{mean} is the mean salinity of all observations used in the linear regression.

2.2.3 Linear Regression Analysis

Linear regression analysis of TA and DIC against salinity was performed using an iteratively weighted least-squares algorithm with a bisquare function to weight outliers and robust fitting options enabled (*fitlm* in Matlab®, Mathworks, Natick MA USA). This returned two linear coefficients: the change in TA or DIC per unit salinity (i.e., slope, designated "TA:S" or "DIC:S" hereafter) and the TA or DIC calculated at salinity zero (i.e., intercept, designated "TA_0" and "DIC_0", respectively).

2.2.4 Performance of the Contros HydroFIA® TA System

The HydroFIA® TA instrument collected 11,150 hourly measurements between May 2016 and November 2019. Additionally, instrument checks were performed every one to two weeks using certified reference material (CRM) obtained from the Scripps Institute of Oceanography laboratory of Dr. Andrew Dickson (Dickson et al. 2003) to support assessments of instrument stability and accuracy. A total of 80 sets of triplicate CRM checks were conducted over the study period, each prior to instrument re-calibration (see Supplementary Material Figure B.1). The magnitude of one standard deviation (σ) of the triplicate CRM checks ranged from less than 1 µmol kg^{-1} to 23.4 µmol kg^{-1}, with a mean σ of 3.8 µmol kg^{-1}. This σ is somewhat higher than that reported by Seelmann et al. (2019) for the HydroFIA® TA instrument, as well as that reported by Hunt et al. (2021) in a shipboard deployment; however, as will be shown in this work the σ from this study was adequate for resolving the dynamic TA signals at CML, both at shorter tidal and longer monthly time scales, where TA variability was greater than the mean σ by an order of magnitude or more. The mean difference between CRM measurements and the certified TA value was -2.9±19.0 µmol kg^{-1}, where the negative value indicates that the mean HydroFIA® TA values were lower than the certified CRM TA. This instrument performance was similar to those reported by Hunt et al. (2021) and Seelmann et al. (2019) using the same instrument.

2.2.5 Mechanistic Model

To estimate the relative contributions of mixing, net ecosystem metabolism (NEM, Caffrey 2004), and air-sea flux of CO_2 to changes in TA and DIC, we used a mechanistic model modified from that of Pacella et al. (2018). This model calculated the partial change in TA and DIC between time t and time t+1 (in this study, from one hour to the next) due to mixing (using salinity changes and linear TA:salinity and DIC:salinity mixing relationships), NEM (in this model NEM incorporated all biologic activity, including benthic anaerobic processes) and air-sea CO_2 exchange. Briefly, this model apportioned changes in DIC according to:

$$[DIC]_{t+1} = [DIC]_t + \Delta[DIC]_{Mixing} + \Delta[DIC]_{NEM} + \Delta[DIC]_{Gas} \quad (2.5)$$

where $[DIC]_{t+1}$ is the DIC concentration at time t+1, $[DIC]_t$ is the DIC concentration at time t, $\Delta[DIC]_{Mixing}$ is the change in the DIC concentration from time t to time t+1 due to mixing, $\Delta[DIC]_{NEM}$ is the change due to NEM, and $\Delta[DIC]_{Gas}$ is the change due to the air-sea flux of CO_2. Changes in TA were apportioned similarly, with no air-sea flux term:

$$[TA]_{t+1} = [TA]_t + \Delta[TA]_{Mixing} + \Delta[TA]_{NEM} \quad (2.6)$$

where $[TA]_{t+1}$ is the TA concentration at time t+1, $[TA]_t$ is the TA concentration at time t, $\Delta[TA]_{Mixing}$ is the change in the TA concentration from time t to time t+1 due to mixing and $\Delta[TA]_{NEM}$ is the change due to NEM. The terms $\Delta[DIC]_{Mixing}$ and $\Delta[TA]_{Mixing}$ were calculated using endmember mixing between river endmember TA and DIC as discussed below and monthly mean marine TA and DIC measured at the WBD station offshore of CML, at depths greater than 20m (Supplementary B.2). The $\Delta[DIC]_{Gas}$ term was calculated using CO_2 fluxes calculated as in Hunt et al. (2013) from the observed pCO_2 data, wind velocity from a nearby weather station (National Data Buoy Center station IOSN3), and atmospheric pCO_2 values from the coastal UNH CO_2 buoy (Vandemark et al. 2011). Pacella et al. (2018) used changes in dissolved oxygen concentration from time *t* to time *t+1* to stoichiometrically calculate $\Delta[DIC]_{NEM}$ and $\Delta[TA]_{NEM}$ and thus derive $[DIC]_{t+1}$ and $[TA]_{t+1}$. However, using changes in dissolved oxygen to estimate NEM-driven changes to DIC has been shown to be problematic (Van Dam et al. 2019). The availability of hourly measurements in this study provided observed values of $[DIC]_t$, $[DIC]_{t+1}$, $[TA]_{t+1}$, *and* $[TA]_{t+1}$, and allowed calculation of $\Delta[DIC]_{NEM}$ and $\Delta[TA]_{NEM}$.

2.3 Results

2.3.1 Observed Conditions

Conditions at CML during the study period were strongly seasonal: colder and fresher in the winter and spring, and warmer and saltier in the summer and fall (Figure

2.2, Table 2.2). The coldest monthly average water temperature was in February, while the lowest monthly average salinity was in April; the highest average water temperature was in August, while the highest average salinity was in September. Vigorous semidiurnal tidal exchanges between the coastal ocean and Great Bay produced clear temperature and salinity differences at CML between high and low tides. Differences sometimes exceeded 5°C in temperature and 5 in salinity over the tidal cycle. Salinity variability was greatest in the late winter and spring, when seasonal storms and melting snowpack brought more fresh water into Great Bay that mixed with saltier coastal water, but summer or fall storms also produced periods of high episodic salinity variability. For instance, salinity increased over 8 between low and high tides during late winter and spring of 2018, and by 9 during a period in spring 2019. In contrast, late summer and fall typically had fewer storms and drier conditions, which resulted in much less salinity variability during these seasons. For example, in the fall of 2016 the salinity change between high and low tides was as little as 0.15-0.3 when Great Bay received very little fresh water. Similarly, in the fall of 2017 salinity changed by about 0.7 between tides. The smallest tidal salinity difference was 0.02, on September 9, 2016; the largest tidal salinity difference was 8.7 on March 4, 2017. The generally dry conditions in fall were reflected in the low standard deviations for salinity from July through October, while wetter spring conditions were reflected in high salinity standard deviations from March through May (Table 2.2).

Table 2.2: Monthly mean values, with standard deviation and range (in parentheses) of water temperature, salinity, pCO_2, and TA measured at the CML site from 2016-2019.

	Water Temperature (°C)	Salinity	pCO_2 (µatm)	TA (µmol kg^{-1})
Jan	4.53 ± 1.49 (1.80-7.71)	29.9 ± 1.6 (26.0-32.1)	401 ± 14 (359-439)	2069 ± 92 (1841-2223)
Feb	3.75 ± 0.75 (2.06-5.83)	30.2 ± 1.6 (23.7-32.1)	372 ± 24 (270-420)	2077 ± 86 (1679-2207)
Mar	3.97 ± 0.60 (1.75-5.64)	29.4 ± 2.0 (22.6-32.2)	343 ± 42 (218-434)	2021 ± 125 (1564-2199)
Apr	8.25 ± 0.75 (6.86-9.51)	26.3 ± 2.2 (22.4-30.4)	324 ± 24 (288-361)	1815 ± 139 (1523-2073)
May	9.74 ± 1.44 (6.12-12.95)	28.1 ± 2.0 (22.9-31.1)	423 ± 40 (333-520)	1947 ± 124 (1610-2150)
Jun	12.51 ± 1.85 (8.40-17.71)	29.1 ± 1.6 (23.0-31.2)	464 ± 58 (321-807)	2023 ± 90 (1634-2194)
Jul	15.93 ± 2.24 (9.53-20.1)	30.0 ± 0.6 (27.1-31.3)	556 ± 73 (402-969)	2057 ± 57 (1800-2196)
Aug	16.62 ± 1.93 (12.16-20.60)	31.0 ± 0.5 (29.6-31.8)	602 ± 86 (390-973)	2092 ± 36 (1991-2206)
Sep	16.26 ± 1.90 (12.23-20.12)	31.7 ± 0.1 (31.1-32.0)	659 ± 114 (423-858)	2131 ± 26 (2055-2187)
Oct	13.94 ± 1.06 (11.97-15.76)	31.5 ± 0.5 (28.5-32.1)	598 ± 59 (459-730)	2120 ± 36 (1947-2201)
Nov	9.82 ± 1.28 (8.27-12.94)	31.0 ± 0.8 (28.7-32.3)	585 ± 94 (407-815)	2120 ± 52 (1962-2213)
Dec	7.49 ± 1.33 (4.63-10.16)	30.5 ± 1.2 (27.4-32.1)	426 ± 22 (376-485)	2103 ± 74 (1694-2209)

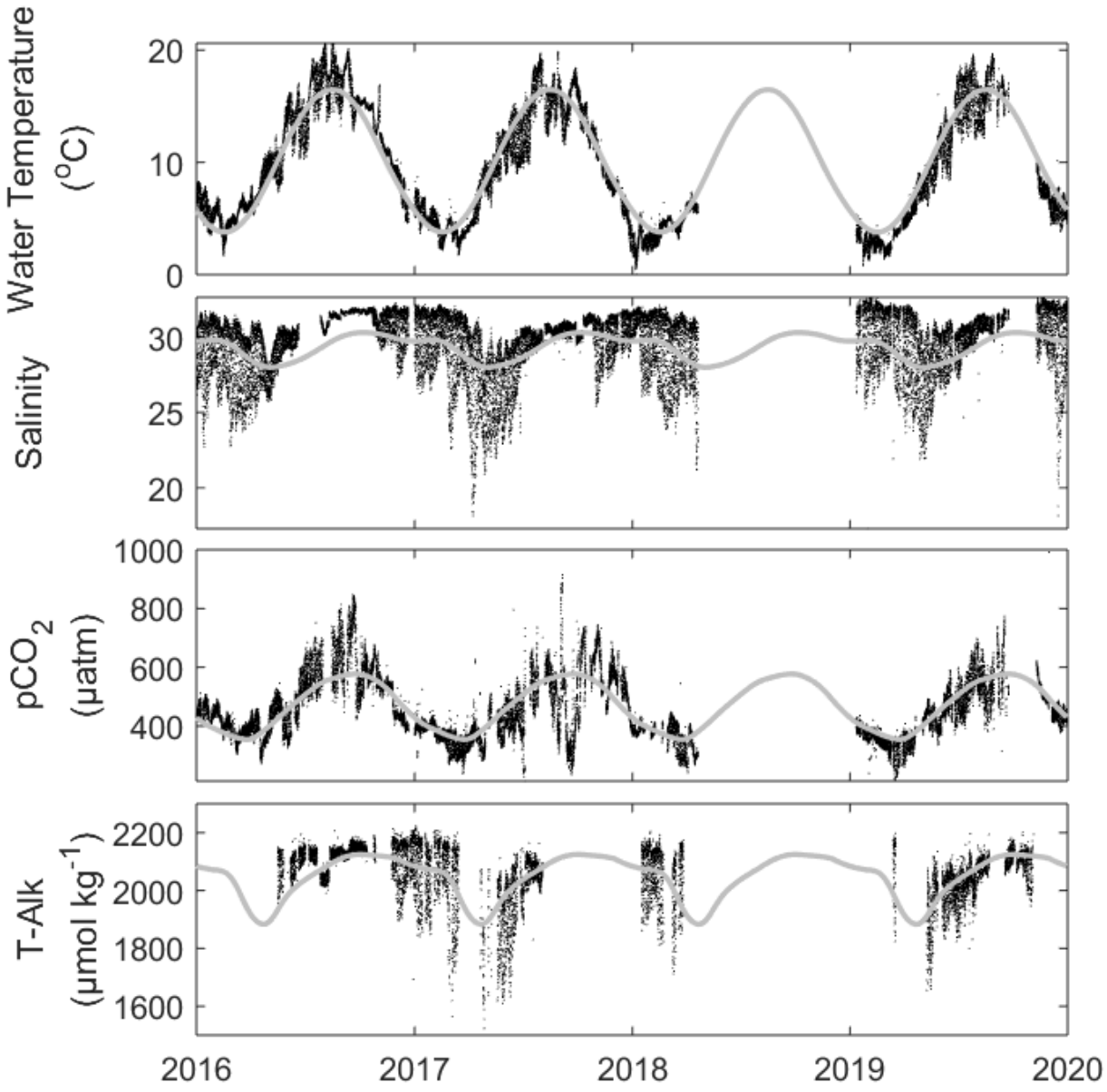

Figure 2.2: Coastal Marine Laboratory hourly timeseries plots, from top to bottom, of: water temperature, salinity, pCO_2, and TA (black markers) measured from 2016-2019. Grey lines depict annual climatologies, calculated from monthly averages of data from 2005-2019, except for TA data which were only collected from 2016 through 2019. All monthly climatologies were smoothed over 60 days ('smooth' function, Matlab®, Mathworks Natick MA USA).

Monthly mean pCO_2 dropped from 401 µatm in January to annual low values in March and April indicating net estuary productivity (343 and 324 µatm, respectively), then rose steadily to an annual high of 659 µatm indicating net estuary respiration in August before dropping through the fall to 426 µatm in December. In contrast to salinity, pCO_2 variability was highest when salinity variability was lowest, as seen during the late summer and fall in 2016, when pCO_2 variability over the tidal cycle reached 400 µatm in September, and again in the fall of 2019 when the same variability reached 350 µatm (Figure 2.2). This pattern was reflected in larger pCO_2 standard deviations from July to November and smaller pCO_2 standard deviations from December to May (Table 2.2). While pCO_2 was generally higher at low tide, there were periods each year when pCO_2 at low tide was lower than at high tide, typically during spring months.

TA concentrations followed salinity, with higher TA associated with higher salinity, and higher tidal TA variability associated with periods of higher salinity variability. Monthly average TA was highest in September (2131 µmol kg^{-1}), which was also the month of lowest TA variability as measured by the standard deviation of monthly data (Figure 2.2, Table 2.2) and highest average salinity. The largest tidal TA difference, as measured by the difference between TA at high tide and TA at the subsequent low tide, was 578 µmol kg^{-1} on March 4, 2017; the smallest tidal TA difference was 0.1 µmol kg^{-1} on October 4, 2019. While infrequent, there were periods when the TA at high tide was lower than that on the subsequent low tide, generally in summer or fall (there were no such periods of lower salinity at high tide than low tide, however). The monthly average TA was lowest in April (1815 µmol kg^{-1}), which was the month of lowest average salinity (26.3) and highest TA variability (Table 2.2), but also

the fewest monthly TA measurements (Table 2.4). The monthly co-variation of TA with salinity was not perfect. For instance, although March had the second-highest hourly salinity at CML (32.2) the corresponding TA was not particularly high (2159 µmol kg^{-1}). Indeed, the highest observed TA (2223 µmol kg^{-1}, in January 2017) was measured at a salinity of 32.1. Monthly mean, salinity-normalized TA (nTA, normalized to a dataset mean salinity of 29.95) was highest in January (2071 µmol kg^{-1}), dropped each successive month to an annual low in April (nTA 2018 µmol kg^{-1}), then increased to another annual high value in June (2068 µmol kg^{-1}). During the latter half of the year monthly nTA remained between 2036 and 2061 µmol kg^{-1} (Supplementary Table B.1).

2.3.2 Derived Parameter Conditions

DIC concentrations followed the general patterns of salinity and TA, with higher DIC found at higher salinities. The highest average monthly DIC was in September (2017 µmol kg^{-1}), while October was the month of lowest DIC variability (±29 µmol kg^{-1}, Figure 2.3, Table 2.3). The lowest average monthly DIC was in April (1710 µmol kg^{-1}), also the month of highest DIC variability (±124 µmol kg^{-1}). Low DIC in April due to the annual spring phytoplankton bloom coincided with the highest monthly average pH calculated at 25°C ($pH_{25°C}$ 7.82), while the lowest monthly average $pH_{25°C}$ was in January (7.72). As pH is strongly affected by temperature, results of pH at *in-situ* temperature ($pH_{in\text{-}situ}$) were quite different, with the lowest $pH_{in\text{-}situ}$ in September (7.85) and the highest $pH_{in\text{-}situ}$ in March (8.06). ß-H was highest, and thus buffering was

strongest, in August (376 µmol kg^{-1}) and weakest in April (326 µmol kg^{-1}). The lowest monthly average ß-H in April coincided with the second-freshest month (average salinity 28.6), while the second-lowest monthly ß-H in May (332 µmol kg^{-1}) coincided with the lowest average monthly salinity (28.1). While August was the month of strongest buffering, it was not the month of highest salinity (which was September/October); however, August was the month of highest average water temperature (16.4 °C). Monthly mean, salinity-normalized DIC (nDIC, normalized to a dataset mean salinity of 29.95) was highest in January and February (1957 and 1955 µmol kg^{-1}, respectively) and lowest in April (1889 µmol kg^{-1}) in a similar pattern to nTA. The nDIC for months from May to December ranged between 1913 µmol kg^{-1} (in August) and 1947 µmol kg^{-1} in November.

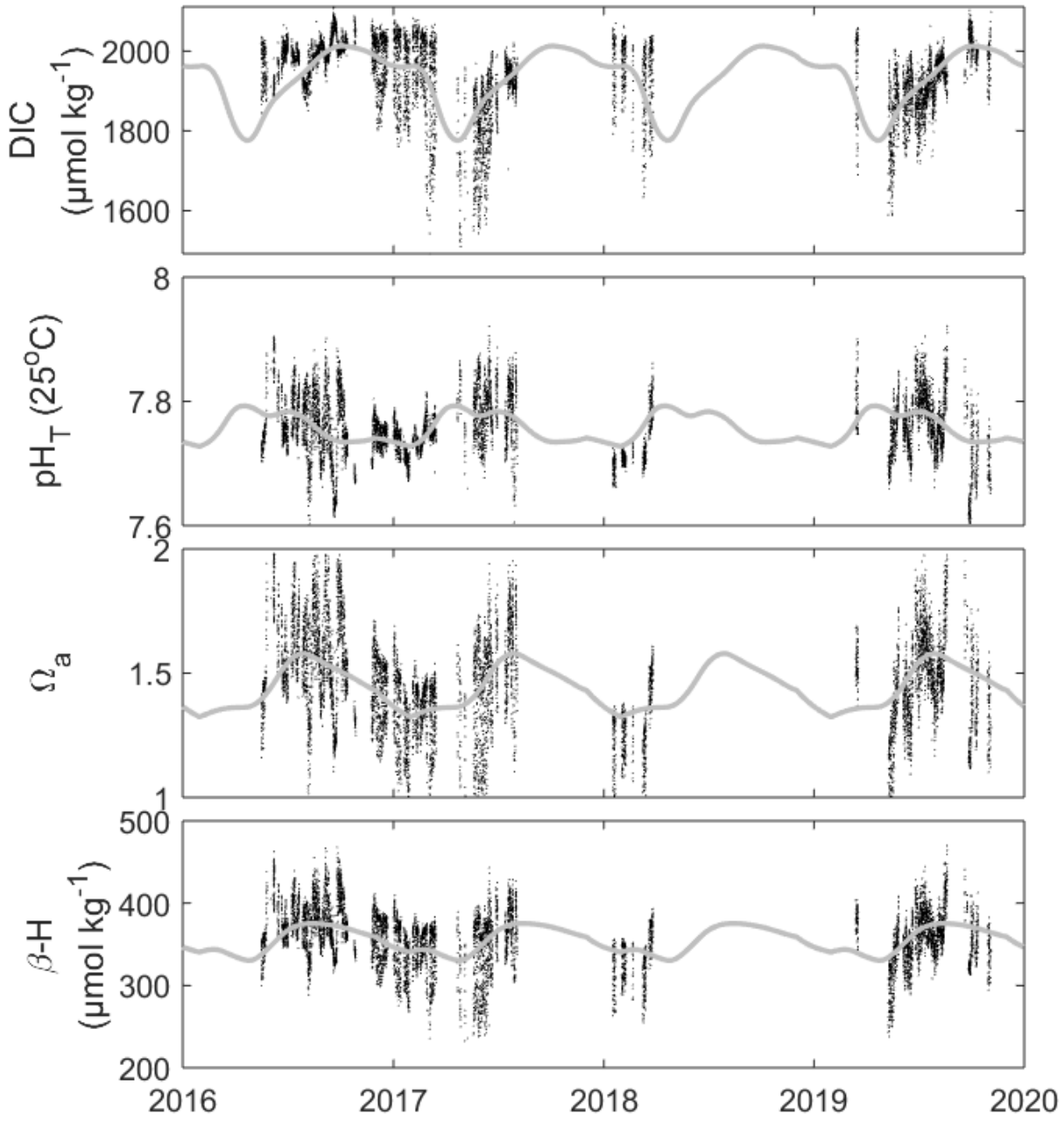

Figure 2.3: Coastal Marine Laboratory hourly timeseries plots, from top to bottom, of calculated parameters: dissolved inorganic carbon (DIC), pH on the total scale at 25°C, aragonite saturation state (Ω_a), and the buffering factor β-H. See text for details of the calculation of these parameters from *in situ* measurements of salinity, temperature, pCO_2 and TA. Grey lines depict annual climatologies, calculated from monthly averages of data from 2016-2019. See Appendix B for further detail regarding the preparation of climatologies.

Table 2.3: Monthly mean values, with standard deviation and range (in parentheses), of derived variables DIC, pH and β-H. Note that larger values of β-H indicating higher buffering capacity.

	Dissolved Inorganic Carbon ($\mu mol\ kg^{-1}$)	pH (Total scale, 25°C)	pH (Total scale, in situ temperature)	β-H ($\mu mol\ kg^{-1}$)
Jan	1956 ± 81 (1761-2077)	7.723 ± 0.030 (7.625-7.874)	8.003 ± 0.016 (7.958-8.040)	-146 ± 14 (-178, -114)
Feb	1969 ± 77 (1590-2082)	7.736 ± 0.034 (7.687-7.952)	8.035 ± 0.018 (7.988-8.098)	-150 ± 9 (-168,-117)
Mar	1907 ± 115 (1492-2065)	7.758 ± 0.038 (7.620-7.900)	8.059 ± 0.042 (7.966-8.201)	-150 ± 15 (-175,-102)
Apr	1710 ± 124 (1510-1932)	7.819 ± 0.028 (7.768-7.865)	8.051 ± 0.031 (7.988-8.104)	-142 ± 16 (-169,-108)
May	1837 ± 110 (1544-2035)	7.764 ± 0.046 (7.659-7.877)	7.972 ± 0.045 (7.858-8.075)	-144 ± 17 (-191,-101)
Jun	1892 ± 84 (1566-2065)	7.785 ± 0.051 (7.593-7.921)	7.955 ± 0.051 (7.712-8.096)	-156 ± 17 (-201,-104)
Jul	1924 ± 56 (1704-2063)	7.786 ± 0.043 (7.605-8.011)	7.899 ± 0.048 (7.687-8.017)	-163 ± 10 (-193,-132)
Aug	1964 ± 36 (1850-2073)	7.764 ± 0.053 (7.545-7.921)	7.874 ± 0.055 (7.671-8.034)	-164 ± 12 (-204,-125)
Sep	2017 ± 38 (1823-2111)	7.736 ± 0.082 (7.589-8.119)	7.848 ± 0.071 (7.735-8.015)	-162 ± 17 (-203,-136)
Oct	2011 ± 29 (1868-2095)	7.734 ± 0.049 (7.546-7.891)	7.877 ± 0.040 (7.787-7.984)	-161 ± 11 (-191,-128)
Nov	2003 ± 42 (1879-2098)	7.735 ± 0.038 (7.652-7.804)	7.944 ± 0.052 (7.826-8.022)	-157 ± 12 (-179,-131)
Dec	1974 ± 64 (1802-2067)	7.745 ± 0.015 (7.710-7.784)	7.990 ± 0.020 (7.942-8.031)	-155 ± 11 (-174,-130)

2.4 Discussion

2.4.1 TA and DIC Mixing

TA can be a useful tracer of conservative river-ocean mixing in estuaries and coastal waters (Howland et al. 2000, Cai et al. 2010, Wang et al. 2013), as it is unchanged by CO_2 exchange with the atmosphere. Unlike DIC, changes in which can indicate biological uptake or release of CO_2, pairing TA with salinity often yields a nearly conservative behavior in an estuary system (Salisbury et al. 2009). However, there is increasing evidence that estuarine biogeochemical processes can influence TA as well as DIC, producing nonconservative TA mixing as well as nonconservative DIC mixing (Raymond et al. 2000, Cai et al. 2017, Wang et al. 2016, Sippo et al. 2016).

Linear regression of all the CML TA measurements against salinity (Figure 2.4) yielded a regression slope of 53.8±0.2 μmol kg^{-1} and zero-salinity intercept (TA_0, Equation 2.2) of 442±6 μmol kg^{-1}, with an RMSE of 34.8 μmol kg^{-1} (r^2 0.87, $p<<0.001$). There was also a strong linear relationship between DIC and salinity (Figure 2.4), with a regression slope of 50.3±0.2 μmol kg^{-1} and zero-salinity intercept (DIC_0, Equation 2.3) of 428±6 μmol kg^{-1}, with an RMSE of 36.4 μmol kg^{-1} (r^2 0.84, $p<<0.001$). The relatively high RMSE values indicate that there was considerable variability in the TA-salinity and DIC-salinity relationships at CML, either due to changes in water mass mixing, biogeochemical processes, or (in the case of DIC) air-sea exchange. This is evident in Figure 2.4, as considerable scatter of TA and DIC both above and below the linear regression lines. To set reasonable bounds for how much of this variability might be due to variable river inputs of TA and DIC, we used the river endmember data reported by

Hunt et al. (2011a) for three rivers draining to Great Bay to estimate the mean and one standard deviation uncertainty of river TA (507±270 µmol kg^{-1}) and DIC (644±308 µmol kg^{-1}). Upper and lower conservative river mixing bounds were thus calculated using the values of Hunt et al. (2011a) and a theoretical ocean endmember calculated from the linear regression of all the TA and DIC observations (Figure 2.4).

River TA and DIC concentrations vary considerably with season and discharge, leading to a range of river-ocean mixing lines through time (Najjar et al. 2020, Joesoef et al. 2017, Hunt et al. 2011b). While this was likely true in the CML data as well, and thus some amount of the variability of TA and DIC above and below the river mixing lines in Figure 2.4 was due to changing river endmember TA and DIC, a substantial number of TA and DIC observations at CML were still above or below the bounds of this theoretical river mixing. This indicates that some of the TA and DIC variability is likely due to another process or combination of processes in addition to conservative river mixing. Another indication of estuary modification of TA and DIC was the finding that the regressed CML TA_0 (442±6 µmol kg^{-1}) was higher than the regressed DIC_0 (428±6 µmol kg^{-1}). In contrast, measured river DIC was always higher than the corresponding river TA (Hunt et al. 2011a,b). While the TA_0 of 442 was slightly lower than the mean river TA (507 µmol kg^{-1}), the DIC_0 of 428 µmol kg^{-1} was substantially lower than the mean river DIC (644 µmol kg^{-1}). This discrepancy supports the idea that river-borne TA and DIC are processed non-conservatively and in different proportions in Great Bay before reaching CML. Specifically, while there may be a small amount of overall TA removal, the amount of DIC removal appears to be much larger.

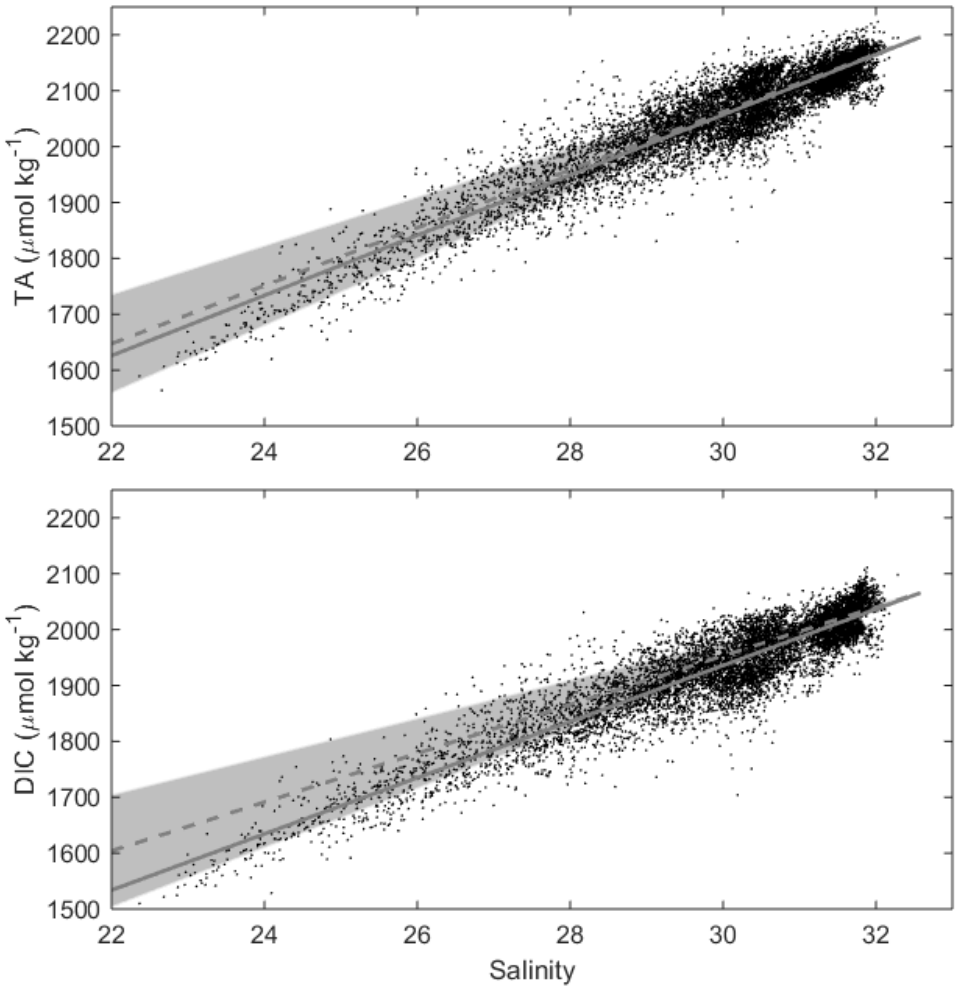

Figure 2.4: CML TA (top panel) and DIC (bottom panel) distributions with salinity for data collected from 2016-2019. The TA measurements were made by the HydroFIA® TA instrument, while DIC was derived from measured TA and pCO_2 (refer to the text for the calculation description). The solid grey lines show the linear regression of all TA or DIC observations against salinity. The dotted grey lines show the conservative mixing of mean river TA or DIC from Hunt et al. (2011a) with a coastal ocean endmember (calculated as the TA or DIC from the solid linear regression line at the maximum observed salinity of 32.58). The grey shaded area represents the upper and lower bounds of river and coastal ocean conservative mixing. The bounds for the river endmembers were defined as one standard deviation above and below the mean TA and DIC for the three Great Bay rivers reported by Hunt et al. (2011a), while the bounds for the ocean endmember were obtained from subsurface data offshore of CML.

Table 2.4: Monthly robust linear regression statistics for TA and DIC against salinity.

Year	Month	Salinity Range	TA-salinity Slope	TA-salinity Intercept	TA-salinity r^2	TA-salinity n	TA-salinity RMSE	DIC-salinity Slope	DIC-Salinity Intercept	DIC-salinity r^2	DIC-salinity n	DIC- salinity RMSE
2016	May	3.3	63 ± 1.6	206 ± 47	0.91	158	15	56 ± 1.1	324 ± 34	0.94	158	11
2016	Jun	2.3	65 ± 1.6	135 ± 48	0.75	566	18	65 ± 4.3	-1 ±130	0.35	434	40
2016	Jul	0.7	75 ± 12.8	-171 ± 389	0.07	467	41	52 ± 12.8	376 ±390	0.04	426	39
2016	Aug	2.1	82 ± 1.4	-448 ± 43	0.84	655	17	66 ± 1.8	-72 ±55	0.68	652	22
2016	Sep	0.5	151 ± 3.0	-2627 ± 95	0.79	690	9	193 ± 9.9	-4105 ± 313	0.37	664	29
2016	Oct	1.2	43 ± 3.2	774 ± 102	0.35	337	13	-0.03 ± 4.3	2017 ± 134	0.03	336	17
2016	Nov	2.7	59 ± 0.6	296 ± 20	0.98	166	6	45 ± 1.3	594 ± 41	0.88	164	13
2016	Dec	4.8	61 ± 0.4	221 ± 13	0.98	463	11	52 ± 0.4	392 ± 14	0.97	459	11
2017	Jan	5.9	61 ± 0.6	234 ± 19	0.95	530	22	52 ± 0.5	385 ± 14	0.96	507	16
2017	Feb	8.4	58 ± 0.5	336 ± 16	0.96	484	17	54 ± 0.5	323 ± 15	0.96	479	16
2017	Mar	9.3	65 ± 0.3	115 ± 9	0.99	280	12	59 ± 0.3	160 ± 10	0.99	279	12
2017	Apr	8.1	61 ± 0.6	236 ± 17	0.99	57	11	54 ± 0.7	293 ± 17	0.99	57	11
2017	May	7.1	62 ± 0.4	199 ± 11	0.99	293	14	51 ± 0.6	405 ± 16	0.96	291	19
2017	Jun	7.6	56 ± 0.8	392 ± 23	0.89	560	35	47 ± 0.7	525 ± 21	0.88	557	31
2017	Jul	3.2	44 ± 2.3	765 ± 68	0.39	660	30	3 ± 3.5	1845 ± 105	0.00	385	28
2017	Aug	8.9	5 ± 10.1	1914 ± 305	-0.01	64	19	-3 ± 15.6	2031 ± 470	-0.02	63	29
2018	Jan	5.9	47 ± 0.7	686 ± 22	0.92	334	24	36 ± 1.5	905 ± 45	0.83	109	29
2018	Feb	8.2	47 ± 0.7	643 ± 20	0.92	450	24	35 ± 0.7	910 ±23	0.91	209	16
2018	Mar	8.1	60 ± 0.8	259 ± 23	0.95	303	23	55 ± 0.6	300 ± 17	0.97	298	18
2019	Mar	7.3	62 ± 1.2	200 ± 36	0.97	96	19	62 ± 1.3	61 ± 38	0.96	96	20
2019	May	7.9	54 ± 1.4	412 ± 40	0.79	393	48	46 ± 1.4	524 ± 39	0.75	393	47
2019	Jun	5.0	48 ± 1.1	576 ± 33	0.79	494	29	40 ± 1.4	714 ± 40	0.64	494	36
2019	Jul	4.1	45 ± 1.8	668 ± 55	0.47	703	38	41 ± 1.8	665 ± 55	0.42	703	38
2019	Aug	1.8	46 ± 1.8	669 ± 55	0.62	415	14	32 ± 2.9	967 ± 90	0.23	415	24
2019	Sep	1.0	89 ± 5.6	-698 ± 178	0.63	149	16	113 ± 12.5	-1544 ± 396	0.40	127	31
2019	Oct	4.0	45 ± 1.4	704 ± 45	0.64	544	23	33 ± 2.7	954 ± 85	0.40	221	27
2019	Nov	5.3	57 ± 1.9	333 ± 59	0.95	43	13	51 ± 2.4	420 ± 74	0.91	43	16

2.4.2 Seasonal Changes in TA and DIC Mixing Patterns

The hourly measurement rate at CML allowed for highly-resolved data collection over long periods of time. To examine temporal shifts in the conservative mixing of TA and DIC with respect to salinity, we constructed monthly linear regressions for the 27 months with sufficient data collection from 2016-2019 (Table 2.4). Of these 27 months, 19 TA-salinity regressions returned zero-salinity intercepts that were within the TA river-mixing bounds discussed previously, while 16 months had DIC-salinity regressions with zero-salinity intercepts that were within the DIC river-mixing bounds. Taking results from all sampled months, the mean TA-salinity regression slope was 60.0 μmol kg^{-1} (±24 μmol kg^{-1}, one standard deviation), while that of DIC-salinity was 51.5 μmol kg^{-1} (±36 μmol kg^{-1}, one standard deviation). The TA-salinity slope was higher than the corresponding DIC-salinity slope for 22 of the 27 months in Table 2.4, again indicating stronger estuary removal or decreases of DIC. The mean TA-salinity slope was similar to the slope of 65.8 described by Cai et al. (2010) for a transect whose inshore leg began very near CML in August 2007. However, Cai et al. (2010) reported a zero-salinity TA intercept of -188.7 μmol kg^{-1}, a value which clearly requires some mechanism of TA removal to explain.

The strongest linear correlations between TA and salinity or DIC and salinity, according to the r^2 statistic, tended to be in the winter (December, January, February) and spring months (March and May), while the weaker r^2 statistics in summer and fall months indicated that mixing was less conservative. The winter and spring months also tended to have TA-salinity regression slopes near the mean value (60.0), while the

summer and fall months showed widely varying TA-salinity slopes (ranging from 5.0 to 150). However, it should be noted that the summer and fall months were also those with lowest river flow and range of salinity change, and therefore the less robust salinity mixing relationships for these months were not surprising. For example, in September 2016 the salinity range was only 0.5; considering the overall mean TA-salinity slope of 53.8 this translated into a potential TA variability of half the slope, or 26.9 μmol kg^{-1}. This was only somewhat higher that the overall uncertainty in the TA instrument accuracy (±18 μmol kg^{-1}), indicating that in months of very low salinity variability the TA instrument may not be capable of determining a meaningful TA-salinity relationship. But it is worth noting that while the overall accuracy uncertainty over the study period was ±18 μmol kg^{-1}, in September 2016 the uncertainty in instrument accuracy was smaller (±11 μmol kg^{-1}, n=3), allowing for meaningful interpretation of the results despite the small salinity changes in this and other months (Appendix Figure B.1). Other summer and fall months, such as June and August 2016 as well as June and August 2019 when the salinity range was larger, had relatively high r^2 values, and were still much different in the slope and intercept terms. Despite the added uncertainty in TA-salinity and DIC-salinity regressions in the summer and fall months, there appeared to be other factors contributing to TA and DIC observations.

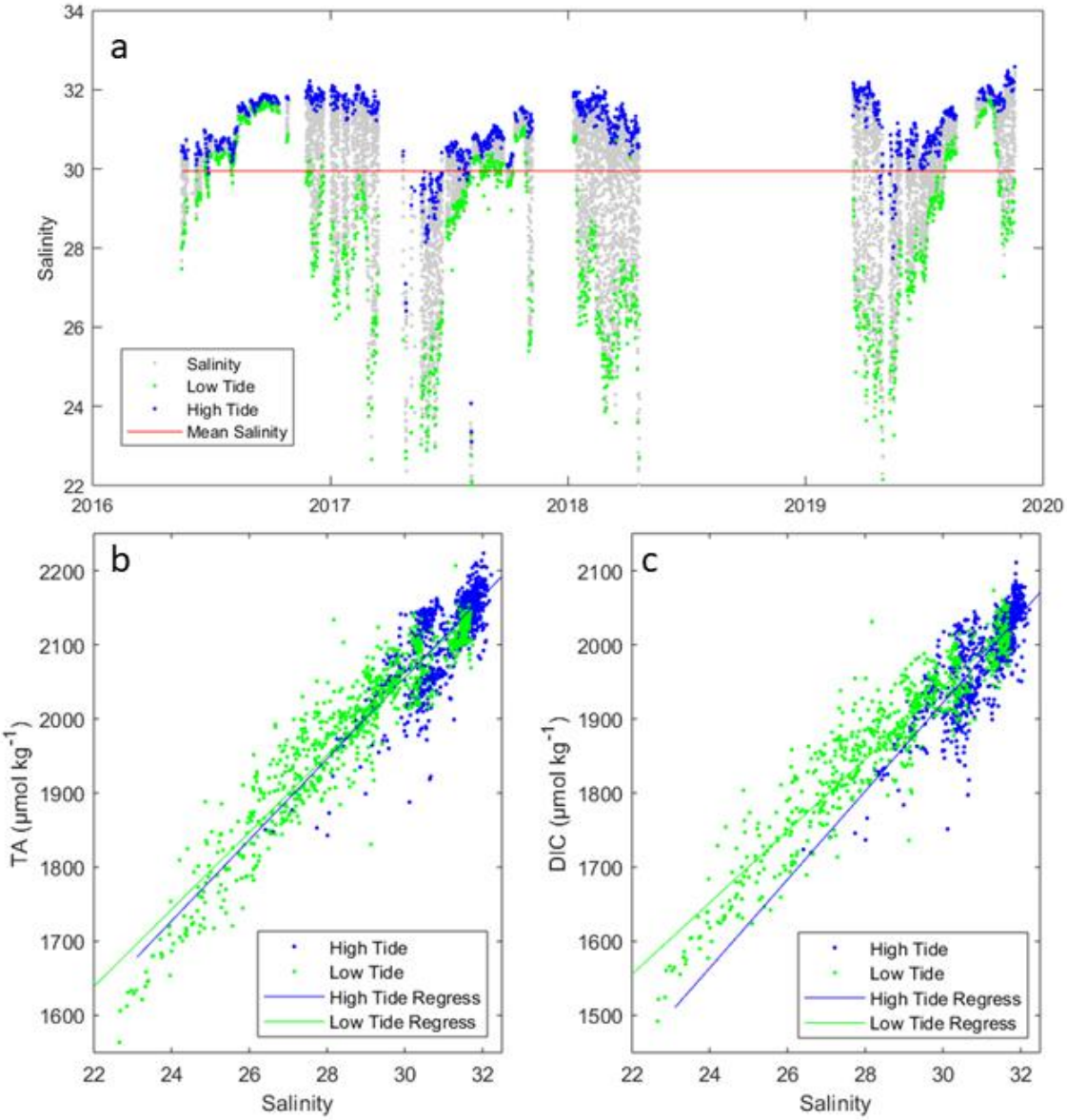

Figure 2.5: CML salinity timeseries (panel a) with high tide readings shown in blue, low tide readings shown in green, and mid-tide readings shown in grey. See the text for discussion regarding the identification of high and low tide points. The linear regression of salinity against high and low tide TA is shown in panel b. The regression equation for high tide TA against salinity is $TA_{high\ tide}$=Sx54.7(±1.4) + 415(±43) with r^2=0.65; that for the low tide TA is $TA_{low\ tide}$=Sx52.0(±0.6) + 495(±18) with r^2=0.89. The linear regression of salinity against high and low tide DIC is shown in panel c. The regression equation for high tide DIC against salinity is $DIC_{high\ tide}$=Sx59.6(±1.5) + 133(±47) with r^2=0.68; that for the low tide DIC is $DIC_{low\ tide}$=Sx48.3(±0.6) + 492(±18) with r^2=0.89.

2.4.3 High and Low Tide TA and DIC

Tidal exchanges between the coastal ocean and Great Bay are very strong, funneling large volumes of water past CML over each diurnal cycle. One study estimated a Great Bay flushing time of 2.5-7 days (Matso 2018), while another gave a range of 5-30 days depending on tidal stage and river discharge (Bilgili et al. 2005). Both studies show that much of the water in Great Bay is replaced over each tide. As the predominant coastal flow outside of CML is southward (Townsend 2006), the water which passes CML on the incoming tide is mostly advected south on the subsequent outgoing tide instead of re-entering Great Bay on the next tide. Therefore, we suggest that a simplistic conceptual model for each tidal cycle can be represented by “newer” coastal water entering the estuary past CML on the incoming tide, mixing with a pool of estuary water comprised of a combination of river and “older” coastal water, and then exiting past CML again on the outgoing tide. As data collection at CML was hourly, it is useful to examine the differences in the TA and DIC compositions of water at CML at high and low tides, where high tide presumably represents the greatest fraction of coastal water, and low tide represents the greatest fraction of mixed estuary water. We used salinity to identify high and low tides (as opposed to the observed tidal stage height) and the corresponding high and low tide TA and DIC (Figure 2.5) by first identifying the lowest salinity measurement within a seven-hour time frame of data (“findpeaks”, MATLAB, Mathworks Natick MA), then searching the previous nine hours for the highest salinity. We chose to employ this strategy due to a mismatch between the time of lowest tidal height and the time of lowest salinity, where the lowest salinity

was observed multiple hours after the lowest tidal height observation. This apparent asymmetry between tidal elevation and salinity is due to the dissipation of the energy of the tidal wave as it moves past CML and proceeds upstream, resulting in the phase of the tidal flow lagging that of the elevation (T. Lippmann, pers. comm.). Thus, while our salinity-based identification method did not strictly correspond to the technical definitions of high and low tides relative to sea surface height, we will use the common terms high and low tide henceforth to refer to the times of highest and lowest salinity during each diurnal tidal cycle.

By employing the method described above, the salinity, TA, and DIC were identified at high and low tide throughout the dataset. Linear regression of high and low tide TA against salinity yielded statistically similar results (Figure 2.5), indicating that there did not appear to be a significant change in TA in the water leaving Great Bay past CML on the outgoing tide relative to water entering past CML on the incoming tide. Additionally, the TA_0 for high and low tides (415±43 µmol kg^{-1} and 495±18 µmol kg^{-1}, respectively) were well within the wide river endmember TA range (507±270 µmol kg^{-1}). However, linear regression of DIC against salinity produced different regression lines for high and low tide, with the low tide DIC having a steeper linear slope and higher DIC_0 than those from the high tide measurements, indicating a relative input of DIC to the water leaving Great Bay past CML on the outgoing tide. The low tide DIC_0 (492±18 µmol kg^{-1}) is also much closer to the approximate river endmember DIC (644±308 µmol kg^{-1}) than the corresponding high tide DIC_0 (133±47 µmol kg^{-1}).

2.4.4 Seasonal pCO_2 Dynamics and Effects on Buffering

Seasonal pCO_2 patterns have been documented at a buoy (WBD) located 12km offshore of CML (Vandemark et al. 2011), showing a strong CO_2 drawdown in the spring and gradual efflux in the fall and winter. April was the month of strongest CO_2 drawdown at WBD, matching results from CML and indicating that the timing of the spring pCO_2 minimum is a regional phenomenon and not specific to CML. Peak CO_2 at WBD was typically in October or later, while that at CML was somewhat earlier in September. In general, pCO_2 at CML followed the seasonal patterns seen at WBD, but with higher overall pCO_2: the minimum buoy pCO_2 in April was typically lower than the corresponding minimum value at CML, while maximum WBD pCO_2 in the fall was also lower than the CML value. A study of spring, summer and fall pCO_2 distributions in three of the Great Bay tributaries also showed the same seasonal progression, with low pCO_2 in April and higher values in October (Hunt et al. 2011a). This study also estimated that river-borne DIC contributions to estuary DIC were usually much larger than the DIC contributed by the estuary itself, with the exception of April when estuary DIC drawdown was nearly equal to the river DIC input.

The strong spring CO_2 drawdown is due to the well-known regional spring bloom (Townsend et al. 2006). Intense primary productivity should stoichiometrically remove DIC and contribute a smaller amount of TA (Table 2.1), a phenomenon reflected by the highest pH and lowest DIC also occurring in April, the minimum DIC being due to a combination of increased low-DIC freshwater and biological drawdown of CO_2. Monthly mean TA was also lowest in April (Table 2.2), due to dilution from river mixing. The

estuary buffering reflected in β-H was also lowest in April (Table 2.3), concurrent to the highest $pH_{25°C}$ and second-highest pH_{insitu}. Fall showed the opposite trend, with higher salinity, TA, pCO_2 and DIC. The highest monthly DIC in September produced both the lowest pH_{insitu} and highest monthly β-H. While pH_{insitu} and water temperature are expected to vary inversely, lower $pH_{25°C}$ values in the fall emphasized that temperature was not the only factor contributing to the pH changes. The co-occurrence of high pH and low β-H in the spring, or low pH and high β-H in the fall, may appear to be contradictory but in fact demonstrates that β-H simply reflects the resistance of estuary pH to perturbation, and not the overall estuary pH itself. The processes which dictate seasonal β-H in an estuary, such as mixing, may be decoupled from the processes which dictate pH such as temperature or NEM. Our results indicate that mixing dictates TA, DIC, and β-H at CML, while pCO_2 and pH are more strongly influenced by strong positive net estuary and coastal production during the spring bloom, and ongoing negative net estuary metabolism through the late summer and fall as allochthonous and autochthonous organic matter is consumed in the estuary.

2.4.5 Biogeochemical Processes Affecting TA and DIC

As discussed earlier, conservative river-ocean TA mixing models are often used to estimate TA distributions in estuaries, and during the winter and spring seasons in Great Bay conservative mixing does appear to explain the general TA distributions with salinity (Figure 2.4, Table 2.4). But estuaries can also be sites of intense

biogeochemical processing, especially of allochthonous and autochthonous organic matter, which can alter TA, DIC, or both in varying proportions, depending on the stoichiometry of the chemical reaction or reactions that predominate (Borges et al. 2003, Bouillon 2007, Krumins et al. 2013, Sippo et al. 2016, Cai et al. 2017). The most common processes and their ΔDIC:ΔTA ratios are compiled from Cai et al. (2017) and Sippo et al. (2016): aerobic respiration and primary production (AR/PP, ΔTA :ΔDIC -0.16), sulfate reduction (SR, ΔTA: ΔDIC 1.0), carbonate dissolution or precipitation (CD/P, ΔTA: ΔDIC 2.0), denitrification (DN, ΔTA: ΔDIC 0.8), and iron reduction (IR, ΔTA: ΔDIC 8.0). Note that both aerobic respiration and carbonate dissolution are reversible reactions (with primary production and carbonate precipitation, respectively) and are thus named according to the forward and backward reactions. AR/PP can occur in the pelagic environment or the oxygenated benthos, while the remaining processes are components of complex anerobic biogeochemical cycling within estuarine and coastal sediments that is subsequently reflected in the overlying water, where AR/PP, SR, CD/P, and DN tend to predominate in most estuaries (Burdige 2011, Ulfsbo et al. 2011, Hagens et al. 2015). These processes may occur simultaneously or be coupled together to transport electrons through various sediment layers, and the linkage between sediment chemistry and the chemistry of the overlying water may depend on a variety of physical and biogeochemical factors (Burdige 2011, Cai et al. 2017). The chemical reaction stoichiometry for each of these reactions is listed in Table 2.1.

The linear regression of all salinity-normalized TA against salinity-normalized DIC (nTA and nDIC respectively, normalized to a S_{mean} of 29.95, Figure 2.6) yielded a nTA:nDIC slope of 0.83±0.005. This slope most closely matched the theoretical

nTA:nDIC slope of denitrification (DN, 0.8), and was shallower than the theoretical slopes for sulfate reduction (SR, 1.0), carbonate dissolution or precipitation (CD/P, 2.0) or iron reduction (8.0). This is consistent with previous work, as denitrification is thought to represent a small proportion of NEM (Bouillon et al. 2007), while PP/AR and SR are thought to be the dominant processes in systems such as Great Bay and the coastal Gulf of Maine (Köster et al. 2000, Raymond et al. 2000, Hopkinson et al. 1999). The observed slope (0.83) is somewhat lower than the theoretical slope for SR (1.0), but much higher than the slope for AR/PP (-0.16), indicating that a mixture of the SR and AR/PP processes are likely either operating sequentially or simultaneously to alter nTA:nDIC, but that SR could be the dominant process. Cai et al. (2017) modeled a mixture of aerobic respiration, SR, and carbonate dissolution in both sequential and simultaneous arrangements in order to explain oxygen and sulfide concentrations and DIC:TA changes in subsurface summertime Chesapeake Bay waters, with the simultaneous arrangement producing a closer match to their observations. Sippo et al. (2016) calculated nTA:nDIC slopes from six Australian mangrove estuaries; five of these had slopes ranging from 0.44 to 0.95 (mean slope 0.71) and good linearity (r^2>0.5, mean r^2 0.81), while one had a slope of essentially zero and poor linearity (slope 0.05, r^2 0.07). Like Cai et al. (2017), Sippo et al. (2016) invoked a combination of processes to explain their observations, specifically a combination of aerobic respiration and SR. It seems likely that an overall combination of SR and AR/PP was responsible for the nTA:nDIC observed at CML as well.

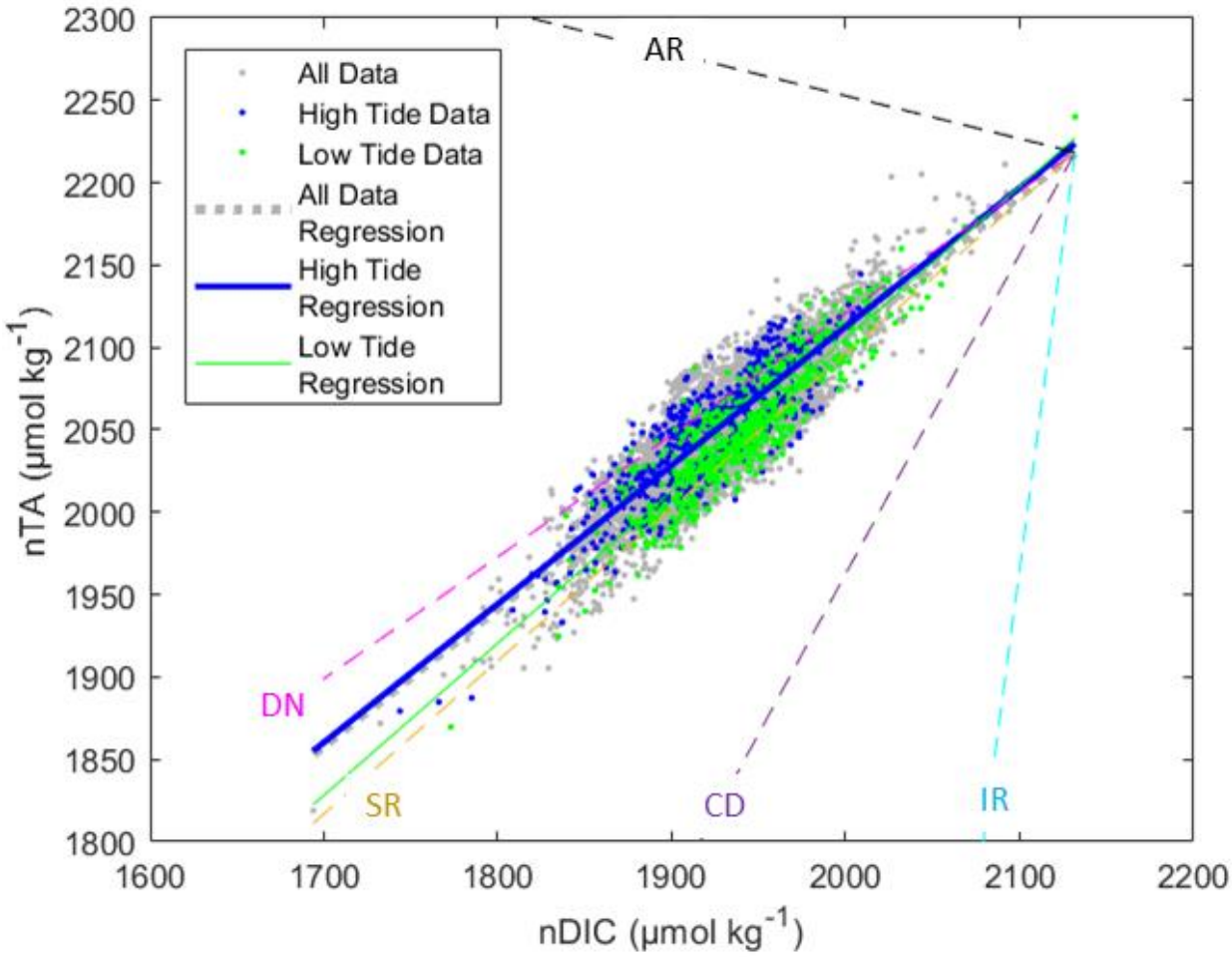

Figure 2.6: All salinity-normalized DIC (nDIC) and salinity-normalized TA (nTA) from the CML observations (gray points), with high tide data (blue points) and low tide data (green points) corresponding to those shown in Figure 2.5. Dashed lines show the stoichiometric nTA:nDIC changes for common estuarine processes: aerobic respiration (AR), denitrification (DN), sulfate reduction (SR), carbonate dissolution (CD) and iron reduction (IR). The solid blue line shows the linear regression of high tide data points (slope 0.84±0.017), while the solid green line shows that of low tide data points (slope 0.92±0.016). The linear regression of all data (dashed gray line, slope 0.83±0.005) is essentially covered by the solid blue high tide regression line.

While the overall CML nTA:nDIC regression was linear (r^2 0.75, p<0.001), there was significant scatter around the regression line (nTA RMSE 18 µmol kg^{-1}). Examination of the nTA:nDIC distributions at high and low tide showed clear differences (Figure 2.6). The high tide slope (0.84±0.017, r^2=0.77, p<0.001) was indistinguishable from the overall trend of all data and may reflect an apparent combination of SR and AR/PP. The low tide slope (0.92±0.016, r^2=0.83, p<0.001), however, was significantly steeper than the high tide slope. The steeper low tide slope was very close to the stoichiometric slope for SR (1.0), perhaps indicating that this process was a stronger contributor at low tide, a logical result as the tidal flushing out of Great Bay and past CML and consequent sea height drop results in more benthic-pelagic interaction.

In addition to differences in the nTA:nDIC slope between high and low tides, there was an evident seasonal progression of nTA:nDIC slope as well (Figure 2.7). Monthly nTA:nDIC slope values were generally between the SR and DN values, excepting a large decrease in the later summer and fall months (August through October) toward the AR value. These months were also the months of relatively high nonlinearity between nTA and nDIC as indicated by generally low r^2 values (Table 2.4). This general pattern was seen across years between 2016-2019 with some interannual variability. While there were differences between low and high tide monthly nTA:nDIC slopes, these differences were small and inconsistent between years.

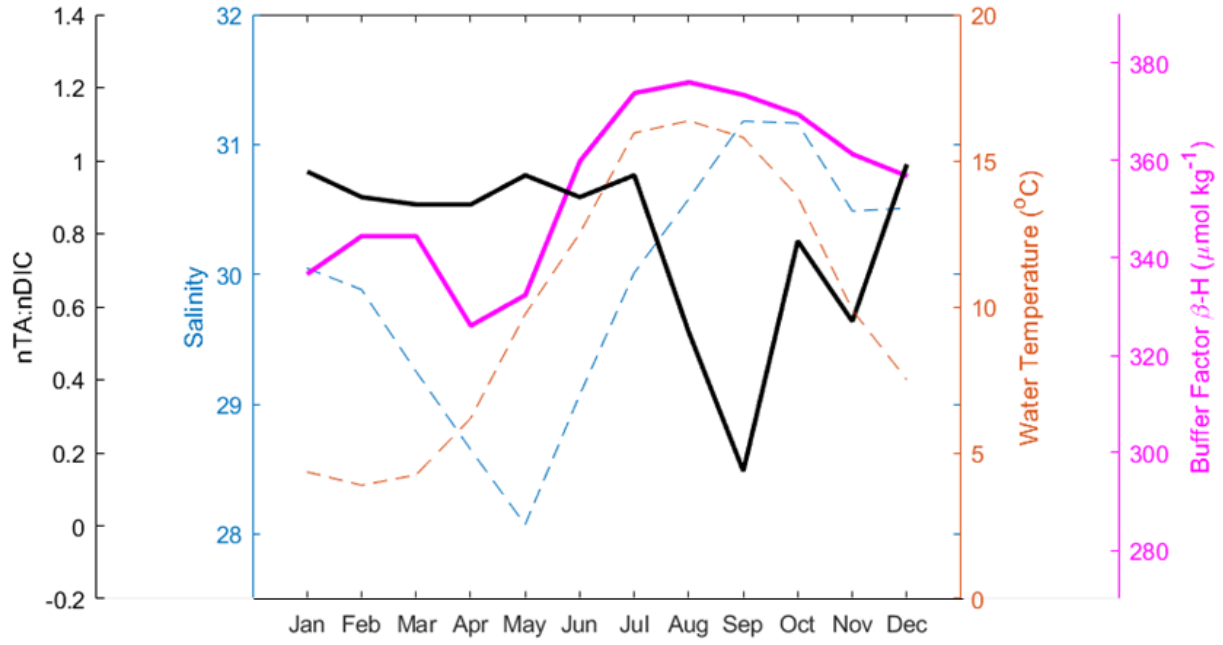

Figure 2.7: Monthly climatological salinity (dashed blue line), water temperature (dashed red line), buffer factor β-H (solid magenta line), and nTA:nDIC slope (solid black line) at the Coastal Marine Lab, calculated using data from 2016 through 2019.

Examination of TA:DIC changes have been used to estimate the prevalence of biogeochemical processes, however it is worthwhile to consider how river-ocean mixing might also affect the TA:DIC signature. Hunt et al. (2011a) presented a limited dataset of TA and DIC from three Great Bay rivers, which exhibited a mean TA:DIC of 0.78 (±0.11, n=12). If this ratio represents the predominant TA:DIC signature of river water entering Great Bay, then comparison to the low tide nTA:nDIC slope discussed above (0.92±0.016) would indicate substantial biogeochemical transformation between the river mouths and CML. Processes which would raise the nTA:nDIC slope above 0.78 would include SR, CD/P and iron reduction. Hunt et al. (2011b) presented a more extensive timeseries of data from one Great Bay river: the Oyster River, which was among the three Great Bay rivers sampled in Hunt et al. (2011a). These Oyster River data exhibited a mean TA:DIC of 1.02 (±0.14, n=41), a value substantially higher than both that from Hunt et al. (2011a, 0.78) and from the low and high tide data (0.92 and 0.84, respectively) discussed above. Thus TA:DIC data from Great Bay rivers encompass the TA:DIC values seen at both high and low tides at CML. However, a simple endmember mixing calculation determined that variability in river TA:DIC probably has little effect on the nTA:nDIC slope at CML, and that other processes must be present in order to produce the observed nTA:nDIC slopes.

It is important to consider that while nTA:nDIC slopes can be informative, they should also be interpreted together with TA and DIC addition or removal processes. For example, a nTA:nDIC slope of -0.16 could indicate aerobic respiration, as TA is consumed and DIC is produced. The same slope, however, can equally indicate primary production, as TA is produced and DIC is consumed. This is also true of carbonate

dissolution and precipitation. The above discussion focuses on nTA:nDIC slopes, which indicate that SR may have the strongest effect on relative changes in DIC and TA, with some possible influence of DN and seasonal expression of AR/PP. The overall TA mixing line appears mostly conservative, with perhaps a small TA removal (Figure 2.4), and indistinguishable between high tide and low tide (Figure 2.5). The DIC mixing line appears to indicate that DIC at CML is lower than that predicted by mixing with local rivers. Air-sea flux is one obvious explanation for the lower DIC, as CO_2 is removed from estuary water by degassing (Hunt et al. 2011a), a process which leaves TA unchanged. The biogeochemical processes that remove DIC are primary production and carbonate precipitation, but these processes produce changes in TA as well and this is not apparent in the data.

2.4.6 Contributions of mixing and temperature to buffering and pH

A simple set of calculations were performed to examine the relative influence of TA and DIC mixing and seasonal temperature changes on β-H and pH. Each parameter was calculated using CO2SYS, with TA and DIC inputs determined from the dataset-wide relationships with salinity (Figure 2.4). The mixing influence was determined using a constant water temperature of 10°C, monthly mean salinity (Table 2.2), and conservatively mixed TA and DIC (Figure 2.4). The temperature influence was determined using mean monthly temperature (Table 2.2) and a dataset-wide mean salinity of 29.9, TA of 2048 μmol kg^{-1}, and DIC of 1931 μmol kg^{-1}. Application of the

monthly mixing and temperature effects to mean β-H (352 μmol kg^{-1}) and pH (7.96) produced results matching the mean observed values within one standard deviation (Figure 2.8), indicating that mixing and temperature together account for much of the annual variability in β-H and pH at this site. Individually, the mean mixing effect was about three times stronger than the mean effect of in-situ temperature change for β-H (9.4 and 2.4 μmol kg^{-1}, respectively), while the effect of in-situ temperature change was nearly an order of magnitude stronger than the mixing effect for pH (0.06 and 0.007, respectively).

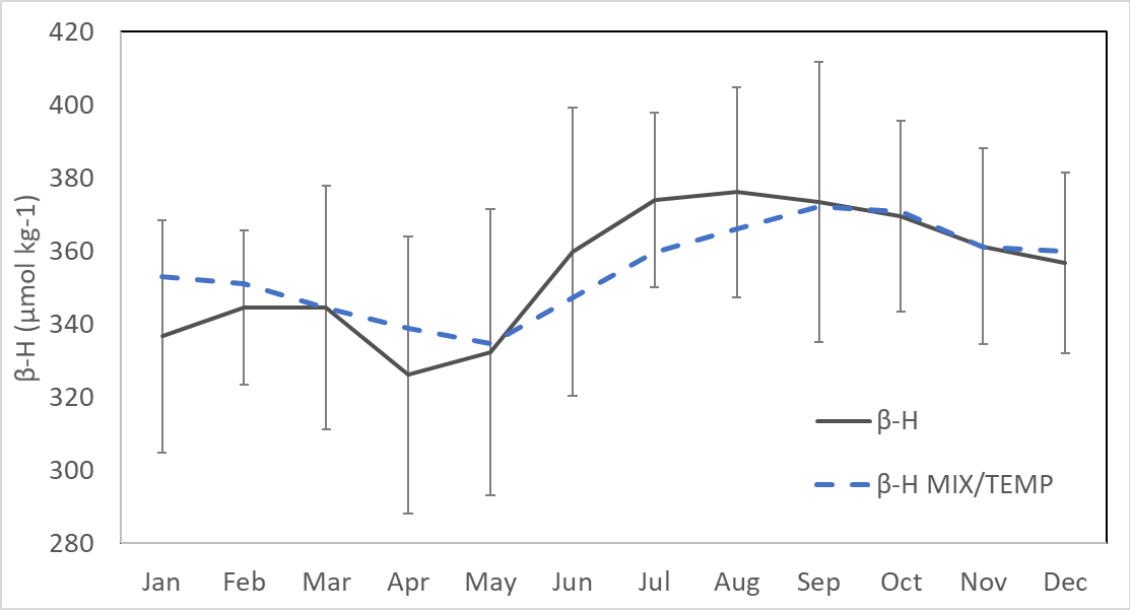

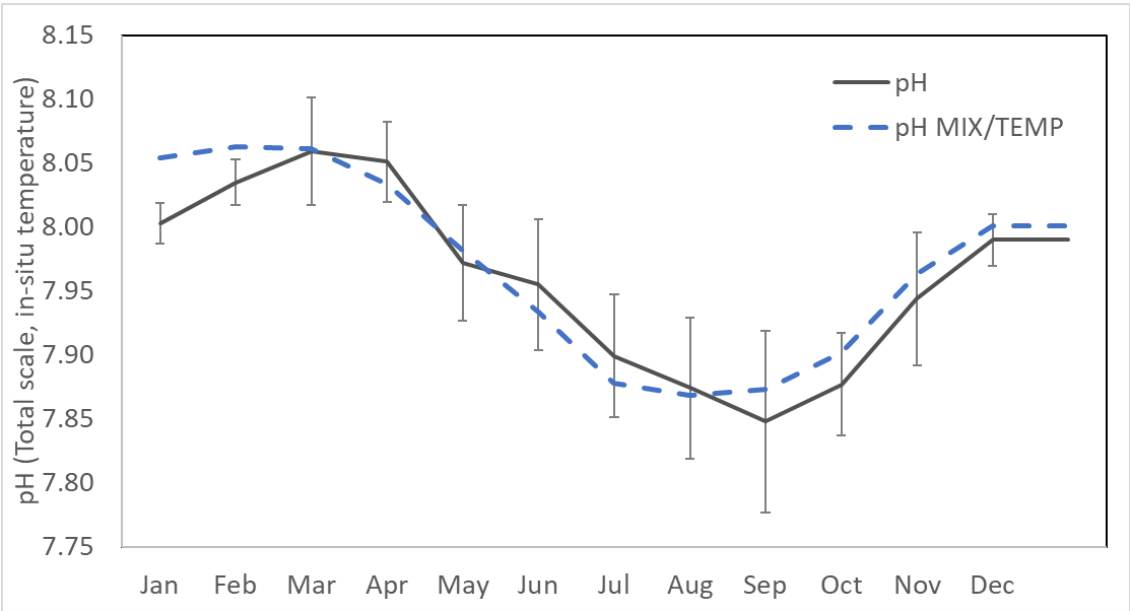

Figure 2.8: Observed monthly mean buffer factor β-H (top panel) and pH (bottom panel), indicated by the solid grey line. Errorbars indicate plus and minus one standard deviation of monthly mean β-H or pH. Theoretical β-H ("β-H MIX/TEMP") and pH("pH MIX/TEMP") due to endmember mixing and temperature changes, calculated from whole-dataset salinity-TA and salinity-DIC regressions, mean monthly salinity, and mean monthly temperature, are shown as dashed blue lines.

2.4.7 Relative influences of mixing and NEM on TA and DIC

Both mixing and NEM contributed to changes in TA, DIC, pH and β-H. These contributions appeared to shift seasonally, with mixing processes (and temperature) controlling changes for much of the year as shown in Figure 2.8, but metabolic process signatures were also evident in the late summer and fall (Figure 2.7). Results from a mechanistic model (Figure 2.9) help explain the apparent contradiction that β-H was highest in late summer and fall while this period also showed the largest change in nTA:nDIC that implied enhanced metabolic activity. We note that limited paired TA and pCO_2 data were available for the month of April in one year (n=29 in 2017), and these data were often not collected consecutively, producing unrealistically large, negative average monthly values of $\Delta[DIC]_{Mixing}$ and $\Delta[TA]_{Mixing}$ (-15.5 and -16.8 μmol kg^{-1}, respectively) which have been excluded from the following discussion. More complete data collection in April would likely result in seasonally-appropriate values of $\Delta[DIC]_{Mixing}$ and $\Delta[TA]_{Mixing}$. Overall, the model showed that mixing was the dominant control on changes in DIC and TA in winter and spring, a model result that is mostly driven by the higher degree of salinity variability (Figure 2.2, Table 2.2). By June the salinity became much less variable, and NEM overtook mixing as the more significant control. Air-sea flux, which only influences changes in DIC, also increased in importance through the summer, becoming the largest factor influencing DIC in the months of August and October. Interestingly, the model showed that late summer and fall represented a period of diminished NEM influence on DIC relative to the spring and early summer, but

this decrease in NEM was smaller than the decrease in mixing. The decreased mixing influence was due to less freshwater entering the estuary, resulting in saltier conditions at CML and relatively high salinities at both low and high tides, with proportionally higher DIC and TA. This then led to a more strongly buffered system despite the relatively strong influence of NEM. It is worth noting that some metabolic activity may be reflected in the seasonal changes in the ocean mixing endmember (Appendix B.2), and thus some of the mixing contribution at CML may instead be reflective of remote coastal ocean NEM. Whereas some studies have indicated that metabolic processes may pose a significant acidification risk in estuaries (Van Dam and Wang 2019, Cai et al. 2017), others have indicated that well-mixed estuaries may actually be buffered by increased NEM (Nixon et al. 2015). These results suggest that NEM at CML represents a smaller acidification risk than changes to river inputs (Salisbury et al. 2008) or acidification controlled by the coastal ocean. We emphasize here that these findings from CML, located at the mouth of the estuary, may not apply to conditions in Great Bay itself. Oxygen and pH monitoring data at CML and in central Great Bay surface waters do not show especially low oxygen or pH levels (PREP 2018, NERR 2021). However, the same oxygen and pH levels in tidal rivers supplying Great Bay (the Oyster, Lamprey and Squamscott rivers, Figure 2.1) can be much lower, with frequent evidence of hypoxia and low pH which may be promoted by NEP (PREP 2018, NERR 2021). While efforts to mitigate OCA by reducing nutrient inputs to lower overall NEM may be beneficial in Great Bay, they may have a lesser effect at CML, where AR appears to be a smaller contributor to NEM than SR, except in the fall when estuary buffering is already high (Figure 2.7).

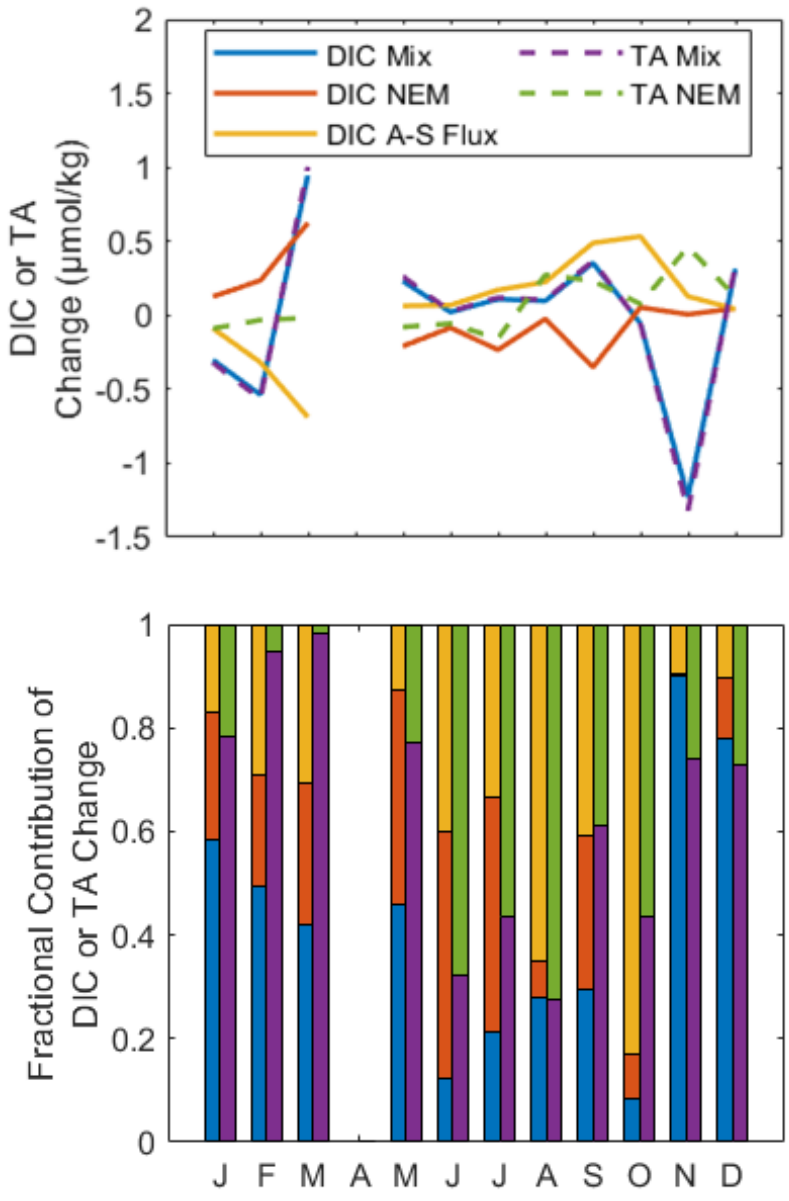

Figure 2.9: Modeled, monthly mean changes in DIC and TA due to mixing, metabolic and air-sea flux processes (top panel) and relative contributions of these processes to the total monthly DIC or TA change (bottom panel). Values shown in the top panel are the monthly mean values of DIC and TA changes over each hourly time step. The colors of lines shown in the legend of the top panel correspond to the bar colors of the bottom panel. Note that the DIC Mix and TA Mix lines in the top panel virtually overlie one another, and that results from April are excluded due to low data availability as discussed in the text.

2.5 Conclusions

This study presents evidence that CML, at the outlet of Great Bay, is a site of dynamic mixing, and this mixing influences estuary buffering capacity and acidification potential. Biogeochemical processes such as primary productivity and aerobic respiration may contribute to annual changes in pH, pCO_2, DIC, and β-H but the signatures of these processes are difficult to discern within the strong mixing and temperature signals. The annual period when biogeochemical processes have the strongest influence on changes in TA and DIC is also the period when the estuary is most highly buffered by an abundance of high salinity water. Future work could include estuary sampling transects from CML through Great Bay, with concurrent river endmember sampling. This would provide a snapshot view of TA and DIC addition relative to conservative mixing along the salinity gradient over a short time period and may identify areas upstream of CML where biogeochemical process signatures are discernible beyond physical influences. The addition of sampling for nitrate and ammonia at CML and upstream in Great Bay, particularly during winter, spring and early summer, would help constrain the possible influence of nitrification and denitrification on TA and DIC. These next steps would produce findings useful to policy makers and coastal managers who will need to decide which processes may be affected by regulation in order to better monitor and potentially ameliorate OCA.

CHAPTER 3: ORGANIC ALKALINITY DISTRIBUTIONS AND CHARACTERISTICS IN TWO GULF OF MAINE ESTUARIES

3.1 Introduction

Estuaries are the dynamic connection between terrestrial and oceanic aquatic systems, and the sites of some of the heaviest population densities in the world (Nixon 1995). Estuaries also provide important ecosystem services such as nursery and fishery habitats, filtering and detoxification, and flooding and storm event mitigation (Barbier et al. 2011). However, estuaries are threatened by changing atmospheric conditions (nitrogen deposition, carbon dioxide enrichment) oceanic conditions (ocean acidification, sea level rise, warming, frequency and intensity of storms), and terrestrially-derived impacts (eutrophication, organic matter fluxes, increased runoff).

The overall cumulative impacts of these changes on estuaries are unclear. On one hand, estuaries are commonly heterotrophic, high CO_2 environments that are more susceptible to acidification than adjacent ocean waters (Cai et al. 2011). The primary sources of acid buffering in ocean water have long been known to be the dissolved carbonate (CO_3^{2-}) and bicarbonate (HCO_3^-) ions (Park 1960), whose concentrations are commonly lower in estuaries. The carbonate/bicarbonate buffer regulates pH and the partial pressure of carbon dioxide (pCO_2) by the equilibria:

$$CO_2 + H_2O \leftrightarrow H_2CO_3 \leftrightarrow H^+ + HCO_3^- \leftrightarrow 2H^+ + CO_3^{2-} \quad (3.1)$$

While the CO_3^{2-} and HCO_3^- ions are the primary contributors to total alkalinity (TA) and pH buffering, other charged species can make significant contributions as well. Organic alkalinity (OrgAlk) has been identified as an important contributor to TA in riverine and low salinity coastal environments (Waldbusser and Salisbury 2014) including Gulf of Maine rivers (Hunt et al. 2011), the Kennebec estuary (ME, USA, Hunt et al. 2013), intertidal salt marshes (Song et al. 2020), some Southeastern U.S. estuaries (Cai et al. 1998), Baltic Sea estuary waters (Kulinski et al. 2014), Gulf of Mexico estuaries and coastal waters (Yang et al. 2015), and Korean coastal waters (Ko et al. 2016). The term organic alkalinity refers to the contributions of the conjugate bases of weak organic acids to total alkalinity- a contribution that depends on the total concentrations of the conjugate bases, their dissociation constants (pKs), and the pH of the water containing them. Thus, the contributions of a particular organic acid to total alkalinity may be quite different in an acidic estuary than in a well-buffered system; similarly, different forms of organic acid may have quite different contributions to alkalinity at the same pH. Ultimately, it is clear that the relative organic alkalinity concentrations are pH dependent. While a potentially important alkalinity component, the overall sources and roles of organic acids in driving physio-chemical reactions within estuaries remain unclear. Without a better understanding of the interplay between organic acids and inorganic alkalinity in estuaries and their coastal plumes, the potential of estuaries to respond to acidification threats from both land and sea cannot be determined.

Examinations of the aquatic carbonate system can employ measurements of TA, pH, dissolved inorganic carbon (DIC), and the partial pressure of carbon dioxide (pCO_2). Measurements of two of these parameters, together with the appropriate acid

dissociation constants (pK_a) are frequently used to calculate the other parameters in lakes (Cole et al. 1994, McDonald et al. 2013), rivers (Butman et al. 2011, Raymond et al. 2013), estuaries (Borges 2005) and ocean waters (Park et al. 1960). Software packages such as CO2SYS (Lewis and Wallace 1998) and SeaCARB (Lavigne et al. 2011) are available across a wide range of computing platforms to automate these calculations. However, if TA is used as one of the inputs for these calculations, and OrgAlk is present in significant quantities, then derived results will be inaccurate (systematically biased). For example, if TA and pH are used to derive pCO_2 and DIC, and OrgAlk is significant, DIC and pCO_2 will both be overestimated, sometimes by a large factor (Abril et al. 2014). A number of recent estimates of CO_2 release from U.S. lakes (McDonald et al. 2013), U.S. rivers (Butman et al. 2011), and global rivers (Raymond et al. 2013) derive CO_2 flux estimates from the combination of TA and pH measurements; consequently, our understanding of global terrestrial and estuary CO_2 fluxes are subject to large potential uncertainties due to the undetermined effects of OrgAlk.

In addition to the quantity of OrgAlk present in a system, the acid-base characteristics of that OrgAlk are also important. While the pK_a values of carbonate and bicarbonate are well characterized and predictable from salinity, temperature and pressure, those of OrgAlk are not. The few studies which have characterized the pK_a of estuary OrgAlk have yielded a continuum of values from 4.5-7.5, and indicate that the acid-base chemistry associated with OrgAlk is complex (Cai et al. 1998, Kulinski et al. 2014, Yang et al. 2015, Ko et al. 2016). If the pK_a's of OrgAlk are sufficiently low, then organic bases will remain dissociated at oceanic and estuary pH levels, and will not

bond with H^+ ions, even at the lower pH levels predicted under ocean acidification scenarios. Thus, even at high concentrations of organics, the effect of OrgAlk on pH may be small, contributing weakly as a buffer against ocean acidification.

In studies of seawater (Dickson 1981) and freshwater (Stumm and Morgan 1995, Drever 1997), total alkalinity (TA) is discussed as the sum of anions in solution which can be neutralized by strong acid. In both aquatic environments, the pH 'equivalence point' has been operationally set at pH 4.5. This definition has served the aquatic sciences well, as the majority of TA is typically thought to be comprised of carbonate and bicarbonate species, which will be about 96% protonated to carbonic acid at pH 4.5. Similarly, other significant species such as borate and silicate will also be fully protonated at or below pH 4.5, while the first dissociation constant of phosphoric acid (H_3PO_4) of about 2.1 is low enough to exclude protonation at the 4.5 equivalence point. To ensure complete carbonic acid formation and increase hydrogen ion concentration signals, current seawater analysis methods call for titration at lower pH working range (3.5-3.0, Dickson et al. 2007), although with accurate pH measurements the TA can also theoretically be measured accurately at virtually any pH, with results consistent with those at pH 4.5, or 3.0, and also consistent with the formal definition of TA (Liu et al. 2012), provided that no species are present in solution that have a dissociation constant similar to the equivalence point. This definition, from Dickson (1981) is presented in Equation 3.2, where any species with an acid dissociation constant (pK_a) greater than 4.5 at zero ionic strength is defined as a base, or proton acceptor, while any species with a pK_a less than 4.5 defined as an acid.

$$TA = [HCO_3^-] + 2[CO_3^{-2}] + [B(OH)_4^-] + [OH^-] + [HPO_4^{-2}] + 2[PO_4^{-3}] + [H_3SiO_4^-] + 2[H_2SiO_4^{-2}] + [HS^-] + 2[S^{-2}] + [NH_3^0] + [OrgAlk^-] - [H^+] - [HSO_4^-] - [HF] - [H_3PO_4] \quad (3.2)$$

However, all definitions of TA have included a catch-all term of unspecified organic anions (OrgAlk in Equation 3.2). These organics will contribute to TA in a way consistent with Equation 3.2, provided that they become fully protonated at or above pH 4.5 (i.e., have a pK_a substantially greater than 4.5). However, there is increasing evidence that some naturally occurring anions are not fully protonated below pH 4.5 (Ulfsbo et al. 2015, Sharp and Byrne 2020).

In this study we sampled two Gulf of Maine estuary systems: the St. John Estuary in Maine USA, and the St. John estuary in New Brunswick Canada over four spring and fall transits, collected samples along the estuary salinity gradient and at the river endmember, and analyzed samples for several parameters including OrgAlk measured according to two different methods. We then compare these measures of OrgAlk and estimated values of estuary organic matter pK_a.

3.2 Materials and Methods

3.2.1 Study Sites

Two river-estuary systems were selected for this study, based on previous work which documented contrasting levels of DOC, TA, OrgAlk and pH measured at the river endmembers (Hunt et al. 2011). The Pleasant River drains an approximately 160 km^2

watershed forested in deciduous trees before emptying into Pleasant Bay, but the watershed is also characterized by substantial regions of heath predominantly used to cultivate wild blueberries. Pleasant River water is known to be rich in tannins (a synonym for humic acids), and the darkly colored water empties into the marsh-fringed estuary at the town of Columbia Falls, ME (Keller 2020). The tidal portion below the dam at Columbia Falls Maine is identified on NOAA chart 13324 as the “Pleasant River”; however, for this work we will refer to the Pleasant River as the freshwater portion upstream of the dam, and we will refer to the tidal portion between the dam and Pleasant Bay as the St. John Estuary. The St. John River drains a much larger watershed, approximately 55,000 km^2, which encompasses areas of Maine (USA) and New Brunswick (Canada). The river empties into the Bay of Fundy at St. John, New Brunswick, although vigorous tidal mixing occurs above and below this location. The watershed is mostly forested, with occasional agricultural areas. Soils are loamy and well-drained, overlying a mixture of limestone and sandstone bedrock.

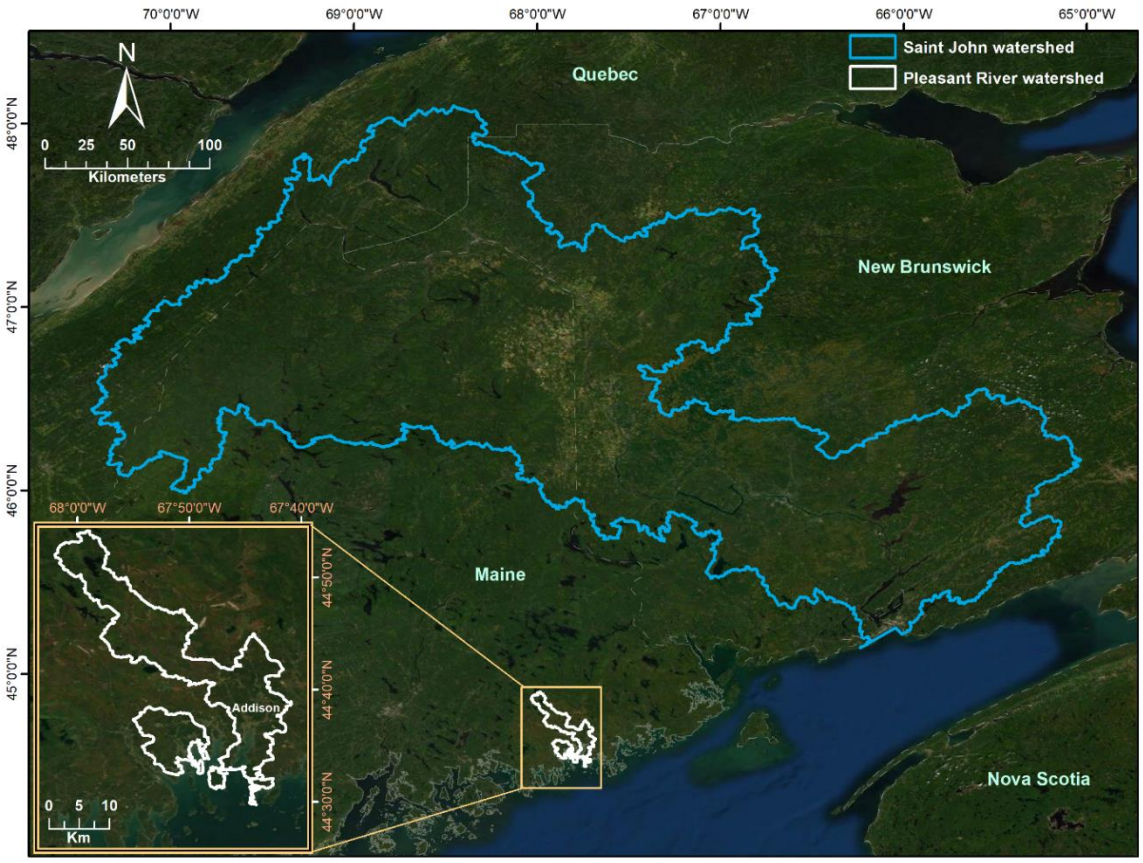

Figure 3.1: The Pleasant (white) and St. John (blue) watersheds. The Pleasant River watershed is located in Maine USA; the St. John River watershed includes areas of Maine USA and New Brunswick Canada. The Bay of Fundy, the northern extension of the Gulf of Maine, is shown between Maine and Nova Scotia. Estuary sampling locations were located at the outlets of the outlined watersheds.

3.2.2 Sample Collection

Estuary samples were collected during single-day surveys on small vessels in each system. Four surveys were conducted of both the Pleasant and St. John estuaries, in May and October 2018, and again in May and October 2019. Estuary water was continuously pumped to an underway measurement system, which recorded location,

salinity, water temperature, and the partial pressure of carbon dioxide (pCO_2). A detailed description of this underway system can be found in Hunt et al. (2013). Surveys were started on the incoming tide and lasted through high tide and into the ebb tide. At intervals determined from the underway salinity, surface water was captured for discrete sample collection. During the October 2017 and May 2018 surveys a Niskin bottle was lowered overboard by hand; during the later surveys, a 10-liter high-density polyethylene (HDPE) carboy was rinsed and filled from the outflow of the underway system, then tightly capped until samples were drawn from a spout at the bottom of the carboy. River endmember samples were collected from above the most downstream dam on each river. For the Pleasant, this dam formed a physical tidal barrier, and the transition from river to estuary was immediate. For the St. John the closest site was in Fredericton New Brunswick, a location over 120 km from the estuary mouth along the river's course. For both endmember sites, a plastic bucket was lowered from the center of a bridge over the river, rinsed three times with river water, and samples were collected as described above. The temperature and conductivity of samples were measured directly from the bucket with a handheld meter (YSI, Yellow Springs, Ohio).

Water from the Niskin or carboy was transferred without bubbling into individual, previously-flushed glass BOD bottles: 500 mL for alkalinity and pH analyses, and 300 mL for inorganic carbon (C_T) analysis. All bottles had greased stoppers and positive closure mechanisms, were filled to leave less than 1% headspace in the bottle and all samples were preserved with saturated mercuric chloride solution. Samples for silicate and phosphate analysis were filtered using a plastic syringe and 0.2 µm cartridge filter into acid-washed and previously-rinsed 50 mL HDPE vials and preserved with

chloroform. Samples for DOC were filtered as was done for the nutrients into acid-washed and previously-rinsed 30 mL HDPE bottles. All samples were immediately placed on ice. Alkalinity, pH, and DIC samples were refrigerated until analysis; nutrient and DOC samples were frozen until analysis.

3.2.3 Alkalinity Titrations

Total alkalinity and organic alkalinity titrations were conducted using a custom-build apparatus similar to that presented in Cai et al. (1998). This system performed several successive titrations upon the same water sample, in order to measure (in order) the TA (Alk_{Gran1}), the carbonate-free alkalinity according to the Gran titration approach (Alk_{Gran2}), and the carbonate-free alkalinity at pH 4.5 according to an endpoint approach ($Alk_{4.5}$, Figure 3.2).

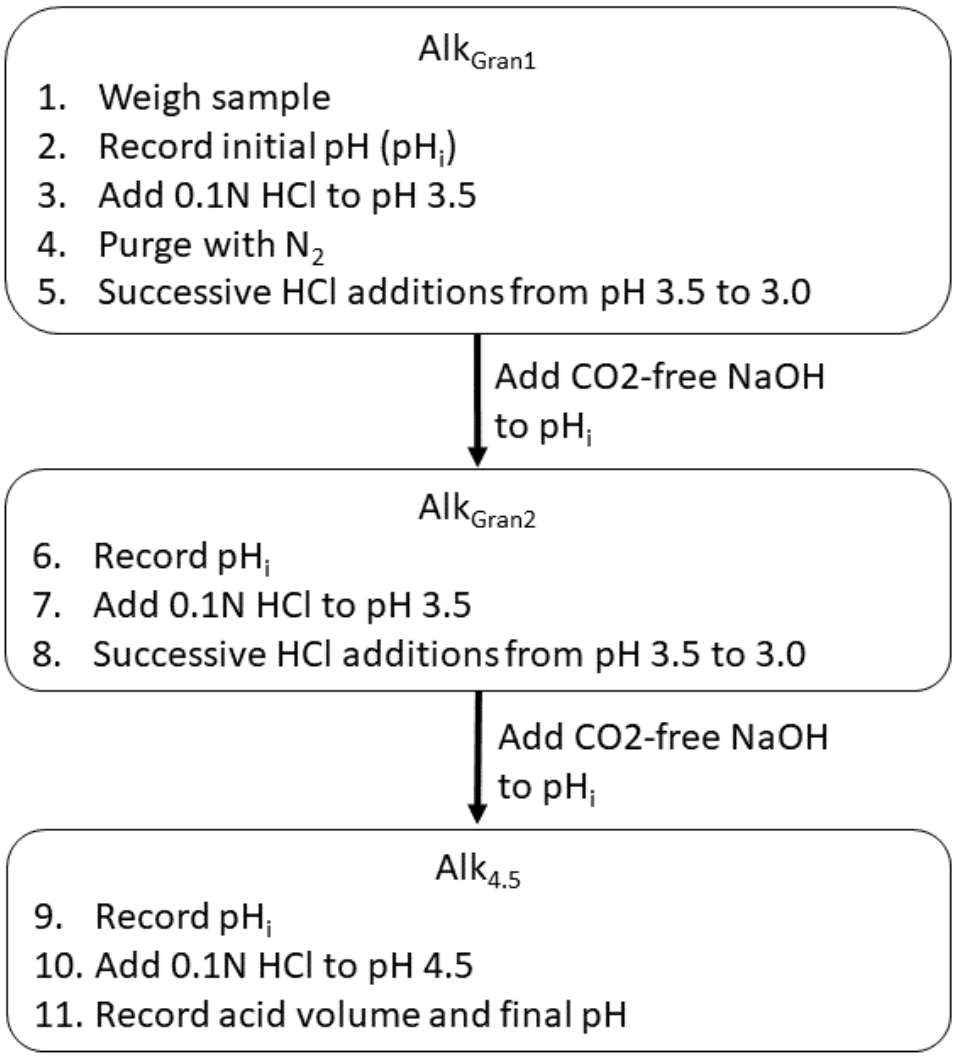

Figure 3.2: The steps of the Alk_{Gran1}-Alk_{Gran2}-$Alk_{4.5}$ titration approach. All steps after number four were carried out under a nitrogen atmosphere.

An empty, clean titration vessel with magnetic stir bar were first weighed (to the nearest 0.001 g), then sample was poured into the vessel and the mass of sample determined by difference. A cap with openings for the pH electrode, ultrapure nitrogen (N_2) gas line, hydrochloric acid titrant (HCl) line, and sodium hydroxide (NaOH) line was then screwed onto the titration vessel. The vessel was then placed into a water-

jacketed beaker, maintained at 25°C by a circulating water bath. This beaker rested on a magnetic stir plate. The pH electrode and HCl dosing tube were inserted through the titration vessel cap and stirring started. The pH electrode used in this work was a Metrohm EcoTrode Plus (Metrohm USA, Riverview FL) connected to a Thermo Scientific Orion Star^{TM} A211 pH meter (Thermo Fisher Scientific, Waltham MA USA). The experimental response slope of this electrode was periodically verified by comparison to a series of spectrophotometric seawater pH measurements using purified meta-cresol purple indicator (mCP, Liu et al. 2011) according to the procedure of Easley and Byrne (2012). Details of the electrode slope calibration are included in Appendix C. As the electrode intercept potential (E_0) has been shown to be salinity dependent (Easley and Byrne 2012, Martell-Bonet and Byrne 2020), a unique E_0 was calculated for each sample based on the Alk_{Gran1} titration data. As the electrode was calibrated against spectrophotometric pH measurements on the Total pH scale, all pH measurements presented in this work are also on the Total scale. Once the electrode was inserted into the sample and stirring started, an initial pH reading was taken (pH_i).

HCl titrant was dispensed by a Dosimat 876 digital burette (Metrohm USA, Riverview FL), controlled by a custom-designed software program. The HCl used was certified titrant obtained from Dr. A. Dickson (Batch A18, 0.100661±0.000006 mol kg^{-1}). For a typical Gran titration, as described in Standard Operating Procedure 3B (Dickson et al. 2007), the software program added HCl titrant to a pH of about 3.5, before prompting the operator to insert the ultrapure nitrogen gas (N_2) tube used to purge the acidified sample and maintain a CO_2-free environment for subsequent titrations. The sample was bubbled for five minutes to purge any remaining CO_2, and the N_2 tube

remained in the sample for the remainder of the measurement, as well as during subsequent measurements of the samples. After purging, the instrument then added subsequent doses of HCl titrant (n=8 to 10) to a pH near 3.0, which produced the HCl/pH pairs needed for the Gran alkalinity calculation over the 3.5 to 3.0 pH range. For each sample the initial Gran titration yielded a measurement of TA (Alk_{Gran1}) and E_0 (the electrode potential at pH 0). E_0 has been shown to be electrode-and-salinity dependent (Easley and Byrne 2012, Martell-Bonet and Byrne 2020), so the experimentally-determined E_0 was paired with the spectrophotometrically-verified electrode slope to calculate pH for each sample titration point.

After the initial Gran titration, CO_2-free NaOH (see Supplementary Material) was added to the acidified sample using a Metrohm Dosimat 665 in order to raise the pH_T back to pH_{Ti}, resulting in a sample at a pH_T nearly identical to the untitrated sample but containing no CO_2 species. This CO_2-free sample was then titrated according to two methods (Figure 3.2). For Alk_{Gran2} the Gran titration approach was repeated on the CO_2-free sample to pH_T 3.0, as described above. NaOH was again added to return the sample to pH_{Ti}. Finally, an endpoint titration to pH_T 4.5 was performed on the CO_2-free sample, yielding $Alk_{4.5}$.

3.2.4 Analytical Methods

Discrete sample salinity was measured with a Guildline Portasal salinometer (Guildline, Smiths Falls Canada). The pH_T of samples above 7.0 was measured

spectrophotometrically as described above, using 10cm round glass cells and an Agilent Technologies Cary 8454 UV-Vis. The same instrument was used to verify the electrode response slope. For samples of pH_T less than 7.0, and therefore outside the working range of mCP, the initial mV reading and E_0 value determined from the Alk_{Gran1} titration were used to calculate the pH of the untitrated sample. All pH_T measurements were performed on samples preserved with mercuric chloride. DOC was measured using a Shimadzu high temperature catalytic oxidation analyzer with chemiluminescent detection, with an uncertainty of 1.5 µmol kg^{-1}. Nutrients including phosphate and silicate were analyzed using a SmartChem automated analyzer (Westco Scientific) according to standard colorimetric methods, resulting in uncertainties of 0.8 µmol kg^{-1} and 0.25 µmol kg^{-1}, respectively (Strickland and Parsons 1972). C_T was measured by acidifying each sample using a custom-built gas extraction system, with the evolved CO_2 passed through a Picarro G5131-I cavity ringdown spectrometer (Picarro, Santa Clara CA).

3.2.5 Calculation of Alk_{Gran1}, Alk_{Gran2}, and $Alk_{4.5}$

Alk_{Gran1} and Alk_{Gran2} were calculated according to the Gran function (Gran 1952) with a nonlinear least squares correction for the presence of sulfate and fluoride ions (Dickson et al. 2007). Alk_{Gran2} and $Alk_{4.5}$ were measured sequentially after Alk_{Gran1} on the same aliquots of water; the Alk_{Gran1} procedure removed all inorganic carbon, and continuous purging of the titration vessel prevented re-dissolution of CO_2. At an

endpoint of 4.5, $Alk_{4.5}$ was simply determined as the difference between the concentration of added H^+ ions from the HCl titrant and the measured H^+ ion concentration (of $10^{-4.5}$, or about 3.2×10^{-5} M at pH_T 4.5):

$$Alk_{4.5} = \frac{m_A c_A}{m_0} - \frac{[H^+](m_0+m_A)}{m_0} \quad (3.3)$$

where m_A is the mass of added HCl titrant, c_A is the concentration of HCl titrant, m_0 is the initial sample mass, and [H+] is the hydrogen ion concentration determined from the endpoint pH measurement on the Total pH scale. The pH_T was calculated from the observed E_0 determined during the Alk_{Gran1} measurement for each sample:

$$pH = \frac{E-E_0}{RT \cdot \frac{\ln(10)}{F}} \quad (3.4)$$

where E is the electrode potential measured at the titration endpoint (in volts), E0 is the electrode intercept potential, R is the molar gas constant, T is the titration temperature (in Kelvin), and F is the Faraday constant.

3.2.6 Calculation of $OrgAlk_{Gran2}$ and $OrgAlk_{4.5}$

As Alk_{Gran2} and $Alk_{4.5}$ titrations were performed on CO_2-free solutions, their values represented the sum contribution of minor alkalinity components (A_x):

$$A_x = [OH^-] + 2[PO_4^{3-}] + [HPO_4^{2-}] + [SiO(OH)_3^-] + [B(OH)_4^-] + [OrgAlk_x{}^-] - [H^+]_T \quad (3.5)$$

where Ax is either Alk_{Gran2} or $Alk_{4.5}$ and $[H^+]_T$ is the total hydrogen ion concentration (including hydrogen sulfate, HSO_4^-). $OrgAlk_x$ represents the contribution of organic

species to Alk_{Gran2} or $Alk_{4.5}$, and was calculated as the residual after all other alkalinity species were taken into account. Phosphate and silicate concentrations were either taken from the reported CRM documentation or measured using a SmartChem automated analyzer (Westco Scientific) by standard colorimetric methods and have uncertainties of 0.0008 µmol kg-1 and 0.25 µmol kg-1, respectively (Strickland and Parsons 1972).

3.2.7 Estuary OrgAlk and K_a parameterizations

Cai et al. (1998) presented two methods for the estimation of organic function group concentration and dissociation constant determination. The first involved a stepwise titration of previously-acidified sample with CO_2-free NaOH, from pH 3 to 10, and nonlinear least squares fitting of the resulting titration curve. We attempted to employ a modified version of this model, using CO_2-free NaOH to return the acidified sample to a pH of 8.5, then titrating in a stepwise manner with the same HCl titrant used in the original titration. However, we were unable to consistently estimate pK_a values or OrgAlk concentrations with this method, even when titrating a simple NaCl solution. The reasons for this are not clear, but may include interferences from silicate inputs from glassware not present in the lower-pH $OrgAlk_{Gran2}$ or $OrgAlk_{4.5}$ titrations, compounding uncertainties related to the repeated dispensing of very small titrant volumes from the digital burette, or hysteresis in acid-base behavior during additions of NaOH or HCl, as documented by Paxéus and Wedborg (1985). Our test titrations

resulted in unreasonably large alkalinities of test solutions, which did not match the alkalinities determined via Alk_{Gran1}, Alk_{Gran2} or $Alk_{4.5}$ approaches. Further development and refinement of this method is greatly needed.

As we were unable to reliably reproduce this first method with our samples, we used the second method (hereafter referred to as the "Cai Fit"), which takes advantage of the natural titration of organic material between the acid river and alkaline coastal ocean endmembers, and returns best-fit parameterizations of pKa and the XT charge group total concentrations at the river and ocean endmembers. This calculation uses inputs of OrgAlk concentration, pH_T, and salinity, assumes that changes in OrgAlk concentration are only determined by pH_T and mixing, and also assumes that the total concentration of a single organic charge group (for example, X_T) is the sum of the protonated (HX) and ionic forms (X^-) and remains conservative during estuary mixing (i.e., $X_T = HX + X^-$):

$$OrgAlk = \left(1 - \frac{S_m}{S_{Ocean}}\right) \sum_j \frac{X_{Triver} K_X}{K_X + [H^+]_f} + \frac{S_m}{S_O} \sum_j \frac{X_{Tocean} K_X}{K_X + [H^+]_f} \qquad (3.6)$$

Equation 3.6 is from Cai et al. (1998), where OrgAlk is either $OrgAlk_{Gran2}$ or $OrgAlk_{4.5}$ concentration, measured as described above, S_m is the salinity of the estuary sample, S_{Ocean} is the coastal ocean endmember salinity, X_{Triver} is the total concentration of charge group X at the river endmember, K_X is the dissociation constant of charge group X, $[H+]_f$ is the free hydrogen ion concentration and X_{Tocean} is the total concentration of charge group X at the coastal ocean endmember. Using the Matlab® "lsqcurvefit" function (Mathworks, Natick MA) and OrgAlk, pH_T and salinity data from

each estuary survey, the Cai Fit returned the parameters X_{Triver}, X_{Tocean}, and K_X which best fit the observations.

3.2.8 Estuary DOC, K_{DOC} and f parameterizations

Kuliński et al. (2014) presented an empirical parameterization of organic alkalinity (Hereafter referred to as the "Kuliński Fit"), using inputs of organic alkalinity, DOC, and pH_T. This parameterization returns best-fit values of the bulk DOC dissociation constant (pK_{DOC}) and acidic fraction of DOC (f), according to:

$$OrgAlk = \frac{K_{DOC} * f * [DOC]}{[H^+]_T + K_{DOC}} \quad (3.7)$$

Where K_{DOC} is a bulk dissociation constant which reflects the fraction f of DOC that acts as a weak acid charge group, [DOC] is the total DOC concentration, and $[H+]_T$ is the hydrogen ion concentration calculated from pH measurements on the Total pH scale. As with the Cai Fit, we used the Matlab "lsqcurvefit" function (Mathworks, Natick MA), inputs of OrgAlk (both $OrgAlk_{Gran2}$ and $OrgAlk_{4.5}$), pH_T and DOC from each estuary survey to model the parameters of K_{DOC} and f that best fit the observed data.

3.3 Results

Conditions at the river or lowest-salinity endmember of each estuary varied widely (Table 3.1), and the conditions of each endmember offered a view of contrasting watershed inputs. The Pleasant River endmember was highly acidic and poorly

buffered, with a mean pH_T of 4.394 and mean Alk_{Gran1} of -39 µmol kg^{-1}. The concept of a negative alkalinity concentration may be counterintuitive, but simply relates to the deficit of proton donors relative to proton acceptors; as the equivalence point of total alkalinity is defined at pH 4.5 (Dickson 1981) a sample with a natural pH less than 4.5 may be expected to exhibit negative Alk_{Gran1}. A pH_T of 4.394 translates to a $[H^+]_T$ of 40 µmol kg^{-1}; as shown in Equation 3.5 the $[H^+]_T$ is treated as a negative quantity in the alkalinity calculation, and thus the negative Pleasant River Alk_{Gran1} is entirely due to the natural hydrogen ion concentration. The St. John River by contrast was more buffered, with a mean pH_T of 6.808 and mean Alk_{Gran1} of 650 µmol kg^{-1}. The mean Pleasant River endmember DOC was also double that of the St. John River, while the mean St. John River DIC was more than four times higher than that in the Pleasant River. The October surveys in both systems followed dry summers with low river discharge and coincided with the highest endmember pH_T and Alk_{Gran1}, DIC, and DOC concentrations.

Table 3.1: Endmember characteristics for the four surveys described in this study. Minimum and maximum values are shown above, with the mean and one standard deviation in parentheses below.

	Pleasant	St. John
Alk_{Gran1} (µmol kg^{-1})	(-92) - (-15) (-39±36)	463 - 858 (650±182)
pH_T	3.976 - 4.785 (4.394±0.333)	6.437 - 6.920 (6.808±0.356)
DIC (µmol kg^{-1})	123 - 211 (153±40)	337 - 978 (691±201)
DOC (µmol kg^{-1})	545 - 1944 (1238±720)	463 - 882 (612±185)
$OrgAlk_{Gran2}$ (µmol kg^{-1})	(-31) - (-12) (-25±8.9)	40 - 51 (43±5.6)
$OrgAlk_{4.5}$ (µmol kg^{-1})	n/a	24 - 33 (28±3.8)

Alk_{Gran1}, pH_T and DOC distributions with salinity in both the Pleasant and St. John estuaries reflected the mixing of the distinct river endmembers with the common Gulf of Maine higher-salinity endmember (Figure 3.3). Alk_{Gran1} and pH_T were consistently lower in the Pleasant Estuary than the St. John Estuary at the same salinity. Alk_{Gran1} in both estuaries appeared to reflect mostly conservative mixing across the salinity gradient, although at salinities less than 3 the Pleasant Alk_{Gran1} exhibited some nonlinear characteristics with non-conservative Alk_{Gran1} (Figure 3.3). While the slope and zero-salinity intercept of the Pleasant Estuary Alk_{Gran1} was consistent across the four surveys, the respective quantities in the St. John Estuary varied, with shallower slopes and higher zero-salinity intercepts in October than in May. Nonlinear distributions of pH_T with salinity are thermodynamically consistent, although the pH_T values below 6 in the Pleasant Estuary reflected a distinctly acidic system. Note that all pH_T values are reported as measured at 25°C in the laboratory. pH_T was higher by several tenths across the salinity range during October surveys in the St. John Estuary when compared to October surveys, especially at salinities lower than 15; the opposite was true in the Pleasant Estuary, when pH_T was somewhat higher in May than October, although the difference was not as large as in the St. John Estuary. This is explained by higher St. John Alk_{Gran1} in October relative to May at the same salinity, while DIC at the same salinity remained similar between May and October, resulting in more buffering and higher pH_T. The Pleasant Estuary pH_T results are explained by the opposite trend: TA remained consistent at the same salinity among May and October surveys, but DIC at the same salinity was higher in October, leading to less buffering and lower pH_T. In contrast to Alk_{Gran1} and pH_T, DOC was consistently higher in the Pleasant Estuary than

in the St John at a comparable salinity and season. While St. John DOC-salinity distributions were similar across the four surveys, with the possible exception of the October 2019 St. John survey, DOC concentrations across the salinity gradient in October were more than twice as high than in May in the St. Pleasant Estuary.

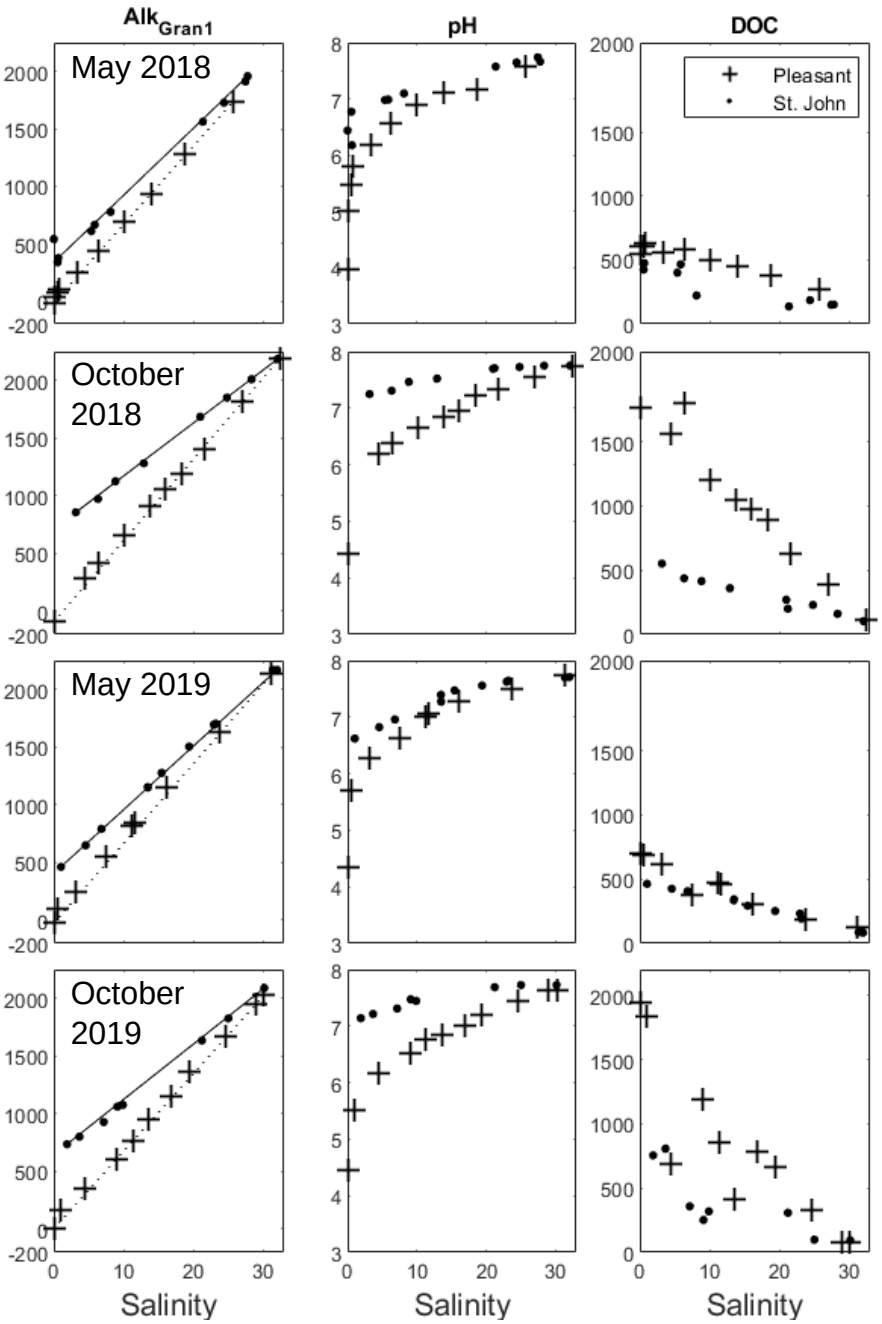

Figure 3.3: Distributions of Alk_{Gran1} (left panels, µmol kg^{-1}), pH_T (center panels, Total scale), and dissolved organic carbon (right panels, µmol kg^{-1}) against salinity in the Pleasant (circles) and St. John (crosses) estuaries. From top to bottom, data were collected in May 2018, October 2018, May 2019 and October 2019. Lines in the alkalinity plots connect the lowest- and highest-salinity data points, and do not represent a quantitative regression line.

3.3.1 OrgAlk Titration Validation Results

Since there are no standard solutions of organic alkalinity available, nor a standard methodology for the measurement of organic alkalinity, we assessed the titration procedure in two ways. We performed repeated measurements of the Alk_{Gran1} and $Alk_{4.5}$ of a 0.7M NaCl solution (see Appendix C), which could be reasonably expected to contain little to none of the phosphate, silicate, or boron *Ax* alkalinity components listed in Equation 3.5. These measurements in 0.7M NaCl showed that at most 1 µmol kg^{-1} of $Alk_{4.5}$ could be attributed to unknown alkalinity contributors, while no excess contribution to Alk_{Gran2} was observed; when measurement uncertainties are taken into account no measurable alkalinity was observed in either test.

We also repeatedly measured the Alk_{Gran1} and $Alk_{4.5}$ of certified reference material (CRM) obtained from Dr. A. Dickson (Batch 185, Dickson et al. 2003). The mean CRM Alk_{Gran1} was 2218.6 µmol kg^{-1}, representing a mean difference from the certified TA value of -2.1±5.0 µmol kg^{-1} (n=37) and indicating reasonable titration system performance. The mean A_X of previously titrated, CO_2-free CRM at the titration endpoint of 4.5 ($A_{X4.5}$) was 65.6±3.1 µmol kg^{-1}, a value which includes all the potential A_X contributors listed in Equation 3.5, the largest of which is expected to be from borate (A_B). To examine the potential contribution of $OrgAlk_{4.5}$ to $A_{X4.5}$ the contributions of phosphate and silica alkalinities were calculated from the total phosphate and silicate concentrations listed for CRM Batch 185 (0.42 and 3.0 µmol kg^{-1}, respectively). The boron concentration of CRM Batch 185 has not been determined; however two boron-to-salinity ratios are commonly employed to estimate seawater boron concentrations:

Uppström (1974, 0.1284 mg kg^{-1} $‰^{-1}$) and Lee et al. (2010, 0.1336 mg kg^{-1} $‰^{-1}$). Using these ratios to calculate total boron concentrations and A_B, then subtracting A_B and the phosphate, silicate and hydroxide ion alkalinities from $A_{X4.5}$ resulted in calculated CRM $OrgAlk_{4.5}$ values of 5.2±3.2 µmol kg^{-1} and 2.9±3.2 µmol kg^{-1}, respectively (n=37). To simplify the presentation of results we chose to use the mean of the Uppström and Lee et al. ratios to calculate boron concentration, A_B, and subsequent $OrgAlk_{Gran2}$ and $OrgAlk_{4.5}$, resulting in a mean CRM $OrgAlk_{4.5}$ of 4.0±3.2 µmol kg^{-1} (n=37), a value dependent on the actual final pH of each endpoint titration. A similar approach using the mean of the Uppström and Lee et al. ratios resulted in a mean CRM $OrgAlk_{Gran2}$ value of 12.0±2.8 µmol kg^{-1} (n=3).

3.3.2 Estuary OrgAlk

Organic alkalinity measured as $OrgAlk_{Gran2}$ and $OrgAlk_{4.5}$ was observed in both the Pleasant and St. John estuaries, including the lowest-salinity endmembers, in all four surveys (Figure 3.4, Table 3.1). As with Alk_{Gran1}, the Pleasant endmember $OrgAlk_{Gran2}$ was consistently negative, reflecting the low pH_T conditions of the Pleasant River. This low river pH did not permit the measurement of $OrgAlk_{4.5}$ at the river endmember, as the titration endpoint pH of 4.5 was higher than the river pH. The St. John low-salinity endmember had consistent $OrgAlk_{Gran2}$ and $OrgAlk_{4.5}$ concentrations, with mean values of 43±5.6 and 28±3.8 µmol kg^{-1}, respectively. Estuarine mixing rapidly changed the distributions of $OrgAlk_{Gran2}$ and $OrgAlk_{4.5}$ in the Pleasant Estuary, with increasing salinity coinciding with both increasing $OrgAlk_{Gran2}$ and $OrgAlk_{4.5}$ to a mid-estuary maximum and then decreasing towards the ocean endmember. This low-salinity

increase was particularly large in the Pleasant October surveys, when $OrgAlk_{Gran2}$ rose more than 100 µmol kg^{-1}. $OrgAlk_{Gran2}$ and $OrgAlk_{4.5}$ were typically higher in the Pleasant Estuary than in the St. John above a salinity of 3 in the October surveys, while concentrations were similar between the two systems during the May surveys. Maximum $OrgAlk_{Gran2}$ and $OrgAlk_{4.5}$ concentrations were typically found between salinities 1-11, with exceptions in the Pleasant Estuary in May 2018 where the maximum values were at higher salinities, and the St. John in October 2018 when the maximum $OrgAlk_{4.5}$ was found at the highest salinity sampled (32.10). This sample was collected outside the St. John Estuary while the other samples on this survey were collected inside the Estuary; this sample also was collected on the seaward side of a sharp gradient in salinity, which may indicate that it represented a distinct water mass from the Estuary samples. For these reasons this sample was held out of the pK_a and pK_{DOC} fitting analyses. $OrgAlk_{Gran2}$ concentrations were consistently higher than the respective $OrgAlk_{4.5}$ concentrations at low and middle estuary salinity, but the concentrations typically became comparable at salinities above 25.

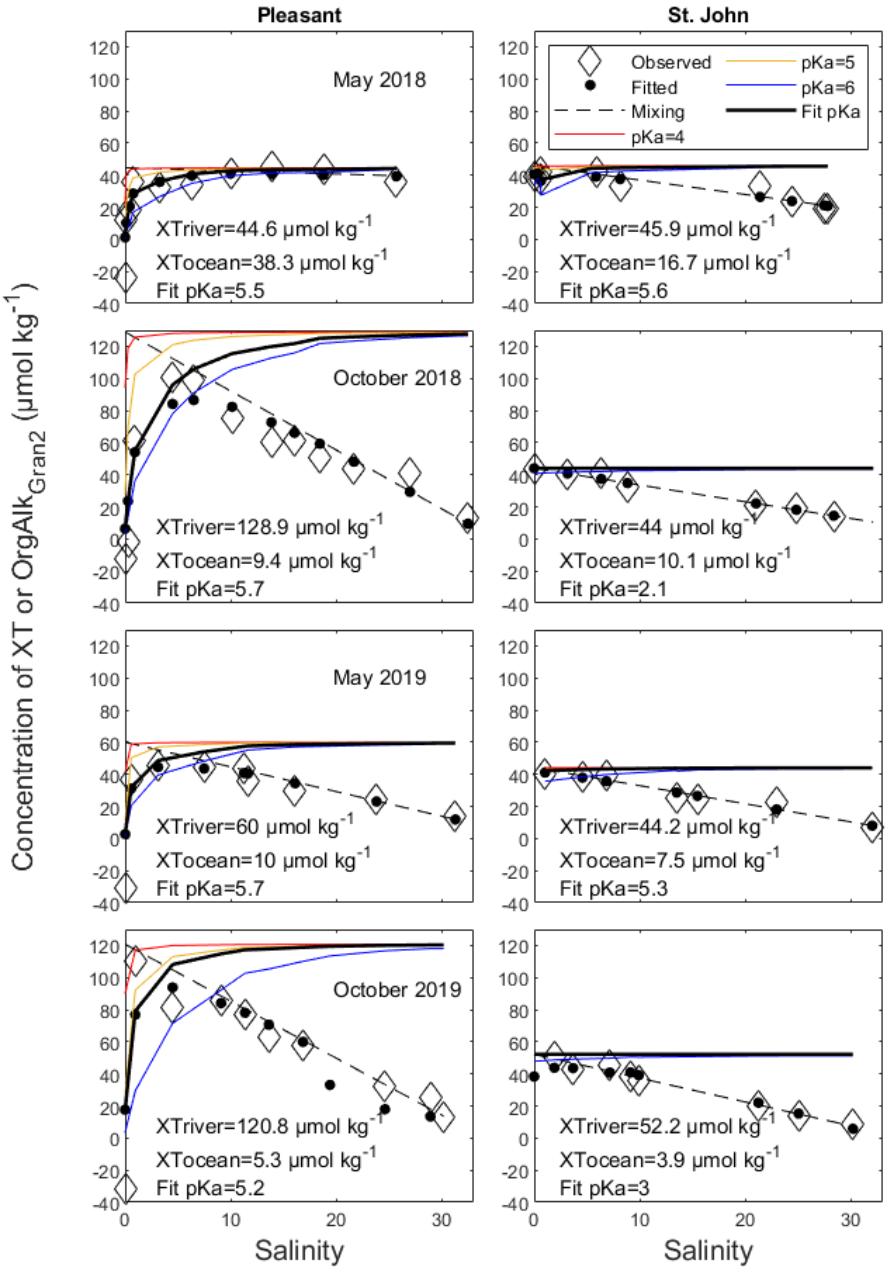

Figure 3.4: Distributions of $OrgAlk_{Gran2}$ (µmol kg^{-1}) observations and fitted empirical results (black solid and dashed lines) plotted against salinity in the Pleasant and St. John estuaries (left and right panels, respectively). From top to bottom, data were collected in May 2018, October 2018, May 2019 and October 2019. Note the different y-axis scales in the Pleasant and St. John plots. Refer to the text for explanation of the empirical fitting calculations. Theoretical results calculated using observed salinity, pH, and pK_a values of 4.0 (red line), 5.0 (orange line) and 6.0 (blue line) are shown to illustrate pK_a influence.

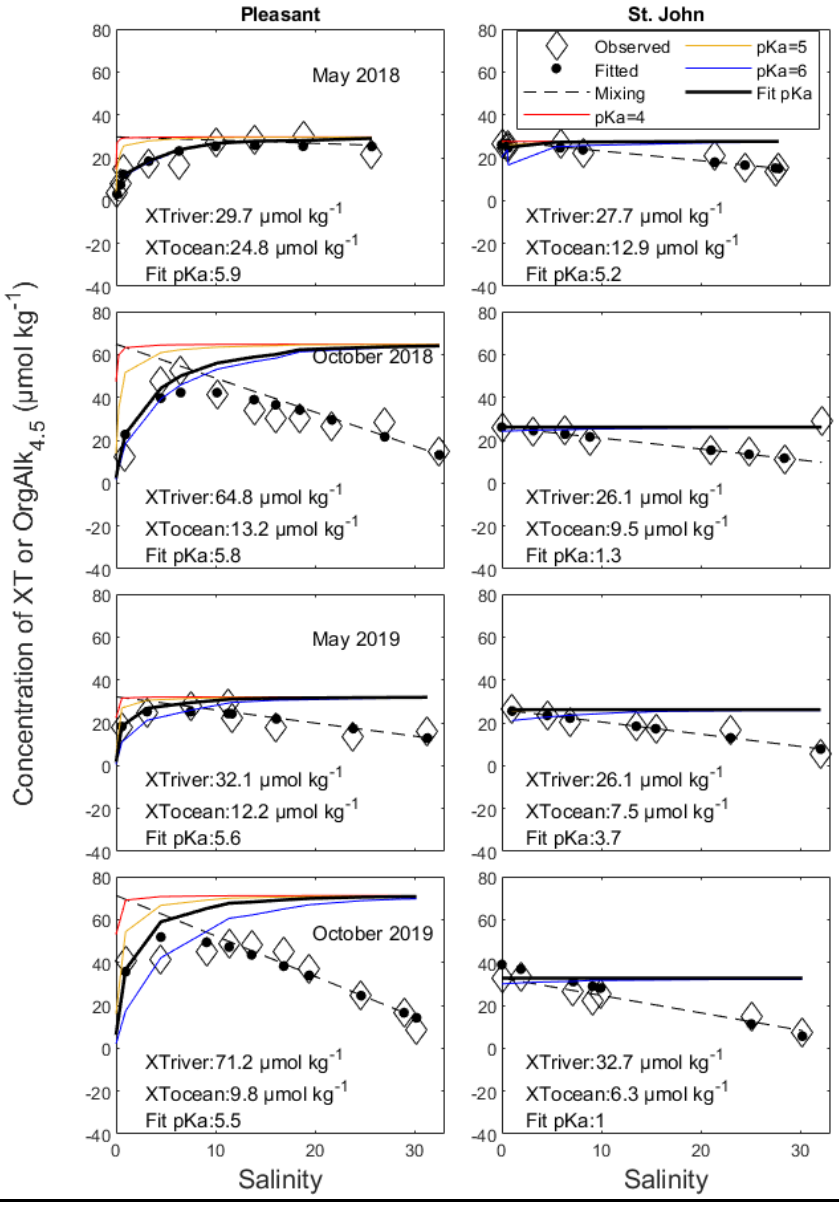

Figure 3.5: Distributions of $OrgAlk_{4.5}$ (µmol kg^{-1}) observations and fitted empirical results (black solid and dashed lines) plotted against salinity in the Pleasant and St. John estuaries (left and right panels, respectively). From top to bottom, data were collected in May 2018, October 2018, May 2019 and October 2019. Note the different y-axis scales in the Pleasant and St. John plots. Refer to the text for explanation of the empirical fitting calculations. Theoretical results calculated using observed salinity, pH, and pK_a values of 4.0 (red line), 5.0 (orange line) and 6.0 (blue line) are shown to illustrate pK_a influence.

3.4 Discussion

Organic alkalinity was present in both the Pleasant and St. John endmembers and estuary samples during all surveys. Indeed, measurable concentrations of organic alkalinity were present in certified reference material as well, a result which confirms findings reported by Sharp and Byrne (2021). Those authors described a method similar to our $OrgAlk_{4.5}$ measurement, and CRM organic alkalinity concentrations (10.5, 10.9, and 7.6 µmol kg^{-1} for Batches 172, 176 and 183, respectively, applying the boron:salinity ratio of Uppström 1974) comparable to the concentration we measured in Batch 185 (5.2 µmol kg^{-1}, applying the Uppström ratio). The ubiquitous presence of organic alkalinity in natural waters from terrestrial to marine systems requires an understanding of the concentrations and chemical nature of this material if total alkalinity measurements are to be accurately used in carbon system calculations (Sharp and Byrne 2020).

Concentrations of $OrgAlk_{Gran2}$ and $OrgAlk_{4.5}$ in the Pleasant and St. John estuaries were comparable to those reported in other studies (Figure 3.6, Table 3.2), although the negative Pleasant $OrgAlk_{Gran2}$ is larger than previously reported. Pleasant Estuary $OrgAlk_{Gran2}$ levels and distributions with salinity during October surveys were similar to those reported for the Satilla estuary by Cai et al. (1998), whose analytical approach was used for the $OrgAlk_{Gran2}$ measurements in this study and whose surveys of the Georgian estuary were also conducted in October. The Satilla zero-salinity endmember also had a very high DOC concentration (about 2170 µmol kg^{-1}) resembling the Pleasant river endmember concentrations (1767 and 1944 µmol kg^{-1} in October

2018 and 2019, respectively). Kuliński et al. (2014) also measured very high OrgAlk concentrations in two Baltic rivers, the Oder and Vistula (184 and 265 μmol kg^{-1}, respectively). The Oder (505 μmol kg^{-1}) and Vistula (614 μmol kg^{-1}) DOC concentrations were lower than those in the Satilla River or the elevated Pleasant River DOC in October, but were quite similar to the Pleasant River DOC concentrations in May (545 and 695 μmol kg^{-1} in May 2018 and 2019, respectively) and St. John endmember DOC concentrations overall. The Oder and Vistula both had much higher total alkalinity (2563 and 3366 μmol kg^{-1}, respectively) than the Satilla, Pleasant or St. John rivers. While the Satilla estuary pH shown in Cai et al. (1998) was not as low as our Pleasant endmember observations, the Satilla pH did approach 5.5 (on the NBS scale) at the endmember, the lowest level registered among the studies presented in Table 3.2.

The Altamaha estuary presented by Cai et al. (1998) most closely resembled the conditions we observed in the St. John, with comparable $OrgAlk_{Gran2}$ (about 5-50 μmol kg^{-1}), DOC concentrations (about 350-750 μmol kg^{-1}) and pH and Alk_{Gran1} near the river endmember (about 6.6 on the NBS scale and 500 μmol kg^{-1}, respectively). The Alk_{Gran1} and pH of the Baltic sites in Kuliński et al. (2014) were much higher than those in the St. John, with lower DOC concentrations as well. Overall, the Satilla estuary is the closest analogue to the St. John Estuary, while the Altamaha is the closest analogue to the St. John estuary from systems described in the literature.

Table 3.2: Organic alkalinity ranges reported by several studies in estuary or coastal ocean systems, the range of salinity ('nr' indicating the salinity was not reported) in each study, the method of OrgAlk determination, and the referring study. The Gran2 and Endpoint 4.5 methods correspond to those described in this work, while the $\Delta OrgAlk_{(TA,DIC,pH)}$ method employed measurements of total alkalinity, dissolved inorganic carbon and pH, together with calculated dissociation constants, to overdetermine the inorganic carbon system and calculate OrgAlk.

System	OrgAlk Range ($\mu mol\ kg^{-1}$)	Salinity Range	Method	Study
Satilla Estuary	25 - 115	0 - 27	Gran2	Cai et al. 1998
Altamaha Estuary	10 - 50	0 - 32	Gran2	Cai et al. 1998
Savannah Estuary	20 - 40	0 - 25	Gran2	Cai et al. 1998
Baltic Sea	22 - 58	3 - 8	$\Delta OrgAlk_{(TA,DIC,pH)}$	Kulinski et al. 2014
N. Gulf California	0 - 120	nr	$\Delta OrgAlk_{(TA,DIC,pH)}$	Hernandez-Ayon et al. 2007
San Diego Bay	100 - 200	nr	$\Delta OrgAlk_{(TA,DIC,pH)}$	Hernandez-Ayon et al. 2007
San Quintin Bay	0 - 70	nr	$\Delta OrgAlk_{(TA,DIC,pH)}$	Hernandez-Ayon et al. 2007
Gulf of Mexico/Florida	(-19) - 90	20 - 38	$\Delta OrgAlk_{(TA,DIC,pH)}$	Yang et al. 2015
Gulf of Mexico/Florida	0 - 40	22 - 33	Spectrophotometric Titration	Yang et al. 2015
Baltic Sea	(-8) - 50	7 - 14	$\Delta OrgAlk_{(TA,DIC,pH)}$	Hammer et al. 2017
Waquoit Bay, Massachusetts	20 - 80	22 - 31	Gran2	Song et al. 2020
Pleasant Estuary Gran2	(-31.9) - 110	0 - 32	Gran2	This study
Pleasant Estuary 4.5	4 - 52	0 - 32	Endpoint 4.5	This study
St. John Estuary Gran2	7 - 51	1 - 30	Gran2	This study
St. John Estuary 4.5	6 - 55	1 - 30	Endpoint 4.5	This study

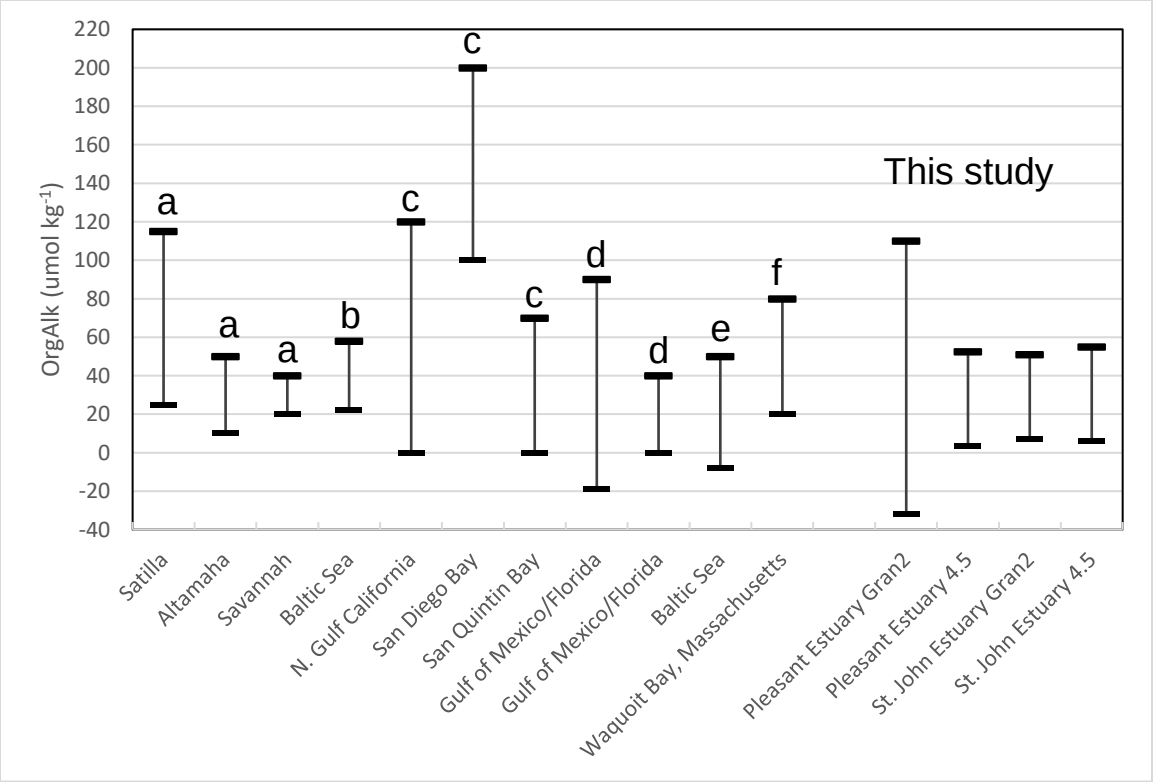

Figure 3.6: Ranges of OrgAlk observed in estuary or coastal waters as reported by other studies, as well as ranges from this work. Refer to Table 3.2 for more details. The studies listed were: (a) Cai et al. 1998 (b) Kuliński et al. 2014 (c) Hernández-Ayon et al. 2007 (d) Yang et al. 2015 (e) Hammer et al. 2017 (f) Song et al. 2020.

3.4.1 Middle-estuary OrgAlk Maxima

A feature of organic alkalinity mixing in the Pleasant Estuary surveys was a peak of $OrgAlk_{Gran2}$ and $OrgAlk_{4.5}$ in the middle of the salinity gradient. While this peak was present in all the Pleasant Estuary surveys, it was not as clearly present in the St. John surveys, Furthermore, the salinity of highest $OrgAlk_{Gran2}$ and $OrgAlk_{4.5}$ was not consistent among Pleasant Estuary surveys. For example, in October 2018 the peak in the Pleasant Estuary was between salinities 3-6.5, while in May 2018 the Pleasant peak was between salinities 14-19. The salinity of maximum organic alkalinity also varied

between $OrgAlk_{Gran2}$ and $OrgAlk_{4.5}$, as in the example of the October 2019 Pleasant data, where $OrgAlk_{4.5}$ rapidly reached a maximum at salinity 1.0, while the maximum $OrgAlk_{Gran2}$ was measured around salinity 11-14.

The low-salinity region of estuary mixing is typically the site of dramatic pH increases, particularly in the acidic Pleasant system. Cai et al. (1998) documented similar mid-estuary organic alkalinity maxima, and attributed the phenomenon to two different processes: rapid pH change in early estuary mixing followed by conservative mixing of the peak organic alkalinity with the coastal endmember over a salinity gradient. If charge groups are present in the organic material whose pK_a is higher than the *in-situ* river pH, this rapid pH increase during estuary mixing would result in those groups being increasingly deprotonated at ambient estuary pH and thus available for titration with acid. Cai et al. (1998) theorized that this pH change is of more importance to estuary organic alkalinity contributions than the potential dependence of organic pK_a on ionic strength (i.e., salinity). Others have pointed out that salt marshes and mangroves represent inputs of alkalinity- presumably at least partly of organic components- to the estuary independent of the river and ocean endmembers (Wang et al. 2016, Sippo et al. 2016), which could explain the mid-estuary maxima in our observations. Song et al. (2020) proposed a large intertidal salt marsh OrgAlk contribution, representing 36% of the total OrgAlk concetration, during a time of limited freshwater input. However, recent experimental work by Hinckley (2021) using samples collected during our October 2019 surveys provides a counterargument. Hinckley prepared serial dilutions of Pleasant River and St. John River water with CRM to achieve mixed salinities of 0.25, 0.5, 0.75, 1.0, 2.5, 5, 10, 15 20, 25, and 30, to

artificially simulate the estuary mixing process. The pH_T of the Pleasant River sample was 3.933, while the pH_T of the St. John River sample was 6.924. The author then performed an Alk_{Gran1} titration, added CO_2-free NaOH to a pH_T of 8.5, and finally performed a second whole-pH titration using very small acid increments to a pH_T of 3.0. These incremental acid additions allowed for the calculation of $OrgAlk_{Gran2}$ and $OrgAlk_{4.5}$ from various initial pH_T values. When the initial titration pH_T for each salinity mixture was selected to match as closely as possible the river endmember pH for each salinity mixture- thus effectively removing the estuary pH_T change cited by Cai et al. (1998)- there was still a mid-salinity peak of $OrgAlk_{Gran2}$ and $OrgAlk_{4.5}$ observed in the serial dilution series, despite the presumed dilution of organic material with the addition of CRM. Under the conditions of these titrations and data analyses the only changes were in the mixing of river and CRM inorganic and organic materials, and the change in ionic strength- the initial pH_T of each titration calculation was effectively the same (near 3.933 for the Pleasant and near 6.924 for the St. John). Thus the pK_a dependence of organic charge sites on ionic strength may be more important than previously reported and bears further investigation, as increasing ionic strength appears to affect organic charge sites in a manner similar to increasing pH_T.

3.4.2 OrgAlk Fitting

The Cai Fit calculations returned values of K_a, XT_{river} and XT_{ocean} for each estuary survey, which were able to reproduce the distributions of $OrgAlk_{Gran2}$ and $OrgAlk_{4.5}$ over the estuary salinity gradient reasonably well (Figures 3.4 and 3.5), although the Cai Fit tended to underestimate the strongly negative Pleasant river $OrgAlk_{Gran2}$ values (which

were probably equivalent to an OrgAlk concentration of zero, with the negative alkalinity due to excess [H^+] below the 4.5 equivalence point) and the highest mid-salinity OrgAlk values. Overall differences from the observed organic alkalinity concentrations were small, ranging from 2 to 6 µmol kg^{-1} with the notable exception of the Pleasant October surveys, where much of the discrepancy stems from relatively large differences in the very low salinity samples (Table 3.3). We present model results for a single charge group; the addition of a second or third charge group produced minimal improvements in model fit to the observed data.

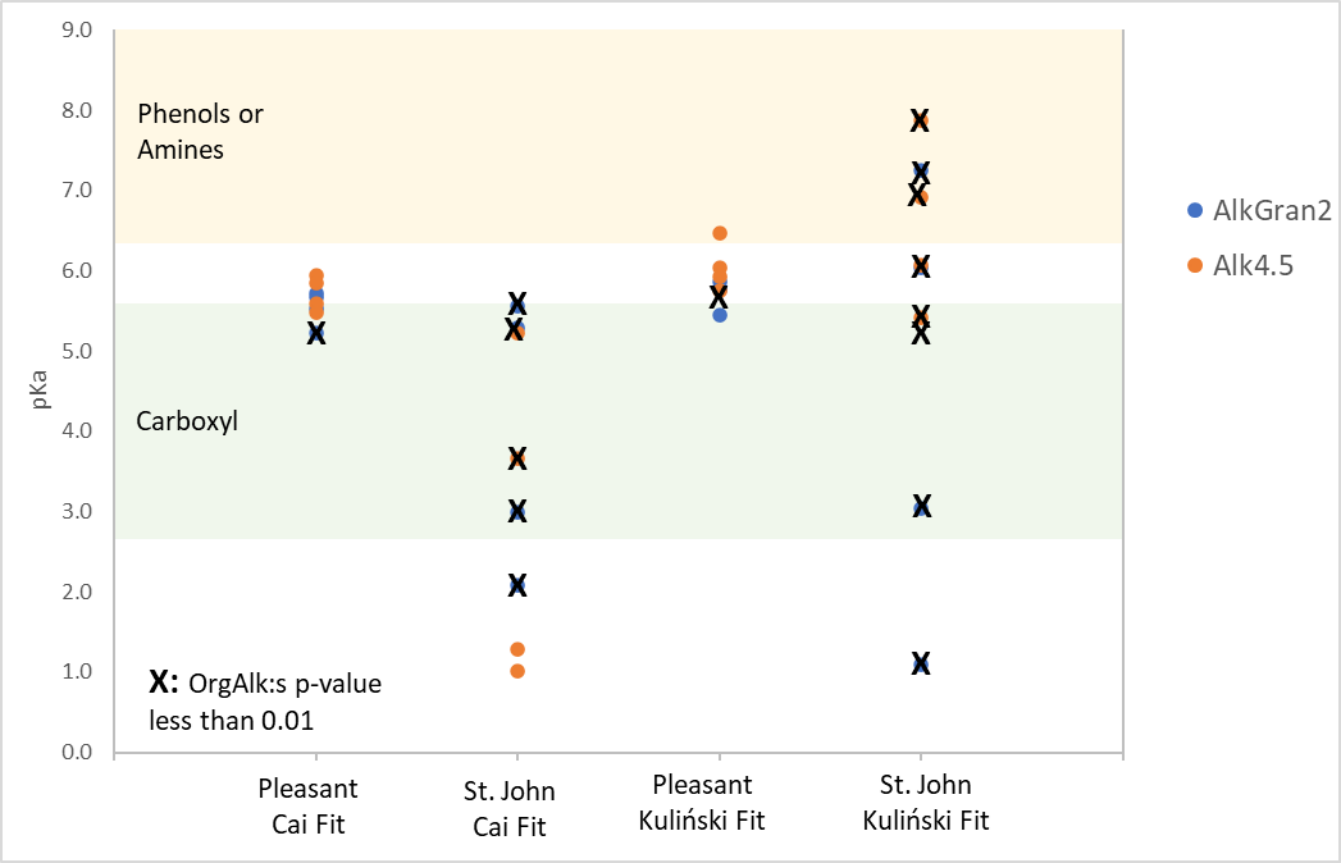

Figure 3.7: Fitted pK_a values for each estuary survey. The Cai Fit is based on the approach of Cai et al. (1998) and the Kuliński Fit from Kuliński et al. (2014), as described in sections 3.2.7 and 3.2.8, respectively. Blue circles represent pK_a values calculated from $OrgAlk_{Gran2}$ measurements, orange circles were calculated from

$OrgAlk_{4.5}$ measurements. Black X symbols are placed over circles where the estuary OrgAlk and salinity were highly linearly correlated ($p<0.01$) and not sensitive to pK_a. The horizontal green band shows the range of carboxyl function group pK_a identified by Paxéus and Wedborg (1985). The horizontal orange bar shows the phenol or amine function group pK_a range from the same study.

Table 3.3: Root mean square error (RMSE) and coefficient of determination (r^2, between fitted and observed OrgAlk) for the Cai Fit and Kulinski Fit results for each estuary survey.

	Results from Cai Fit		Results from Kulinski Fit	
survey	RMSE µmol kg^{-1}	r^2	RMSE µmol kg^{-1}	r^2
$OrgAlk_{Gran2}$				
Pleasant May2018	5.4	0.87	8.7	0.73
St. John May 2018	3.2	0.89	8.1	0.69
Pleasant October 2018	10.1	0.89	10.9	0.88
St. John October 2018	1.9	0.98	3.7	0.92
Pleasant May 2019	6.1	0.85	7.9	0.78
St. John May 2019	2.1	0.90	3.0	0.94
Pleasant October 2019	15.1	0.79	21.3	0.69
St. John October 2019	2.4	0.98	11.8	0.55
$OrgAlk_{4.5}$				
Pleasant May2018	3.6	0.85	4.7	0.83
St. John May 2018	1.6	0.91	5.2	0.68
Pleasant October 2018	5.5	0.73	7.7	0.73
St. John October 2018	1.4	0.95	2.4	0.87
Pleasant May 2019	2.8	0.67	5.1	0.61
St. John May 2019	2.1	0.90	2.1	0.93
Pleasant October 2019	5.4	0.86	11.6	0.66
St. John October 2019	2.0	0.96	3.1	0.90

Results from the Cai Fit calculations included the fitted pK_a of the organic charge group (Figure 3.7) and estimates of the correspondence between calculated and observed OrgAlk (Table 3.3). The Pleasant pK_a value was generally higher than that in the St. John, with the exception of the $OrgAlk_{Gran2}$ results from October 2019. Overall, 10 of the 16 pK_a values fell in the range of 5.2 and 5.9, with 5 values below this range and one pK_a above. This falls between the Satilla estuary Group I and Group II pK_a values reported by Cai et al. (1998), matches the river fulvic Group III pK_a reported by Paxéus and Wedborg (1985), and generally represents a pK_a value between the lower pK_a values reported for soil humics and streams and the higher values reported for estuaries or coastal seas (Table 3.4). St. John Cai Fit pK_a values were mostly below 4, indeed sometimes outside the titration range of the OrgAlk analyses (Figure 3.7). A charge group with such a low pK_a would never be protonated in a natural estuary environment, and only partially protonated during laboratory titrations. For surveys with unusually low pK_a values (i.e., the St. John in October 2018 and 2019), we experimented with varying the upper and lower pK_a bounds of the fitting function by setting these bounds to the approximate range of pH experienced by organic material during the laboratory titration procedure (i.e., pH 3.0-8.5); the resulting pK_a was invariably selected to be at the lower bound of 3.0 and the RMSE and r^2 statistics remained virtually identical. St. John surveys with low modeled pK_a also exhibited very linear distributions of OrgAlk and pH with salinity (Figures 3.4 and 3.5), and these inputs produced a conservative distribution of OrgAlk concentrations and a low pK_a. It is clear from Figures 3.4 and 3.5 that the pK_a value calculated in the St. John surveys has little effect on the fitted OrgAlk, as the OrgAlk distributions are so highly related to salinity. If

pK_a values are ignored when the linear regression of OrgAlk and salinity returns a p-value less than 0.01 one Pleasant estuary survey is ignored (the October 2019 $OrgAlk_{4.5}$ value) while all St. John estuary pK_a values are ignored (Figure 3.7). This merely reflects a limitation of employing the Cai Fit approach to estimate pK_a from conservative estuary OrgAlk distributions, instead of directly modeling pK_a from sample titration data.

Table 3.3: Aquatic pK_a values determined by several studies.

Sample type	Reported pK_a	Authors
Soil Porewater 1	5.3-5.88	Badr et al. (2012)
Soil Porewater 2	5.1-5.75	
Soil Porewater 3	4.9-5.2	
Sewage Sludge	5.25-6.45	
Nile Water Hyacinch compost	6.5-6.75	
Soil humics	4.28	Andjelkovic et al. (2006)
Adirondack soil/stream humics	3.85	Cronan and Aiken (1985)
Humics	4	Lozovik (2005)
Bickford (MA) watershed	3.5-3.7	Eshleman and Hemond (1995)
River fulvic acid Group I	2.66	Paxeus and Wedborg (1985)
River fulvic acid Group II	4.21	
River fulvic acid Group III	5.35	
River fulvic acid Group IV	6.65	
River fulvic acid Group V	8.11	
River fulvic acid Group VI	9.54	
Satilla Estuary Group I	4.46	Cai et al. (1998)
Satilla Estuary Group II	6.64	
Satilla Estuary Group III	8.94	
Altamaha Estuary	6.7	
Savannah Estuary	7.1	
Intertidal Salt Marsh Group I	4.1-5.5	Song et al. (2020)
Intertidal Salt Marsh Group II	7.4-9.8	
Baltic Sea	7.53	Kulinski et al. (2014)
Baltic Sea	7.27	Hammer et al. (2017)
Tampa Bay coastal waters	5.31, 7.05	Yang et al. 2015
Tampa Bay coastal waters	5.45, 7.32	Yang et al. 2015
Pleasant Estuary	5.3-5.9	This Work
St. John Estuary	5.2-5.6	This Work

3.4.3 Differences between $OrgAlk_{Gran2}$ and $OrgAlk_{4.5}$

We chose to measure the organic alkalinity of CO_2-free samples using two different approaches: a Gran-style interpretation of titration data between pH 3.5-3.0 ($OrgAlk_{Gran2}$), and a separate endpoint titration to the total alkalinity equivalence pH of 4.5 ($OrgAlk_{4.5}$). If no OrgAlk was present in solution, or if the organic charge groups had pK_a values considerably higher than 4.5 or lower than 3.0 (and thus became totally protonated or remained deprotonated during both titration procedures, respectively) then in principle the concentrations of $OrgAlk_{Gran2}$ and $OrgAlk_{4.5}$ would be equal. Some of the modeled Pleasant and St. John pK_a values shown in Figure 3.7 are consistent with this idea; for example, the pK_a of 5.9 modeled in the Pleasant using October 2018 $OrgAlk_{4.5}$ measurements would result in the organic charge group being 97% protonated at the pH 4.5 endpoint and 100% protonated at the pH 3.0: a potential 3% difference between $OrgAlk_{Gran2}$ and $OrgAlk_{4.5}$ concentrations simply due to differing degrees of dissociation. However, the mean difference between our Pleasant Estuary measured $OrgAlk_{Gran2}$ and $OrgAlk_{4.5}$ in October 2018 was 37±14%, a difference too large to be explained by the estimated pK_a. Overall for all Pleasant and St. John Estuary surveys the mean difference between $OrgAlk_{Gran2}$ and $OrgAlk_{4.5}$ attributable to the fitted pK_a at pH 3.0 and 4.5 was 15±22%; the mean difference of 32±28% between our measured $OrgAlk_{Gran2}$ and $OrgAlk_{4.5}$ was larger than the pK_a-attributable difference.

If the pK_a of natural organic material does indeed lie below pH 4.5, or the pK_a of one common functional organic group lies below the pH 4.5 threshold, then it is not only possible but expected that the OrgAlk measured at pH 4.5 can be different than that

measured at pH 3.0, but that both measures can be carried out correctly and represent the internally consistent measure at that particular pH. Our work shows that these differences can be substantial. These organic anions may have a pK_a which impacts the titration alkalinity but which would not affect buffering or the overall acid-base chemistry at *in situ* pH, and careful consideration is called for both when measuring OrgAlk and discussing its contribution to TA. Indeed, there does not currently appear to be a good way to include OrgAlk in a quantitative summation of all the alkalinity contributors in aquatic solution. One approach may be to simply use the OrgAlk at pH 4.5 in order to conform to the definition of total alkalinity; however, as the change in behavior of OrgAlk over the pH range is not predictable without knowledge of OrgAlk pK_a, using the OrgAlk value at pH 4.5 may exclude significant behavior differences at lower pH.

While modeling additional charge groups did not appreciably improve the model OrgAlk fit to our observations, it is unlikely that the organic charge groups present in the Pleasant and St John estuaries are actually so uniform in their properties. Instead, it is reasonable to expect that the organic charge group types are polydisperse with a number of distinct pK_a values, as those described by Paxéus and Wedborg (1985) and Cai et al. (1998). The simple model and dataset we employed, which only encompassed the natural pH conditions of the Pleasant and St. John estuaries, could not account for charge groups with a low pK_a, such as the pK_a 2.66 group listed by Paxéus and Wedborg (1985), which was also the most abundant organic charge group in their sample. A charge group with pK_a around this value, together with differences in dissociation among higher- pK_a charge groups as discussed above, could explain the discrepancies between our $OrgAlk_{Gran2}$ and $OrgAlk_{4.5}$ observations.

3.4.4 OrgAlk as a Component of DOC

The Kuliński Fit returned best-fit values of K_{DOC} and f (the weak acid fraction of DOC). DOC concentrations along the salinity gradient were similar among the St. John Estuary surveys, but demonstrated a clear seasonal shift in the Pleasant Estuary, with much higher DOC concentrations at low salinity during the October surveys in comparison to the May surveys (Figure 3.3). These higher DOC concentrations were also reflected in the higher XT_{river} modeled charge group concentrations returned by the Cai Fit calculations for Pleasant Estuary October surveys relative to May surveys (Figure 3.4), and generally higher measured Pleasant Estuary OrgAlk (Figures 3.4 and 3.5). The Pleasant October surveys were conducted after months of very low river flow, which may have resulted in wetlands contributing disproportionately to river flow. It is worthwhile to note, however, that if true this enhancement did not appreciably shift the acid-base character of the Pleasant Estuary DOC as reflected in the Kuliński Fit pK_{DOC} (Figures 3.7, 3.8, 3.9).

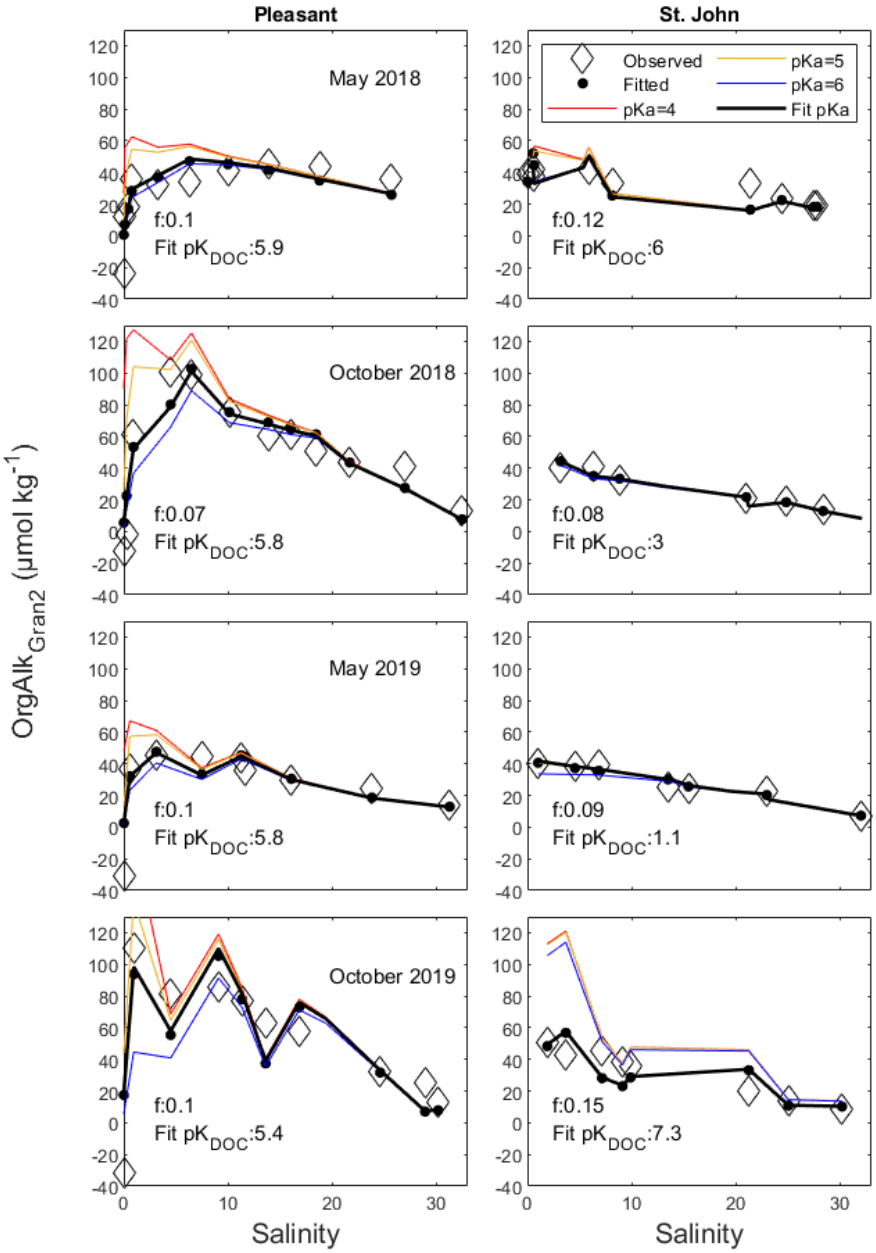

Figure 3.8: Distributions of $OrgAlk_{Gran2}$ (µmol kg^{-1}) observations and empirical Kuliński Fit results (black line) plotted against salinity in the Pleasant and St. John estuaries (left and right panels, respectively). From top to bottom, data were collected in May 2018, October 2018, May 2019 and October 2019. Note the different y-axis scales in the Pleasant and St. John plots. Refer to the text for explanation of the DOC fitting calculations. Theoretical results calculated using observed salinity, pH, and pK_{DOC} values of 4.0 (red line), 5.0 (orange line) and 6.0 (blue line) are shown to illustrate the effect of varying pK_{DOC}.

Estimating $OrgAlk_{Gran2}$ and $OrgAlk_{4.5}$ from modeled f and pK_{DOC} parameters produced concentrations that generally followed the observed distributions with salinity, but with significantly more scatter than comparable model results from the Cai Fit empirical approach. RMSE and r^2 statistics from the DOC approach were generally less robust than those from the mixing model as well (Table 3.3). The same estuary surveys which displayed a high correlation between salinity and OrgAlk and lack of sensitivity to pK_a according to the Cai Fit also returned variable pK_{DOC} values (Figure 3.7), especially in the St. John Estuary Kuliński Fit results. All of the St. John pK_{DOC} were identified as highly dependent on the conservative mixing of OrgAlk with salinity, indicating that the fitted value of pK_{DOC} did not impact OrgAlk distributions. It is possible that the St. John OrgAlk could possess pK_a and pK_{DOC} characteristics similar to those in the Pleasant Estuary (about 5.6 and 5.9, respectively). But as the St. John Estuary pH_T was substantially higher than these pK_a and pK_{DOC} values (the lowest St. John Estuary pH_T was 6.175), and the Cai Fit and Kuliński Fit simulate OrgAlk titrations over the natural pH range of the observations, the organic charge sites remained mostly or fully deprotonated. These results indicate that estimating Pleasant Estuary OrgAlk- either from pK_a, pH_T and salinity (Equation 3.6) or pK_{DOC} and pH_T (Equation 3.7)- may hold some promise, while similar estimates in the St. John estuary will prove difficult.

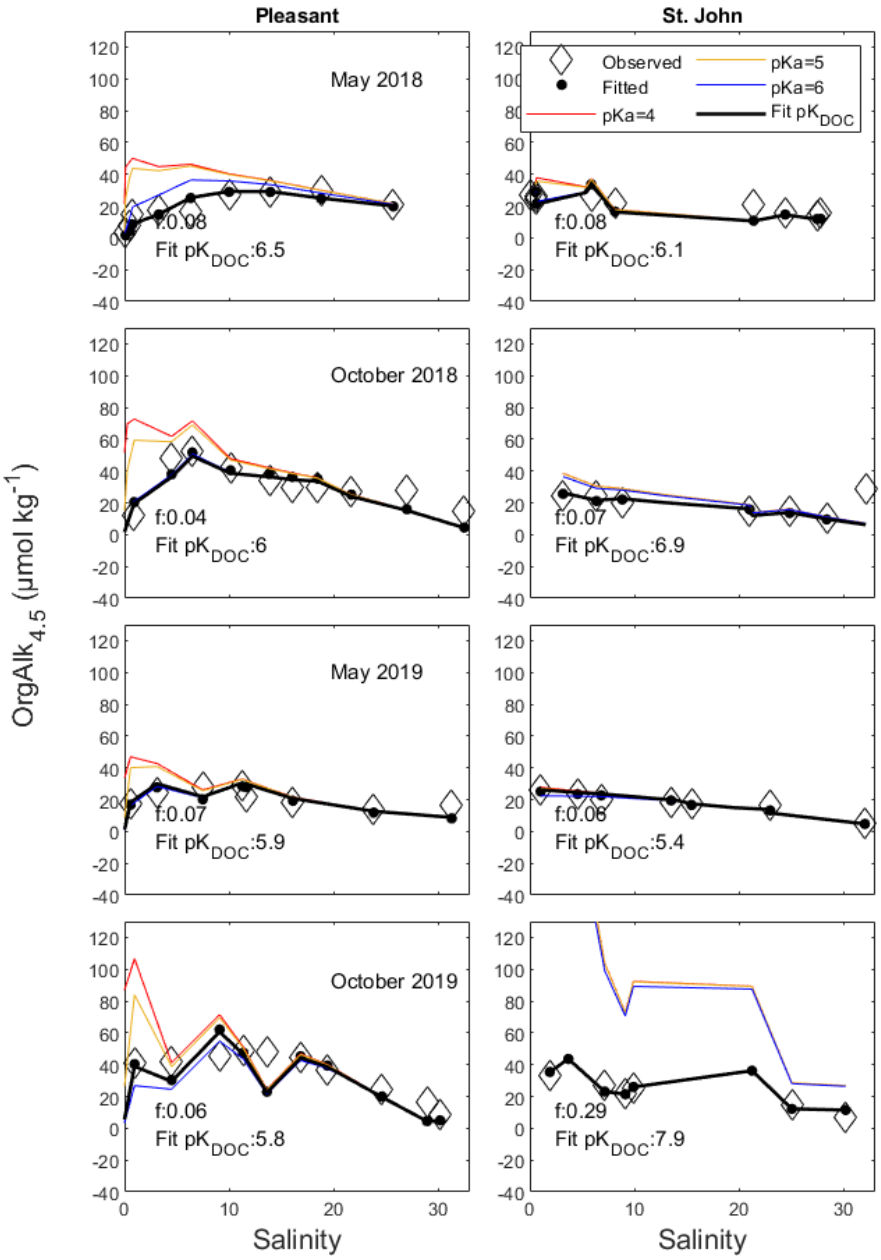

Figure 3.9: Distributions of OrgAlk$_{4.5}$ (µmol kg^{-1}) observations and empirical Kuliński Fit results (black line) plotted against salinity in the Pleasant and St. John estuaries (left and right panels, respectively). From top to bottom, data were collected in May 2018, October 2018, May 2019 and October 2019. Note the different y-axis scales in the Pleasant and St. John plots. Refer to the text for explanation of the DOC fitting calculations. Theoretical results calculated using observed salinity, pH, and pK$_{DOC}$ values of 4.0 (red line), 5.0 (orange line) and 6.0 (blue line) are shown to illustrate pK$_{DOC}$ influence.

3.5 Conclusions

We present some of the first seasonal observations of estuary organic alkalinity distributions, measured by two different analytic approaches, from two estuaries with contrasting river endmember chemistries. OrgAlk constituted a major part of total alkalinity at lower salinities in both estuaries and was an appreciable alkalinity contributor at higher salinities and in certified reference material. Distributions of OrgAlk and DOC with salinity varied seasonally in the Pleasant Estuary but were similar between seasons in the St. John estuary. Two empirical fits were applied to the observations which returned bulk dissociation constants (pK's) which differed between estuaries and also differed in terms of their degree of consistency. While many of the bulk pK values indicated OrgAlk buffering above the total alkalinity equivalence point of pH 4.5, contrasts between $OrgAlk_{Gran2}$ and $OrgAlk_{4.5}$ results for the same samples indicate that a lower-pH charge group may be present as well. This lower-pH charge group may not have an influence on *in situ* alkalinity under natural pH conditions, but poses a potential challenge to the interpretation of titration data. Future efforts to constrain pK characteristics should focus on development of a robust incremental titration procedure, which would provide the data needed to model multiple pK charge groups, and examination of the differing effects of changing salinity and pH upon pK characteristics.

CONCLUSIONS

This dissertation presented some of the first highly temporally and spatially resolved TA measurements in the coastal ocean along the USA East Coast, in addition to a unique analysis of seasonal organic alkalinity distributions in two East Coast estuaries. In Chapter 1, TA along the East Coast and shelf-front break showed a pattern consistent with regional circulation, but seasonal and inter-annual distributions of TA and salinity were changeable and not fully described by previous studies. These changes are likely due to biological processes and shifts in source water masses entering the region, which in turn dictate the TA and salinity entering the East Coast region, and were not consistent with the seasonal TA and salinity patterns reflected in a newly-assembled historical regional dataset. Ocean acidification (strictly as the absorption of elevated atmospheric CO_2 by the ocean) represents one direct and relatively predictable effect of anthropogenic climate change upon the marine environment. On the other hand, indirect effects such as heating, changes in precipitation patterns, and changes in large-scale ocean currents will surely result in altered regional ocean chemistry in ways that are complex, interrelated, and difficult to predict. The analytical capability demonstrated in Chapter 1 offers a way to monitor regional ocean chemistry broadly, at high frequency, and with relatively little supervision or expense. This type of monitoring capability can be especially powerful when paired with concurrent measurements of pCO_2 or with satellite products, and will be an important tool in tracking the progression and effects of global climate change.

Chapter 2 used the high-frequency hourly TA (and associated temperature, salinity and pCO_2) measurements at the UNH coastal laboratory to examine the effects of various processes upon buffering and pH. The relatively simple concept of ocean acidification becomes vastly more complex in shelf and coastal regions, where biogeochemical processes and freshwater inputs can exacerbate or ameliorate acidification, and it can be difficult to attribute short- and long-term changes to specific causes. The data collected for this project allowed for the examination of the potential impact of various processes on coastal chemistry, and a simple mechanistic model was used to apportion contributions of ecosystem metabolism, mixing, and air-sea exchange to changes in TA and DIC. The results indicated that at this site mixing and temperature changes dictated much of the change in buffering and pH, and potential biogeochemical contributions to acidification were overshadowed by enhanced buffering driven by seasonal reductions in freshwater inputs. At this time the relevance of these findings to other coastal sites is undetermined, but the presented monitoring approach, data analysis techniques and model application offer some potential tools for coastal resource managers or other interested parties who may wish to examine acidification at other sites in a similar manner. A logical next step in pursuit of this research area would be to replicate the analytical capability at the UNH Jackson Estuary Laboratory, located in Great Bay itself, to see if the processes driving TA and DIC change at that location agree with or differ from those at the coastal lab.

Moving even further upstream, Chapter 3 detailed several surveys of organic alkalinity in two estuary systems. One estuary (the Pleasant) was showed remarkable acidity and organic alkalinity levels, which varied seasonally with dissolved organic

carbon concentrations. The other estuary (the St. John) showed fairly constant organic alkalinity and dissolved organic carbon distributions. Examination of the organic acid dissociation constant (pK_a) in each estuary via two modeling approaches produced varied results, and a reliable method for direct pK_a determination via a titration approach is clearly needed. This is especially important as there is increasing evidence that organic alkalinity is a nearly universal component of TA, including in open ocean waters and reference materials. This component is sometimes quite small, but can also sometimes be quite large in estuary waters, and appears to be repeatably measurable. Without a knowledge of the pK_a of the organic alkalinity component, however, it is difficult or impossible to determine whether the presence of organic alkalinity is an analytical concern at the low measurement pH, or whether organic alkalinity has real effects on pH and buffering at real estuary and ocean conditions. A standardized method for the determination of organic alkalinity and pK_a would represent a significant contribution to the understanding of the ocean and coastal buffering system.

LIST OF REFERENCES

Aßmann, S., Frank, C., Petersen, W., Körtzinger, A., 2013. Autonomous pH and alkalinity sensors for the characterization of the carbonate system in coastal areas. Presented at the EGU General Assembly Conference Abstracts, pp. EGU2013-8760.

AOML. HB1701 Cruise Report. Accessed September 25, 2020. https://www.aoml.noaa.gov/ocd/gcc/shortcruises/HB1701/33HH20170210-HB1701-Readme.pdf.

Abril, G., Bouillion, S., Darchambeau, F., Teodoru, C.R., Marwick, T.R., Tamooh, F., Omengo, F.O., Geeraert, N., Deirmendjian, L., Poisenaere, P. and A.V. Borges. 2014. Technical Note: Large overestimation of pCO2 calculated from pH and alkalinity in acidic, organic-rich freshwaters. Biogeosciences Discuss. 11: 11701-11725.

Alin, S. R., R. A. Feely, A. G. Dickson, J. M. Hernández-Ayón, L. W. Juranek, M. D. Ohman, and R. Goericke. 2012. Robust empirical relationships for estimating the carbonate system in the southern California Current System and application to CalCOFI hydrographic cruise data (2005–2011). J. Geophys. Res. **117**: C05033. doi:10.1029/2011JC007511.

Andjelkovic, T., J. Perovic, M. Purenovic, S. Blagojevic, R. Nikolic, D. Andjelkovic, and A. Bojic. 2006. A direct potentiometric titration study of the dissociation of humic acid with selectively blocked functional groups. Eclética Química 31: 39–46. doi:10.1590/S0100-46702006000300005

Badr, M. H., M. H. El-Halafawi, and E. R. a. E. Zeid. 2012. Comparison between the effect of ionic strength on acidity and dissociation constants of humic acids extracted from sewage sludge and nile water hyacinth composts. Global Journal of Environmental Research 6: 36–43.

Bakker, D.C.E., Pfeil, B., Landa, C.S., Metzl, N., O'Brien, K.M., Olsen, A., Smith, K., Cosca, C., Harasawa, S., Jones, S.D., Nakaoka, S., Nojiri, Y., Schuster, U., Steinhoff, T., Sweeney, C., Takahashi, T., Tilbrook, B., Wada, C., Wanninkhof, R., Alin, S.R., Balestrini, C.F., Barbero, L., Bates, N.R., Bianchi, A.A., Bonou, F., Boutin, J., Bozec, Y., Burger, E.F., Cai, W.-J., Castle, R.D., Chen, L., Chierici, M., Currie, K., Evans, W., Featherstone, C., Feely, R.A., Fransson, A., Goyet, C., Greenwood, N., Gregor, L., Hankin, S., Hardman-Mountford, N.J., Harlay, J., Hauck, J., Hoppema, M., Humphreys, M.P., Hunt, C.W., Huss, B., Ibánhez, J.S.P., Johannessen, T., Keeling, R., Kitidis, V., Körtzinger, A., Kozyr, A., Krasakopoulou, E., Kuwata, A., Landschützer, P., Lauvset, S.K., Lefèvre, N., Monaco, C.L., Manke, A., Mathis, J.T., Merlivat, L., Millero, F.J., Monteiro, P.M.S., Munro, D.R., Murata, A., Newberger, T., Omar, A.M., Ono, T., Paterson, K., Pearce, D., Pierrot, D., Robbins, L.L., Saito, S., Salisbury, J., Schlitzer, R., Schneider, B., Schweitzer, R., Sieger, R., Skjelvan, I., Sullivan, K.F., Sutherland, S.C., Sutton, A.J., Tadokoro, K., Telszewski, M., Tuma, M., Heuven, S.M.A.C. van, Vandemark, D., Ward, B., Watson, A.J., Xu, S., 2016. A multi-decade record of high-quality fCO2 data in version 3 of the Surface Ocean CO2 Atlas (SOCAT). Earth System Science Data 8, 383–413. https://doi.org/10.5194/essd-8-383-2016Balch, W. M. 2018. The Ecology, Biogeochemistry, and Optical Properties of Coccolithophores. Annual Review of Marine Science 10: 71–98. doi:10.1146/annurev-marine-121916-063319.

Balch, W. M. 2018. The Ecology, Biogeochemistry, and Optical Properties of Coccolithophores. Annual Review of Marine Science 10: 71–98. doi:10.1146/annurev-marine-121916-063319.

Barbero, L., D. Pierrot, R. Wanninkhof, and others. 2017. Third Gulf of Mexico Ecosystems and Carbon Cycle (GOMECC-3) Cruise. Cruise Report. doi :10.25923/y6m9-fy08

Barbier, E.B., Hacker, S.D., Kennedy, C., Koch, E.W., Stier, A.C. and B.R. Silliman. 2011. The value of estuarine and coastal ecosystem services. Ecological Monographs 81(2): 169-193.

Bates, N.R., Michaels, A.F., Knap, A.H., 1996a. Seasonal and interannual variability of oceanic carbon dioxide species at the U.S. JGOFS Bermuda Atlantic Time-series Study (BATS) site. Deep Sea Research Part II: Topical Studies in Oceanography 43, 347–383. https://doi.org/10.1016/0967-0645(95)00093-3

Bates, N.R., Michaels, A.F., Knap, A.H., 1996b. Alkalinity changes in the Sargasso Sea: geochemical evidence of calcification? Marine Chemistry 51, 347–358. https://doi.org/10.1016/0304-4203(95)00068-2

Bates, N.R., 2001. Interannual variability of oceanic CO2 and biogeochemical properties in the Western North Atlantic subtropical gyre. Deep Sea Research Part II: Topical Studies in Oceanography 48, 1507–1528. https://doi.org/10.1016/S0967-0645(00)00151-X

Bauer, J. E., W.-J. Cai, P. A. Raymond, T. S. Bianchi, C. S. Hopkinson, and P. A. G. Regnier. 2013. The changing carbon cycle of the coastal ocean. Nature 504: 61–70. doi:10.1038/nature12857.

Bilgili, A., J. A. Proehl, D. R. Lynch, K. W. Smith, and M. R. Swift. 2005. Estuary/ocean exchange and tidal mixing in a Gulf of Maine Estuary: A Lagrangian modeling study. Estuarine, Coastal and Shelf Science 65: 607–624. doi:10.1016/j.ecss.2005.06.027

Borges, A. V., S. Djenidi, G. Lacroix, J. Théate, B. Delille, and M. Frankignoulle. 2003. Atmospheric CO2 flux from mangrove surrounding waters. Geophys. Res. Lett. 30: 1558. doi:10.1029/2003GL017143.

Borges, A. V. 2005. Do we have enough pieces of the jigsaw to integrate CO2 fluxes in the coastal ocean? Estuaries 28: 3–27. doi:10.1007/BF02732750.

Bouillon, S., F. Dehairs, B. Velimirov, G. Abril, and A. V. Borges. 2007. Dynamics of organic and inorganic carbon across contiguous mangrove and seagrass systems (Gazi Bay, Kenya). J. Geophys. Res. 112: G02018. doi:10.1029/2006JG000325.

Breitburg, D.L., Salisbury, J., Bernhard, J.M., Cai, W.-J., Dupont, S., Doney, S.C., Kroeker, K.J., Levin, L.A., Long, W.C., Milke, L.M., Miller, S.H., Phelan, B., Passow, U., Seibel, B.A., Todgham, A.E., Tarrant, A.M., 2015. And on Top of All That…: Coping with Ocean Acidification in the Midst of Many Stressors. Oceanography 28, 48–61.

Brickman, D., D. Hebert, and Z. Wang. 2018. Mechanism for the recent ocean warming events on the Scotian Shelf of eastern Canada. Continental Shelf Research 156: 11–22. doi:10.1016/j.csr.2018.01.001.

Broecker, W. S., T. Takahashi, H. J. Simpson, and T.-H. Peng. 1979. Fate of Fossil Fuel Carbon Dioxide and the Global Carbon Budget. Science 206: 409–418. doi:10.1126/science.206.4417.409

Brown, T. 2006. Non-reactive gas dynamics in the Piscataqua Estuary inlet. University of New Hampshire.

Burdige, D.J. 2011. Estuarine and coastal sediments—coupled biogeochemical cycling. Treatise Estuarine Coastal Sci., 5, 279–316.

Butman, D. and P.A. Raymond. 2011. Significant efflux of carbon dioxide from streams and rivers in the United States. Nature geosciences: doi: 10.1038/NGEO1294.

Caffrey, J. M. 2004. Factors controlling net ecosystem metabolism in U.S. estuaries. Estuaries 27: 90–101. doi:10.1007/BF02803563.

Cai, W.-J., and Y. Wang. 1998. The chemistry, fluxes, and sources of carbon dioxide in the estuarine waters of the Satilla and Altamaha Rivers, Georgia. Limnology and Oceanography 43: 657–668. doi:10.4319/lo.1998.43.4.0657.

Cai, W.-J., Y. Wang, and R. E. Hodson. 1998. Acid-Base Properties of Dissolved Organic Matter in the Estuarine Waters of Georgia, USA. Geochimica et Cosmochimica Acta 62: 473–483. doi:10.1016/S0016-7037(97)00363-3.

Cai, W.-J., Hu, X., Huang, W.-J., Jiang, L.-Q., Wang, Y., Peng, T.-H., Zhang, X., 2010. Alkalinity distribution in the western North Atlantic Ocean margins. J. Geophys. Res. 115, C08014. https://doi.org/10.1029/2009JC005482

Cai, W.-J., X. Hu, W.-J. Huang, and others. 2011. Acidification of subsurface coastal waters enhanced by eutrophication. Nature Geosci 4: 766–770. doi:10.1038/ngeo1297

Cai, W.-J., W.-J. Huang, G. W. Luther, and others. 2017. Redox reactions and weak buffering capacity lead to acidification in the Chesapeake Bay. Nature Communications 8: 369. doi:10.1038/s41467-017-00417-7.

Cai, W.-J., R. A. Feely, J. M. Testa, and others. 2020. Natural and Anthropogenic Drivers of Acidification in Large Estuaries. Annu. Rev. Mar. Sci. doi:10.1146/annurev-marine-010419-011004.

Caldeira, K., and M. E. Wickett. 2003. Anthropogenic carbon and ocean pH. Nature 425: 365–365. doi:10.1038/425365a.

Carter, B. R., N. L. Williams, A. R. Gray, and R. A. Feely. 2016. Locally interpolated alkalinity regression for global alkalinity estimation. Limnol. Oceanogr. Methods **14**: 268–277. doi:10.1002/lom3.10087.

Chen, C.-T.A., Wang, S.-L., 1999. Carbon, alkalinity and nutrient budgets on the East China Sea continental shelf. Journal of Geophysical Research: Oceans 104, 20675–20686. https://doi.org/10.1029/1999JC900055

Chipman, D.W., Sutherland, S.C., Takahashi, T., 1995. Determination of ocean/atmosphere carbon dioxide flux within the OMP study area. Final Technical Report for Grant DE-FG02-92ER61451, Lamont–Doherty Observatory of Columbia University, 16 pp.

Claret, M., E. D. Galbraith, J. B. Palter, D. Bianchi, K. Fennel, D. Gilbert, and J. P. Dunne. 2018. Rapid coastal deoxygenation due to ocean circulation shift in the northwest Atlantic. Nature Climate Change 8: 868–872. doi:10.1038/s41558-018-0263-1.

COMNARE (NH Coastal Marine Natural Resources & Environment Commission). 2017. 2017 Annual Report - Ocean Acidification summary and recommendations.

Cole, J.J., Caraco, N. and G. Kling. 1994. Carbon dioxide supersaturation in the surface waters of lakes. Science 265: 1568-1570.

Cook, Salme, "EFFECTS OF WAVES, TIDES, AND VEGETATION ON THE DISTRIBUTION OF BED SHEAR STRESS IN THE GREAT BAY ESTUARY, NH" (2019). Doctoral Dissertations. 2485. https://scholars.unh.edu/dissertation/2485

Cronan, C. S., and G. R. Aiken. 1985. Chemistry and transport of soluble humic substances in forested watersheds of the Adirondack Park, New York. Geochimica et Cosmochimica Acta 49: 1697–1705. doi:10.1016/0016-7037(85)90140-1

Cross, J.N., Mathis, J.T., Bates, N.R., Byrne, R.H., 2013. Conservative and non-conservative variations of total alkalinity on the southeastern Bering Sea shelf. Marine Chemistry 154, 100–112. https://doi.org/10.1016/j.marchem.2013.05.012

DeGrandpre, M.D., Hammar, T.R., Wallace, D.W.R., Wirick, C.D., 1997. Simultaneous mooring-based measurements of seawater CO2 and O2 off Cape Hatteras, North Carolina. Limnology and Oceanography 42, 21–28. https://doi.org/10.4319/lo.1997.42.1.0021

DeGrandpre, M.D., Olbu, G.J., Beatty, C.M., Hammar, T.R., 2002. Air–sea CO2 fluxes on the US Middle Atlantic Bight. Deep Sea Research Part II: Topical Studies in Oceanography, Carbon Cycling and Biogeochemistry in the Northwest Atlantic Shel f Slope: Results of the Ocean Margins Program 49, 4355–4367. https://doi.org/10.1016/S0967-0645(02)00122-4

De Meo, O. 2011. Studies of net community productivity in a near-coastal temperate ecosystem. University of New Hampshire.

Dickson, A.G., 1981. An exact definition of total alkalinity and a procedure for the estimation of alkalinity and total inorganic carbon from titration data. Deep Sea Research Part A. Oceanographic Research Papers 28, 609–623. https://doi.org/10.1016/0198-0149(81)90121-7

Dickson, A. G. 1990. Thermodynamics of the dissociation of boric acid in synthetic seawater from 273.15 to 318.15 K. Deep Sea Research Part A. Oceanographic Research Papers 37: 755–766. doi:10.1016/0198-0149(90)90004-F.

Dickson, A. G., D. J. Wesolowski, D. A. Palmer, and R. E. Mesmer. 1990. Dissociation constant of bisulfate ion in aqueous sodium chloride solutions to 250.degree.C. J. Phys. Chem. 94: 7978–7985. doi:10.1021/j100383a042

Dickson, A.G., Afghan, J.D., Anderson, G.C., 2003. Reference materials for oceanic CO2 analysis: a method for the certification of total alkalinity. Marine Chemistry 80, 185–197. https://doi.org/10.1016/S0304-4203(02)00133-0

Dickson, A.G., Sabine, C.L. and Christian, J.R. (Eds.) 2007. Guide to Best Practices for Ocean CO_2 Measurements. PICES Special Publication 3, 191 pp.

Dinauer, A., and A. Mucci. 2017. Spatial variability in surface-water pCO2 and gas exchange in the world's largest semi-enclosed estuarine system: St. Lawrence Estuary (Canada). Biogeosciences 14: 3221–3237. doi:https://doi.org/10.5194/bg-14-3221-2017

Dinauer, A., and A. Mucci. 2018. Distinguishing between physical and biological controls on the spatial variability of pCO2: A novel approach using OMP water mass analysis (St. Lawrence, Canada),. Marine Chemistry 204: 107–120.

Doney, S. C., V. J. Fabry, R. A. Feely, and J. A. Kleypas. 2009. Ocean Acidification: The Other CO2 Problem. Annual Review of Marine Science 1: 169–192. doi:10.1146/annurev.marine.010908.163834.

Doney, S.C., Ruckelshaus, M., Emmett Duffy, J., Barry, J.P., Chan, F., English, C.A., Galindo, H.M., Grebmeier, J.M., Hollowed, A.B., Knowlton, N., Polovina, J., Rabalais, N.N., Sydeman, W.J., Talley, L.D., 2011. Climate Change Impacts on Marine Ecosystems. Annu. Rev. Mar. Sci. 4, 11–37. https://doi.org/10.1146/annurev-marine-041911-111611

Douglas, N. K., and R. H. Byrne. 2017. Spectrophotometric pH measurements from river to sea: Calibration of mCP for 0≤S≤40 and 278.15≤T≤308.15K. Marine Chemistry 197: 64–69. doi:10.1016/j.marchem.2017.10.001

Drever, J. I. 1997. The Geochemistry of Natural Waters: Surface and Groundwater Environments, Prentice Hall.

Dupont, F., Hannah, C.G., Wright, D.G., 2006. Model investigation of the Slope Water, north of the Gulf Stream. Geophysical Research Letters 33. https://doi.org/10.1029/2005GL025321

Easley, R. A., and R. H. Byrne. 2012. Spectrophotometric Calibration of pH Electrodes in Seawater Using Purified m-Cresol Purple. Environ Sci Technol 46: 5018–5024. doi:10.1021/es300491s

Egleston, E. S., C. L. Sabine, and F. M. M. Morel. 2010. Revelle revisited: Buffer factors that quantify the response of ocean chemistry to changes in DIC and alkalinity. Global Biogeochemical Cycles 24. doi:10.1029/2008GB003407 Gran, G. 1952. Determination of the equivalence point in potentiometric titrations. Part II. Analyst 77: 661–671. doi:10.1039/AN9527700661.

Eshleman, K. N., and H. F. Hemond. 1985. The Role of Organic Acids in the Acid-Base Status of Surface Waters at Bickford Watershed, Massachusetts. Water Resources Research 21: 1503–1510. doi:https://doi.org/10.1029/WR021i010p01503

Faber, P. A., V. Evrard, R. J. Woodland, I. C. Cartwright, and P. L. M. Cook. 2014. Pore-water exchange driven by tidal pumping causes alkalinity export in two intertidal inlets. Limnol. Oceanogr. 59: 1749–1763. doi:10.4319/lo.2014.59.5.1749.

Fassbender, A. J., S. R. Alin, R. A. Feely, A. J. Sutton, J. A. Newton, and R. H. Byrne. 2017. Estimating Total Alkalinity in the Washington State Coastal Zone: Complexities and Surprising Utility for Ocean Acidification Research. Estuaries and Coasts **40**: 404–418. doi:10.1007/s12237-016-0168-z.

Feely, R.A., Sabine, C.L., Lee, K., Berelson, W., Kleypas, J., Fabry, V.J., Millero, F.J., 2004. Impact of Anthropogenic CO2 on the CaCO3 System in the Oceans. Science 305, 362–366. https://doi.org/10.1126/science.1097329

Fine, R.A., Willey, D.A., Millero, F.J., 2017. Global variability and changes in ocean total alkalinity from Aquarius satellite data. Geophysical Research Letters 44, 261–267. https://doi.org/10.1002/2016GL071712

Fong, M.B., Dickson, A.G., 2019. Insights from GO-SHIP hydrography data into the thermodynamic consistency of CO2 system measurements in seawater. Marine Chemistry 211, 52–63. https://doi.org/10.1016/j.marchem.2019.03.006

Friedlingstein, P., Jones, M.W., O'Sullivan, M., Andrew, R.M., Hauck, J., Peters, G.P., Peters, W., Pongratz, J., Sitch, S., Quéré, C.L., Bakker, D.C.E., Canadell, J.G., Ciais, P., Jackson, R.B., Anthoni, P., Barbero, L., Bastos, A., Bastrikov, V., Becker, M., Bopp, L., Buitenhuis, E., Chandra, N., Chevallier, F., Chini, L.P., Currie, K.I., Feely, R.A., Gehlen, M., Gilfillan, D., Gkritzalis, T., Goll, D.S., Gruber, N., Gutekunst, S., Harris, I., Haverd, V., Houghton, R.A., Hurtt, G., Ilyina, T., Jain, A.K., Joetzjer, E., Kaplan, J.O., Kato, E., Klein Goldewijk, K., Korsbakken, J.I., Landschützer, P., Lauvset, S.K., Lefèvre, N., Lenton, A., Lienert, S., Lombardozzi, D., Marland, G., McGuire, P.C., Melton, J.R., Metzl, N., Munro, D.R., Nabel, J.E.M.S., Nakaoka, S.-I., Neill, C., Omar, A.M., Ono, T., Peregon, A., Pierrot, D., Poulter, B., Rehder, G., Resplandy, L., Robertson, E., Rödenbeck, C., Séférian, R., Schwinger, J., Smith, N., Tans, P.P., Tian, H., Tilbrook, B., Tubiello, F.N., Werf, G.R. van der, Wiltshire, A.J., Zaehle, S., 2019. Global Carbon

Budget 2019. Earth System Science Data 11, 1783–1838. https://doi.org/10.5194/essd-11-1783-2019

Friis, K., A. Körtzinger, and D. W. R. Wallace. 2003. The salinity normalization of marine inorganic carbon chemistry data. Geophys. Res. Lett. 30: 1085. doi:10.1029/2002GL015898.

Fry, C.H., Tyrrell, T., Hain, M.P., Bates, N.R., Achterberg, E.P., 2015. Analysis of global surface ocean alkalinity to determine controlling processes. Marine Chemistry 174, 46–57. https://doi.org/10.1016/j.marchem.2015.05.003

Gattuso, J.-P., M. Frankignoulle, and R. Wollast. 1998. Carbon and Carbonate Metabolism in Coastal Aquatic Ecosystems. Annual Review of Ecology and Systematics 29: 405–434. doi:10.1146/annurev.ecolsys.29.1.405.

Gledhill, D., M. White, J. Salisbury, and others. 2015. Ocean and Coastal Acidification off New England and Nova Scotia. Oceanography 25: 182–197. doi:10.5670/oceanog.2015.41.

Gran, G. 1952. Determination of the equivalence point in potentiometric titrations. Part II. Analyst 77: 661–671. doi:10.1039/AN9527700661

Grodsky, S.A., Vandemark, D., Feng, H., Levin, J., 2018. Satellite detection of an unusual intrusion of salty slope water into a marginal sea: Using SMAP to monitor Gulf of Maine inflows. Remote Sensing of Environment 217, 550–561. https://doi.org/10.1016/j.rse.2018.09.004

Hagens, M., Slomp, C.P., Meysman, F.J.R., Seitaj, D., Harlay, J., Borges, A.V., Middelburg, J.J., 2015. Biogeochemical processes and buffering capacity concurrently affect acidification in a seasonally hypoxic coastal marine basin. Biogeosciences 12, 1561–1583. https://doi.org/10.5194/bg-12-1561-2015

Hammer, K., B. Schneider, K. Kuliński, and D. E. Schulz-Bull. 2017. Acid-base properties of Baltic Sea dissolved organic matter. Journal of Marine Systems 173: 114–121. doi:10.1016/j.jmarsys.2017.04.007

Hare, J.A., Cowen, R.K., 1996. Transport mechanisms of larval and pelagic juvenile bluefish (Pomatomus saltatrix) from South Atlantic Bight spawning grounds to Middle Atlantic Bight nursery habitats. Limnology and Oceanography 41, 1264–1280. https://doi.org/10.4319/lo.1996.41.6.1264

Harlay, J., Borges, A.V., Van Der Zee, C., Delille, B., Godoi, R.H.M., Schiettecatte, L.-S., Roevros, N., Aerts, K., Lapernat, P.-E., Rebreanu, L., Groom, S., Daro, M.-H., Van Grieken, R., Chou, L., 2010. Biogeochemical study of a coccolithophore bloom in the northern Bay of Biscay (NE Atlantic Ocean) in June 2004. Progress in Oceanography 86, 317–336. https://doi.org/10.1016/j.pocean.2010.04.029

Hernández-Ayon, J. M., A. Zirino, A. G. Dickson, T. Camiro-Vargas, and E. Valenzuela-Espinoza. 2007. Estimating the contribution of organic bases from microalgae to the titration alkalinity in coastal seawaters. Limnology and Oceanography: Methods 5: 225–232. doi:10.4319/lom.2007.5.225

Hinckley, J. A. 2021. The non-conservative behavior of organic alkalinity in U.S. and Canadian estuaries of the Gulf of Maine. University of New Hampshire.

Hofmann, E., Druon, J.-N., Fennel, K., Friedrichs, M., Haidvogel, D., Lee, C., Mannino, A., McClain, C., Najjar, R., O'Reilly, J., Pollard, D., Previdi, M., Seitzinger, S., Siewert, J., Signorini, S., Wilkin, J., 2008. Eastern US Continental Shelf Carbon Budget: Integrating Models, Data Assimilation, and Analysis. Oceanography 21, 86–104. https://doi.org/10.5670/oceanog.2008.70

Hopkinson, C. S., A. E. Giblin, J. Tucker, and R. H. Garritt. 1999. Benthic metabolism and nutrient cycling along an estuarine salinity gradient. Estuaries 22: 863–881. doi:10.2307/1353067

Howland, R. J., A. D. Tappin, R. J. Uncles, D. H. Plummer, and N. J. Bloomer. 2000. Distributions and seasonal variability of pH and alkalinity in the Tweed Estuary, UK. Sci Total Environ 251–252: 125–138. doi:10.1016/s0048-9697(00)00406-x.

Hunt, C. W., J. E. Salisbury, D. Vandemark, and W. McGillis. 2011a. Contrasting Carbon Dioxide Inputs and Exchange in Three Adjacent New England Estuaries. Estuaries and Coasts 34: 68–77. doi:10.1007/s12237-010-9299-9

Hunt, C.W., Salisbury, J.E., Vandemark, D., 2011b. Contribution of non-carbonate anions to total alkalinity and overestimation of pCO2 in New England and New Brunswick rivers. Biogeosciences 8, 3069–3076. https://doi.org/10.5194/bg-8-3069-2011

Hunt, C. W., J. E. Salisbury, and D. Vandemark. 2013. CO2 Input Dynamics and Air–Sea Exchange in a Large New England Estuary. Estuaries and Coasts 37: 1078–1091. doi:10.1007/s12237-013-9749-2.

Hunt, C. W., J. E. Salisbury, D. Vandemark, S. Aßmann, P. Fietzek, C. Melrose, R. Wanninkhof, and K. Azetsu-Scott. 2021. Variability of USA East Coast surface total alkalinity distributions revealed by automated instrument measurements. Marine Chemistry 232: 103960. doi:10.1016/j.marchem.2021.103960

(ILO-SLRB) International Lake Ontario-St. Lawrence River Board. 2018. Lake Ontario - St. Lawrence River 2017 High Water - Questions and Answers. International Joint Commission. https://ijc.org/en/loslrb/watershed/faq/2017. Accessed 10/5/2020.

IPCC. 2014. Climate Change 2014: Synthesis Report. Contribution of Working Groups I, II and III to the Fifth Assessment Report of the Intergovernmental Panel on Climate Change [Core Writing Team, R.K. Pachauri and L.A. Meyer (eds.)]. IPCC, Geneva, Switzerland, 151 pp.

Jiang, Z.-P., Tyrrell, T., Hydes, D.J., Dai, M., Hartman, S.E., 2014. Variability of alkalinity and the alkalinity-salinity relationship in the tropical and subtropical surface ocean. Global Biogeochemical Cycles 28, 729–742. https://doi.org/10.1002/2013GB004678

Joesoef, A., Kirchman, D.L., Sommerfield, C.K., Cai, W.-J., 2017. Seasonal variability of the inorganic carbon system in a large coastal plain estuary. Biogeosciences 14, 4949–4963. https://doi.org/10.5194/bg-14-4949-2017

Jones, S.H. 2000. A Technical Characterization of Estuarine and Coastal New Hampshire. Portsmouth NH: New Hampshire Estuaries Project.

Jutras, M., C. O. Dufour, A. Mucci, F. Cyr, and D. Gilbert. 2020. Temporal Changes in the Causes of the Observed Oxygen Decline in the St. Lawrence Estuary. Journal of Geophysical Research: Oceans 125: e2020JC016577. doi:https://doi.org/10.1029/2020JC016577

Kaushal, S. S., G. E. Likens, R. M. Utz, M. L. Pace, M. Grese, and M. Yepsen. 2013. Increased River Alkalinization in the Eastern U.S. Environ. Sci. Technol. 47: 10302–10311. doi:10.1021/es401046s.

Kaushal, S. S., P. M. Mayer, P. G. Vidon, and others. 2014. Land Use and Climate Variability Amplify Carbon, Nutrient, and Contaminant Pulses: A Review with Management Implications. J Am Water Resour Assoc 50: 585–614. doi:10.1111/jawr.12204.

Keller, J. 2020. Taking stock of a Downeast river. Island Institute. http://www.islandinstitute.org/working-waterfront/taking-stock-downeast-river. Accessed 2020-03-05 21:08:49.

Key, R.M., A. Olsen, S. van Heuven, S. K. Lauvset, A. Velo, X. Lin, C. Schirnick, A. Kozyr, T. Tanhua, M. Hoppema, S. Jutterström, R. Steinfeldt, E. Jeansson, M. Ishi, F. F. Perez, and T. Suzuki. 2015. Global Ocean Data Analysis Project, Version 2 (GLODAPv2), ORNL/CDIAC-162, ND-P093. Carbon Dioxide Information Analysis Center, Oak Ridge National Laboratory, US Department of Energy, Oak Ridge, Tennessee. doi:10.3334/CDIAC/OTG.NDP093_GLODAPv2.

Ko, Y. H., Lee, K., Eom, K. H. and I.-S. Han. 2016. Organic alkalinity produced by phytoplankton and its effect on the computation of ocean carbon parameters. Limnol. Oceanogr. doi:10.1002/lno.10309.

Köster, M., H.-D. Babenzien, H. J. Black, and others. 2000. Significance of aerobic and anaerobic mineralization processes of organic carbon in sediments of a shallow coastal inlet in the southern Baltic Sea, p. 185–194. In B.W. Flemming, M.T. Delafontaine, and G. Liebezeit [eds.], Proceedings in Marine Science. Elsevier.

Krumins, V., M. Gehlen, S. Arndt, P. V. Cappellen, and P. Regnier. 2013. Dissolved inorganic carbon and alkalinity fluxes from coastal marine sediments: model estimates for different shelf environments and sensitivity to global change. Biogeosciences 10: 371–398. doi:https://doi.org/10.5194/bg-10-371-2013.

Kuliński, K., Schneider, B., Hammer, K., Machulik, U., Schulz-Bull, D., 2014. The influence of dissolved organic matter on the acid–base system of the Baltic Sea. Journal of Marine Systems 132, 106–115. https://doi.org/10.1016/j.jmarsys.2014.01.011

Land, P.E., Findlay, H.S., Shutler, J.D., Ashton, I.G.C., Holding, T., Grouazel, A., Girard-Ardhuin, F., Reul, N., Piolle, J.-F., Chapron, B., Quilfen, Y., Bellerby, R.G.J., Bhadury, P., Salisbury, J., Vandemark, D., Sabia, R., 2019. Optimum satellite remote sensing of the marine carbonate system using empirical algorithms in the global ocean, the Greater Caribbean, the Amazon Plume and the Bay of Bengal. Remote Sensing of Environment 235, 111469. https://doi.org/10.1016/j.rse.2019.111469

Lavigne, H., Epitalon, J.-M. and J.-P. Gattuso. 2011. seacarb: seawater carbonate chemistry with R. R package version 3.0. http://CRAN.R-project.org/package=seacarb

Le Quéré, C. L., R. M. Andrew, J. G. Canadell, and others. 2016. Global Carbon Budget 2016. Earth System Science Data **8**: 605–649. doi:10.5194/essd-8-605-2016.

Lee, K., Tong, L.T., Millero, F.J., Sabine, C.L., Dickson, A.G., Goyet, C., Park, G.-H., Wanninkhof, R., Feely, R.A., Key, R.M., 2006. Global relationships of total alkalinity with salinity and temperature in surface waters of the world's oceans. Geophysical Research Letters 33. https://doi.org/10.1029/2006GL027207

Lee, D. Y., M. S. Owens, M. Doherty, E. M. Eggleston, I. Hewson, B. C. Crump, and J. C. Cornwell. 2015. The Effects of Oxygen Transition on Community Respiration and Potential Chemoautotrophic Production in a Seasonally Stratified Anoxic Estuary. Estuaries and Coasts 38: 104–117. doi:10.1007/s12237-014-9803-8.

Lewis, E. and Wallace, D. W. R.: Program developed for CO2 system calculations, Carbon Dioxide Information Analysis Center, Report ORNL/CDIAC-105, Oak Ridge National Laboratory, Oak Ridge, Tennessee, USA, 1998.

Leopold, A., C. Marchand, J. Deborde, and M. Allenbach. 2016. Water Biogeochemistry of a Mangrove-Dominated Estuary Under a Semi-Arid Climate (New Caledonia). Estuaries and Coasts 1–19. doi:10.1007/s12237-016-0179-9.

Li, Q., Wang, F., Wang, Z.A., Yuan, D., Dai, M., Chen, J., Dai, J., Hoering, K.A., 2013. Automated Spectrophotometric Analyzer for Rapid Single-Point Titration of Seawater Total Alkalinity. Environ. Sci. Technol. 47, 11139–11146. https://doi.org/10.1021/es402421a

Li, X., Bellerby, R.G.J., Wallhead, P., Ge, J., Liu, Jie, Liu, Jing, Yang, A., 2020. A Neural Network-Based Analysis of the Seasonal Variability of Surface Total Alkalinity on the East China Sea Shelf. Front. Mar. Sci. 7. https://doi.org/10.3389/fmars.2020.00219

Liu, X., M. C. Patsavas, and R. H. Byrne. 2011. Purification and Characterization of meta-Cresol Purple for Spectrophotometric Seawater pH Measurements. Environ. Sci. Technol. 45: 4862–4868. doi:10.1021/es200665d

Loder, J. W. 1998. The coastal ocean off northeastern North America : a large-scale view. The Sea 11: 105–138.

Lozovik, P. A. 2005. Contribution of Organic Acid Anions to the Alkalinity of Natural Humic Water. J Anal Chem 60: 1000–1004. doi:10.1007/s10809-005-0226-3

Martell-Bonet, L., and R. H. Byrne. 2020. Characterization of the nonlinear salinity dependence of glass pH electrodes: A simplified spectrophotometric calibration procedure for potentiometric seawater pH measurements at 25 °C in marine and brackish waters: 0.5 ≤ S ≤ 36. Marine Chemistry **220**: 103764. doi:10.1016/j.marchem.2020.103764

Mathis, J., Cross, J., Evans, W., Doney, S., 2015. Ocean Acidification in the Surface Waters of the Pacific-Arctic Boundary Regions. Oceanography 25, 122–135. https://doi.org/10.5670/oceanog.2015.36

Matso, Kalle, "Flushing Time Versus Residence Time for the Great Bay Estuary" (2018). PREP Reports & Publications. 413. dence Time for the Great Bay Estuary" (2018). https://scholars.unh.edu/prep/413.

McDonald, C.P., Stets, E.G., Striegl, R.G. and D. Butman. 2013. Inorganic carbon loading as a primary driver of dissolved carbon dioxide concentrations in the lakes and reservoirs of the contiguous United States. Global Biogeochemical Cycles 27: 285-295.

Middelburg, J. J., K. Soetaert, and M. Hagens. 2020. Ocean Alkalinity, Buffering and Biogeochemical Processes. Reviews of Geophysics 58: e2019RG000681. doi:10.1029/2019RG000681.

Millero, F.J., Lee, K., Roche, M., 1998. Distribution of alkalinity in the surface waters of the major oceans. Marine Chemistry 60, 111–130. https://doi.org/10.1016/S0304-4203(97)00084-4

Mitchell, P. H., and J. L. Solinger. 1934. The Effects of Land Drainage upon the Excess Bases of Sea Water. Biological Bulletin **66**: 97–101. doi:10.2307/1537323.

MSLCOOA, Massachusetts Special Legislative Commission on Ocean Acidification. 2021. Report on the ocean acidification crisis in Massachusetts.

Mucci, A., M. Starr, D. Gilbert, and B. Sundby. 2011. Acidification of Lower St. Lawrence Estuary Bottom Waters. Atmosphere-Ocean 49: 206–218. doi:10.1080/07055900.2011.599265

Najjar, R. G., M. Herrmann, S. M. C. D. Valle, and others. 2020. Alkalinity in Tidal Tributaries of the Chesapeake Bay. Journal of Geophysical Research: Oceans 125: e2019JC015597. doi:10.1029/2019JC015597.

NERR 2021. National Estuarine Research Reserve, Central.ized Data Management Office. Accessed April 21, 2021, https://cdmo.baruch.sc.edu/dges/

Nixon, S. W. 1995. Coastal marine eutrophication: A definition, social causes, and future concerns. Ophelia **41**: 199–219. doi:10.1080/00785236.1995.10422044

Nixon, S. W., A. J. Oczkowski, M. E. Q. Pilson, L. Fields, C. A. Oviatt, and C. W. Hunt. 2015. On the Response of pH to Inorganic Nutrient Enrichment in Well-Mixed Coastal Marine Waters. Estuaries and Coasts 38: 232–241. doi:10.1007/s12237-014-9805-6.

Oliver, B. G., E. M. Thurman, and R. L. Malcolm. 1983. The contribution of humic substances to the acidity of colored natural waters. Geochimica et Cosmochimica Acta 47: 2031–2035. doi:10.1016/0016-7037(83)90218-1

Orr, J. C., V. J. Fabry, O. Aumont, and others. 2005. Anthropogenic ocean acidification over the twenty-first century and its impact on calcifying organisms. Nature 437: 681–686. doi:10.1038/nature04095.

Ohashi, K., and J. Sheng. 2013. Influence of St. Lawrence River discharge on the circulation and hydrography in Canadian Atlantic waters. Continental Shelf Research 58: 32–49. doi:https://doi.org/10.1016/j.csr.2013.03.005.

Olsen, A., Key, R.M., Heuven, S. van, Lauvset, S.K., Velo, A., Lin, X., Schirnick, C., Kozyr, A., Tanhua, T., Hoppema, M., Jutterström, S., Steinfeldt, R., Jeansson, E., Ishii, M., Pérez, F.F., Suzuki, T., 2016. The Global Ocean Data Analysis Project version 2 (GLODAPv2) – an internally consistent data product for the world ocean. Earth System Science Data 8, 297–323. https://doi.org/10.5194/essd-8-297-2016

Pacella, S. R., C. A. Brown, G. G. Waldbusser, R. G. Labiosa, and B. Hales. 2018. Seagrass habitat metabolism increases short-term extremes and long-term offset of

CO2 under future ocean acidification. PNAS 115: 3870–3875. doi:10.1073/pnas.1703445115.

Park, P.K. 1960. Oceanic CO2 System: An Evaluation of Ten Methods of Investigation. Limnology and Oceanography 14(2): 179-186.

Paxéus, N., and M. Wedborg. 1985. Acid-base properties of aquatic fulvic acid. Analytica Chimica Acta 169: 87–98. doi:10.1016/S0003-2670(00)86210-8

Pershing, A. J., M. A. Alexander, C. M. Hernandez, and others. 2015. Slow adaptation in the face of rapid warming leads to collapse of the Gulf of Maine cod fishery. Science 350: 809–812. doi:10.1126/science.aac9819.

Pershing, A., A. Dayton, B. Franklin, and B. Kennedy. 2018. Evidence for Adaptation from the 2016 Marine Heatwave in the Northwest Atlantic Ocean. Oceanog 31. doi:10.5670/oceanog.2018.213.

Pierrot, D., Neill, C., Sullivan, K., Castle, R., Wanninkhof, R., Lüger, H., Johannessen, T., Olsen, A., Feely, R.A., Cosca, C.E., 2009. Recommendations for autonomous underway pCO2 measuring systems and data-reduction routines. Deep Sea Research Part II: Topical Studies in Oceanography, Surface Ocean CO2 Variability and Vulnerabilities 56, 512–522. https://doi.org/10.1016/j.dsr2.2008.12.005

PREP (Piscataqua Region Estuaries Partnership), "State of Our Estuaries Report 2018" (2017). PREP Reports & Publications. 391.

Rasmussen, L.L., Gawarkiewicz, G., Owens, W.B., Lozier, M.S., 2005. Slope water, Gulf Stream, and seasonal influences on southern Mid-Atlantic Bight circulation during

the fall-winter transition. Journal of Geophysical Research: Oceans 110. https://doi.org/10.1029/2004JC002311

Raymond, P. A., J. E. Bauer, and J. J. Cole. 2000. Atmospheric CO2 evasion, dissolved inorganic carbon production, and net heterotrophy in the York River estuary. Limnol. Oceanogr. 45: 1707–1717. doi:10.4319/lo.2000.45.8.1707.

Raymond, P. A., and J. J. Cole. 2001. Gas Exchange in Rivers and Estuaries: Choosing a Gas Transfer Velocity. Estuaries 24: 312–317. doi:10.2307/1352954

Raymond, P.A., Hartmann, J., Lauerwald, R., Sobek, S., Hoover, M., Butman, D., Striegl, R., Mayorga, E., Humborg, C., Kortelainen, P., Durr, H., Meybeck, M., Ciais, P. and P. Guth. 2013. Global carbon dioxide emissions from inland waters. Nature 503: 355-359.

Renforth, P. 2017. Preventing climate change by increasing ocean alkalinity. Eos 98, https://doi.org/10.1029/2018EO076919. Published on 09 August 2017.

Reul, N., Grodsky, S.A., Arias, M., Boutin, J., Catany, R., Chapron, B., D'Amico, F., Dinnat, E., Donlon, C., Fore, A., Fournier, S., Guimbard, S., Hasson, A., Kolodziejczyk, N., Lagerloef, G., Lee, T., Le Vine, D.M., Lindstrom, E., Maes, C., Mecklenburg, S., Meissner, T., Olmedo, E., Sabia, R., Tenerelli, J., Thouvenin-Masson, C., Turiel, A., Vergely, J.L., Vinogradova, N., Wentz, F., Yueh, S., 2020. Sea surface salinity estimates from spaceborne L-band radiometers: An overview of the first decade of observation (2010–2019). Remote Sensing of Environment 242, 111769. https://doi.org/10.1016/j.rse.2020.111769

Salisbury, J., Green, M., Hunt, C., Campbell, J., 2008. Coastal Acidification by Rivers:A Threat to Shellfish? Eos Trans. AGU 89, 513–513. https://doi.org/10.1029/2008EO500001

Salisbury, J., D. Vandemark, C. Hunt, J. Campbell, B. Jonsson, A. Mahadevan, W. McGillis, and H. Xue. 2009. Episodic riverine influence on surface DIC in the coastal Gulf of Maine. Estuarine, Coastal and Shelf Science 82: 108–118. doi:10.1016/j.ecss.2008.12.021.

Salisbury, J., Vandemark, D., Jönsson, B., Balch, W., Chakraborty, S., Lohrenz, S., Chapron, B., Hales, B., Mannino, A., Mathis, J., Reul, N., Signorini, S., Wanninkhof, R., Yates, K., 2015. How Can Present and Future Satellite Missions Support Scientific Studies that Address Ocean Acidification? Oceanography 25, 108–121. https://doi.org/10.5670/oceanog.2015.35

Salisbury, J.E., Jönsson, B.F., 2018. Rapid warming and salinity changes in the Gulf of Maine alter surface ocean carbonate parameters and hide ocean acidification. Biogeochemistry 141, 401–418. https://doi.org/10.1007/s10533-018-0505-3

Seelmann, K., Aßmann, S., Körtzinger, A., 2019. Characterization of a novel autonomous analyzer for seawater total alkalinity: Results from laboratory and field tests. Limnology and Oceanography: Methods 17, 515–532. https://doi.org/10.1002/lom3.10329

Sharp, J. D., and R. H. Byrne. 2020. Interpreting measurements of total alkalinity in marine and estuarine waters in the presence of proton-binding organic matter. Deep

Sea Research Part I: Oceanographic Research Papers 165: 103338. doi:10.1016/j.dsr.2020.103338

Sharp, J. D., and R. H. Byrne. 2021. Technical note: Excess alkalinity in carbonate system reference materials. Marine Chemistry 103965. doi:10.1016/j.marchem.2021.103965.

Sherwood, O. A., M. F. Lehmann, C. J. Schubert, D. B. Scott, and M. D. McCarthy. 2011. Nutrient regime shift in the western North Atlantic indicated by compound-specific δ15N of deep-sea gorgonian corals. PNAS 108: 1011–1015. doi:10.1073/pnas.1004904108

Short, F. T. 1992. The Ecology of the Great Bay Estuary, New Hampshire and Maine: An Estuarine Profile and Bibliography, Jackson Estuarine Laboratory, University of New Hampshire.

Signorini, S.R., Mannino, A., Najjar, R.G., Friedrichs, M.A.M., Cai, W.-J., Salisbury, J., Wang, Z.A., Thomas, H., Shadwick, E., 2013. Surface ocean pCO2 seasonality and sea-air CO2 flux estimates for the North American east coast. J. Geophys. Res. Oceans 118, 5439–5460. https://doi.org/10.1002/jgrc.20369

Sipos, P., May, P.M. and Hefter, G.T. 2000. Carbonate removal from concentrated hydroxide solutions. Analyst 125(5): 955-958.

Sippo, J. Z., D. T. Maher, D. R. Tait, C. Holloway, and I. R. Santos. 2016. Are mangroves drivers or buffers of coastal acidification? Insights from alkalinity and

dissolved inorganic carbon export estimates across a latitudinal transect. Global Biogeochem. Cycles 30: 2015GB005324. doi:10.1002/2015GB005324.

Song, S., Z. A. Wang, M. E. Gonneea, K. D. Kroeger, S. N. Chu, D. Li, and H. Liang. 2020. An important biogeochemical link between organic and inorganic carbon cycling: Effects of organic alkalinity on carbonate chemistry in coastal waters influenced by intertidal salt marshes. Geochimica et Cosmochimica Acta **275**: 123–139. doi:10.1016/j.gca.2020.02.013

Stumm, W., and Morgan, J.J. 1995. Wiley: Aquatic Chemistry: Chemical Equilibria and Rates in Natural Waters, 3rd Edition - Werner Stumm, James J. Morgan, Wiley.

Takahashi, T., Sutherland, S.C., Chipman, D.W., Goddard, J.G., Ho, C., Newberger, T., Sweeney, C., Munro, D.R., 2014. Climatological distributions of pH, pCO2, total CO2, alkalinity, and CaCO3 saturation in the global surface ocean, and temporal changes at selected locations. Marine Chemistry 164, 95–125. https://doi.org/10.1016/j.marchem.2014.06.004

Thomas, H., Schiettecatte, L.-S., Suykens, K., Koné, Y.J.M., Shadwick, E.H., Prowe, A.E.F., Bozec, Y., de Baar, H.J.W., Borges, A.V., 2009. Enhanced ocean carbon storage from anaerobic alkalinity generation in coastal sediments. Biogeosciences 6, 267–274. https://doi.org/10.5194/bg-6-267-2009

Thompson, T. G., and R. U. Bonnar. 1931. The buffer capacity of sea water. Ind. Eng. Chem. Anal. Ed. **3**: 393–395. doi:10.1021/ac50076a029.

Townsend, D.W., Thomas, A.C., Mayer, L.M., Thomas, M., Quinlan, J., 2006. Oceanography of the Northwest Atlantic Continental Shelf, in: The Sea. Harvard University Press, pp. 119–168.

Townsend, D. W., N. R. Pettigrew, M. A. Thomas, M. G. Neary, D. J. McGillicuddy, and J. O'Donnell. 2015. Water Masses and Nutrient Sources to the Gulf of Maine. Journal of marine research 73: 93–122. doi:10.1357/002224015815848811.

Ulfsbo, A., S. Hulth, and L. G. Anderson. 2011. pH and biogeochemical processes in the Gotland Basin of the Baltic Sea. Marine Chemistry 127: 20–30. doi:10.1016/j.marchem.2011.07.004.

Ulfsbo, A., K. Kuliński, L. G. Anderson, and D. R. Turner. 2015. Modelling organic alkalinity in the Baltic Sea using a Humic-Pitzer approach. Marine Chemistry **168**: 18–26. doi:10.1016/j.marchem.2014.10.013

Van Dam, B. R., C. Lopes, C. L. Osburn, and J. W. Fourqurean. 2019. Net heterotrophy and carbonate dissolution in two subtropical seagrass meadows. Biogeosciences 16: 4411–4428. doi:https://doi.org/10.5194/bg-16-4411-2019.

Van Dam, B. R., and H. Wang. 2019. Decadal-Scale Acidification Trends in Adjacent North Carolina Estuaries: Competing Role of Anthropogenic CO2 and Riverine Alkalinity Loads. Front. Mar. Sci. 6. doi:10.3389/fmars.2019.00136.

Van Heuven, S., Pierrot, D., Rae, J.W.B., Lewis, E., and Wallace, D. W. R. CO2SYS v 1.1, MATLAB program developed for CO2 system calculations. ORNL/CDIAC-105b. ORNL/CDIAC-105b Oak Ridge Natl. Lab. US DoE.

Vandemark, D., J. E. Salisbury, C. W. Hunt, S. M. Shellito, J. D. Irish, W. R. McGillis, C. L. Sabine, and S. M. Maenner. 2011. Temporal and spatial dynamics of CO2 air-sea flux in the Gulf of Maine. J. Geophys. Res. 116: C01012. doi:10.1029/2010JC006408.

Waldbusser, G. G., E. N. Powell, and R. Mann. 2013. Ecosystem effects of shell aggregations and cycling in coastal waters: an example of Chesapeake Bay oyster reefs. Ecology 94: 895–903. doi:10.1890/12-1179.1.

Waldbusser, G.G. and J.E. Salisbury. 2014. Ocean Acidification in the Coastal Zone from an Organism's Perspective: Multiple System Parameters, Frequency Domains,and Habitats. Annu. Rev. Mar. Sci. 6:221–47

Wallace, R.B., Baumann, H., Grear, J.S., Aller, R.C., Gobler, C.J., 2014. Coastal ocean acidification: The other eutrophication problem. Estuarine, Coastal and Shelf Science 148, 1–13. https://doi.org/10.1016/j.ecss.2014.05.027

Wang, Z. A., and W.-J. Cai. 2004. Carbon dioxide degassing and inorganic carbon export from a marsh-dominated estuary (the Duplin River): A marsh CO2 pump. Limnol. Oceanogr. 49: 341–354. doi:10.4319/lo.2004.49.2.0341.

Wang, Z.A., Wanninkhof, R., Cai, W.-J., Byrne, R.H., Hu, X., Peng, T.-H., Huang, W.-J., 2013. The marine inorganic carbon system along the Gulf of Mexico and Atlantic coasts of the United States: Insights from a transregional coastal carbon study. Limnol. Oceanogr. 58, 325–342. https://doi.org/10.4319/lo.2013.58.1.0325

Wang, Z.A., Kroeger, K.D., Ganju, N.K., Gonneea, M.E., Chu, S.N., 2016. Intertidal salt marshes as an important source of inorganic carbon to the coastal ocean. Limnol. Oceanogr. 61, 1916–1931. https://doi.org/10.1002/lno.10347

Wanninkhof, R., and K. Thoning. 1993. Measurement of fugacity of CO2 in surface water using continuous and discrete sampling methods. Marine Chemistry 44: 189–204. doi:10.1016/0304-4203(93)90202-Y.

Wanninkhof, R., Barbero, L., Byrne, R., Cai, W.-J., Huang, W.-J., Zhang, J.-Z., Baringer, M., Langdon, C., 2015. Ocean acidification along the Gulf Coast and East Coast of the USA. Continental Shelf Research 98, 54–71. https://doi.org/10.1016/j.csr.2015.02.008

Xu, Y.-Y., W.-J. Cai, Y. Gao, and others. 2017. Short-term variability of aragonite saturation state in the central Mid-Atlantic Bight. Journal of Geophysical Research: Oceans 122: 4274–4290. doi:10.1002/2017JC012901

Yang, B., Byrne, R.H., Lindemuth, M., 2015. Contributions of organic alkalinity to total alkalinity in coastal waters: A spectrophotometric approach. Marine Chemistry 176, 199–207. https://doi.org/10.1016/j.marchem.2015.09.008

Yao, W., Byrne, R.H., 1998. Simplified seawater alkalinity analysis. Deep Sea Research Part I: Oceanographic Research Papers 45, 1383–1392. https://doi.org/10.1016/S0967-0637(98)00018-1

Zeebe, R.E., 2012. History of Seawater Carbonate Chemistry, Atmospheric CO2, and Ocean Acidification. Annual Review of Earth and Planetary Sciences 40, 141–165. https://doi.org/10.1146/annurev-earth-042711-105521

Zweng, M.M, Reagan, J.R., Seidov, D., Boyer, T.P. , Locarnini, R.A., Garcia, H.E., Mishonov, A.V., Baranova, O.K., Weathers, K.W., Paver, C.R., Smolyar, I.V., 2019. World Ocean Atlas 2018, Volume 2: Salinity. A. Mishonov, Technical Editor, NOAA Atlas NESDIS 82, 50pp.

APPENDIX A

Statistical Calculation Detail

Precision was determined as one standard deviation (σ) of repeated measurements of certified reference material (CRM):

$$\sigma = \pm\sqrt{\frac{\sum_{i=1}^{n}(TA_i - \overline{TA})^2}{n-1}} \quad (1)$$

where *n* is the number of measurements, TA_i is the i[th] of n TA measurements, and $\overline{TA}$ is the mean of all TA measurements. Accuracy was determined at the root mean square error (RMSE) of repeated CRM measurements relative to the certified TA, or of the TA differences of paired samples measured by independent instruments such as laboratory titration systems:

$$RMSE = \pm\sqrt{\frac{1}{n}\sum_{i=1}^{n}(TA_{A,i} - TA_{B,i})^2} \quad (2)$$

where *n* is the total number of paired sample or CRM measurements, $TA_{A,i}$ is the i[th] TA measured by instrument A, and $TA_{B,i}$ is either the i[th] TA measured by instrument B or the CRM TA concentration. The RMSE and CRM uncertainty were then used to calculate a total bias uncertainty *u(bias)*:

$$u(bias) = \pm\sqrt{RMSE^2 + u(CRM)^2} \quad (3)$$

where *u(CRM)* is the uncertainty of the certified CRM TA concentration. Then *u(bias)* and *σ*, together with a *u(other)* term for non-CRM seawater samples, were combined into an overall uncertainty u_c (approximating a 68.3% confidence interval):

$$u_c = \pm\sqrt{\sigma^2 + u(bias)^2} \quad (4)$$

The combined known uncertainties between the HydroFIA TA measurements and discrete TA measurements, with uncertainties calculated from replicate bottle analyses can be propagated into a combined uncertainty- $u_{c(HydroFIA\ TA,B)}$- as:

$$u_{c(HydroFIA\,TA,B)} = \pm\sqrt{u_{c(HydroFIA\,TA)}{}^2 + u_{c(B)}{}^2 + u(rep) + u(other)} \quad (5)$$

where *u(rep)* is calculated from Equation 4 (substituting the calculated RMSE of replicate bottle samples for u_c and *u(rep)* for *u(bias)*. The *u(other)* term includes all potential non-instrumental uncertainties, including temporal offsets between sample collection and instrument measurement times, discrete sample preservation uncertainties, and other unknown uncertainties.

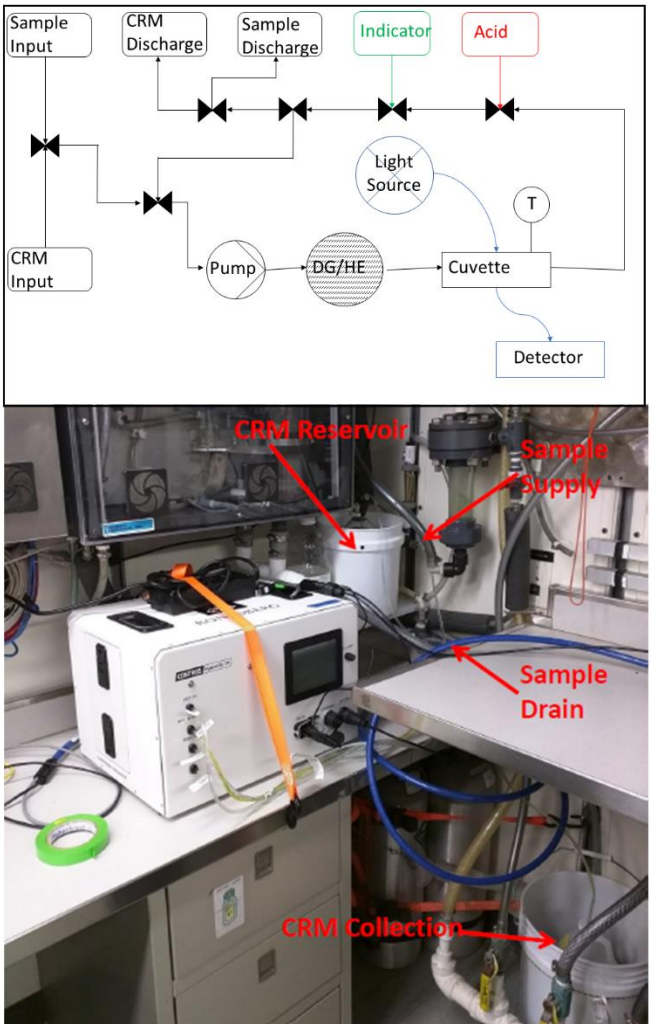

Figure A.1: Top panel: schematic diagram of HydroFIA TA instrument components as used in this work, including modifications for automated CRM measurements. Bottom panel: photograph of the HydroFIA TA analyzer, installed aboard the NOAA Ship *Henry B. Bigelow*.

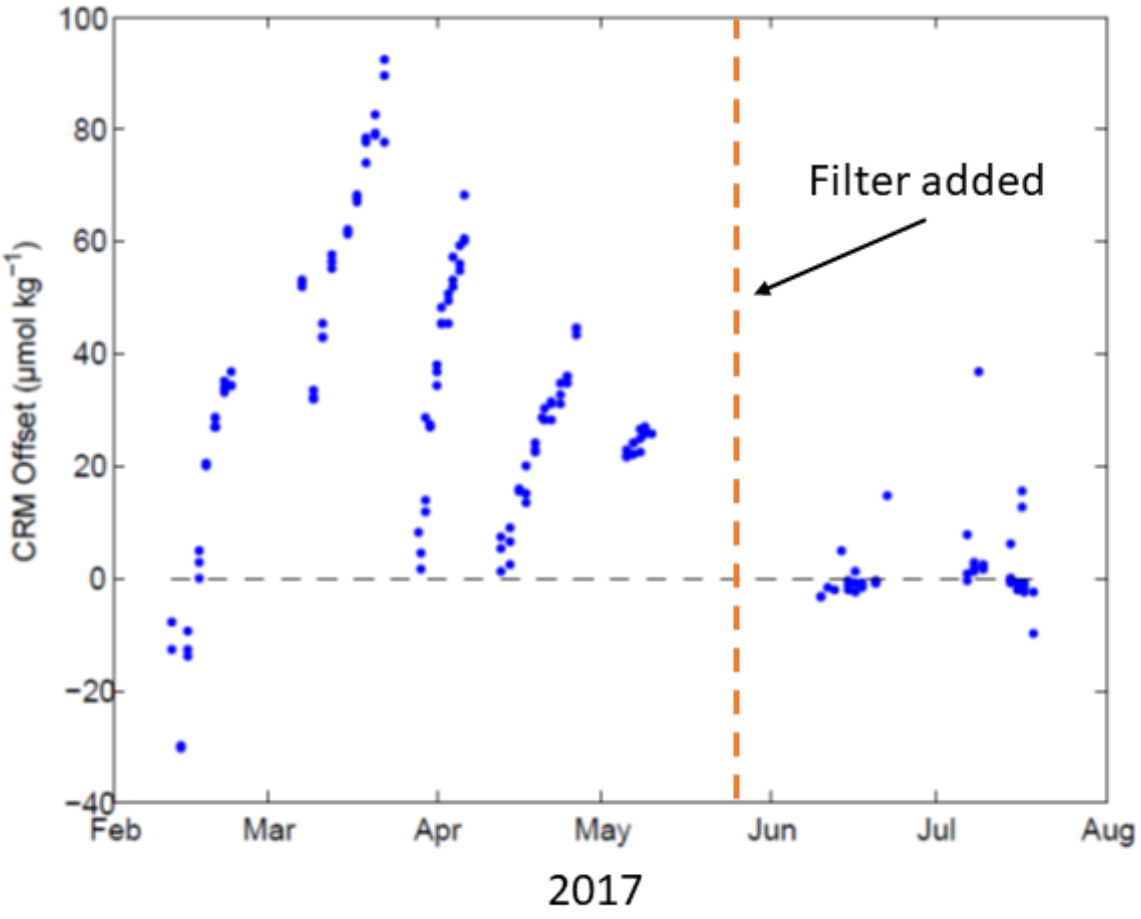

Figure A.2: Offsets of automated HydroFIA TA measurements of certified reference material (CRM) measured during the seven 2017 cruises. The offset was calculated as the certified TA concentration subtracted from the measured TA value, thus positive values indicate an overestimate of the CRM TA. The CRM used on 2017 cruises was Batch 159, with a certified TA concentration of 2213.59 µmol kg^{-1} (Dickson et al. 2003). The in-line filter described in the text was added in June with some sample offsets (i.e., noise) but no substantial drift observed after.

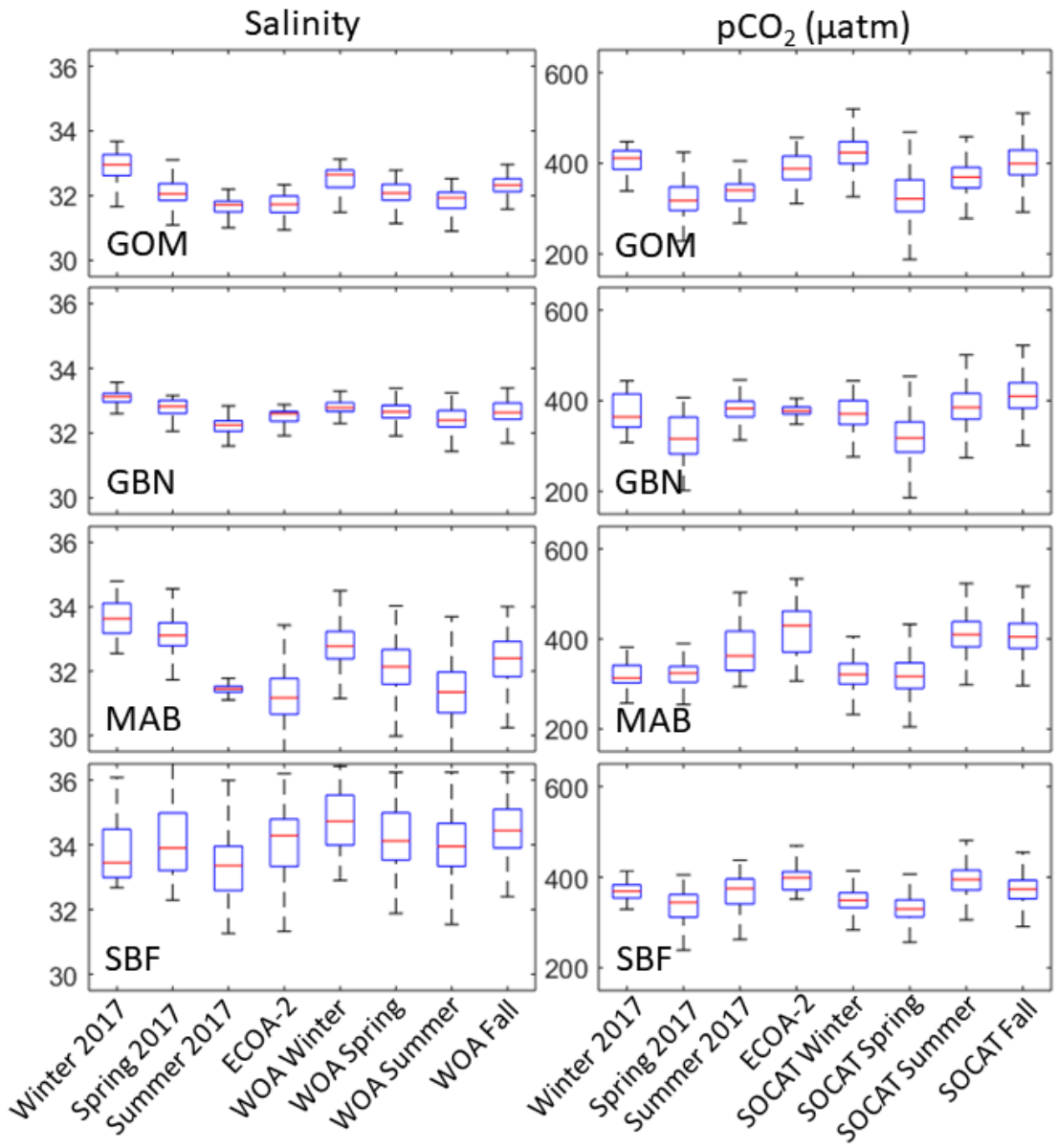

Figure A.3: Seasonal box-and-whisker plots of mean salinity (left panels) and mean pCO_2 (right panels, µatm). Red lines denote mean values, upper and lower box boundaries depict the 75th and 25th percentiles, respectively, and whiskers depict range of values. WOA and SOCAT datasets are described in the text.

	Dates	Minimum CRM Offset (µmol kg-1)	Maximum CRM Offset (µmol kg-1)	Mean CRM Offset (µmol kg-1)	σ (µmol kg-1)	n
Cruise 1	Feb 11 - Feb 22	-31	37	11	6.2	27
Cruise 2	Mar 7 - Mar 22	32	93	62	2.5	27
Cruise 3	Mar 28 - Apr 6	2	68	39	3.4	27
Cruise 4	Apr 12 - Apr 26	1	45	24	1.2	30
Cruise 5	May 5 - May 11	22	27	24	1	18
Cruise 6	Jun 10 - Jun 22	-4	15	0	4.2	26
Cruise 7	Jul 6 - Jul 19	-10	37	3	3.3	38

Table A.1: Summaries of automated Certified Reference Material tests aboard the *Bigelow* during cruises in 2017. The CRM used was Batch 159 (TA 2213.59 µmol kg^{-1} and salinity 33.572, Dickson et al. 2003). Plots of individual CRM tests are shown in Appendix A Figure A.1. The offset was calculated as the certified TA concentration subtracted from the measured TA value, and thus positive values indicate an overestimate of the CRM TA by the HydroFIA TA instrument.

Table A.2: Data sources used to compile the ‘Historical’ East Coast TA dataset described in this work.

Filename	region	source/link
33GG20130609_BT.csv	Gulf of Maine, Georges Bank, Mid-Atlantic Bight	https://www.aoml.noaa.gov/ocd/gcc/shortcruises/GU1302/GU1302-Discrete.csv
33GG20131114_BT.csv	Gulf of Maine, Georges Bank, Mid-Atlantic Bight	https://www.aoml.noaa.gov/ocd/gcc/shortcruises/GU1305/GU1305-Discrete.csv
33GG20140301_GU1401_hy1.csv	Gulf of Maine, Georges Bank, Mid-Atlantic Bight	https://www.aoml.noaa.gov/ocd/gcc/shortcruises/GU1401/GU1401-Discrete.csv
33GG20151012-GU1506-data.xlsx	Gulf of Maine, Georges Bank, Mid-Atlantic Bight	https://www.aoml.noaa.gov/ocd/gcc/shortcruises/GU1506/33GG20151012-GU1506-data.xlsx
33GG20160521-GU1608-data.xls	Gulf of Maine, Georges Bank, Mid-Atlantic Bight	https://www.aoml.noaa.gov/ocd/gcc/shortcruises/GU1608/33GG20160521-GU1608-data.xls
33GG20160521-GU1608-data.xls	Gulf of Maine, Georges Bank, Mid-Atlantic Bight	https://www.aoml.noaa.gov/ocd/gcc/shortcruises/GU1608/33GG20160521-GU1608-data.xls
33GG20170516_GU1701_GU1702_data.xls	Gulf of Maine, Georges Bank, Mid-Atlantic Bight	http://www.aoml.noaa.gov/ocd/gcc/shortcruises/GU1701/33GG20170516-GU1701-data.csv

33GG20170610-GU1702-data.csv	Gulf of Maine, Georges Bank, Mid-Atlantic Bight	http://www.aoml.noaa.gov/ocd/gcc/shortcruises/GU1702/33GG20170610-GU1702-data.csv
33GG20171031-GU1706-data.csv	Gulf of Maine, Georges Bank, Mid-Atlantic Bight	http://www.aoml.noaa.gov/ocd/gcc/shortcruises/GU1706/33GG20171031-GU1706-data.csv
33GG20180822-GU1804-data.csv	Gulf of Maine, Georges Bank, Mid-Atlantic Bight	http://www.aoml.noaa.gov/ocd/gcc/shortcruises/GU1804/33GG20180822-GU1804-data.csv
33HH20140902-HB_1405-data.csv	Gulf of Maine, Georges Bank, Mid-Atlantic Bight	https://www.aoml.noaa.gov/ocd/gcc/shortcruises/HB1103/Bigelow_1103-Discrete-Web.csv
Bigelow_1103-Discrete-Web.csv	Gulf of Maine, Georges Bank, Mid-Atlantic Bight	https://www.aoml.noaa.gov/ocd/gcc/shortcruises/HB1103/Bigelow_1103-Discrete-Web.csv
33HH20120531-HB1202-data.csv	Gulf of Maine, Georges Bank, Mid-Atlantic Bight	https://www.aoml.noaa.gov/ocd/gcc/shortcruises/HB1202/33HH20120531-HB1202-data.csv
33HH20130314-HB1301-data.xlsx	Gulf of Maine, Georges Bank, Mid-Atlantic Bight	https://www.aoml.noaa.gov/ocd/gcc/shortcruises/HB1301/33HH20130314-HB1301-data.xlsx
33HH20140902-HB_1405-data.csv	Gulf of Maine, Georges Bank, Mid-Atlantic Bight	https://www.aoml.noaa.gov/ocd/gcc/shortcruises/HB1405/33HH20140902-HB_1405-data.csv
33HH20150519-HB1502-data.csv	Gulf of Maine, Georges Bank, Mid-Atlantic Bight	https://www.aoml.noaa.gov/ocd/gcc/shortcruises/HB1502/33HH20150519-HB1502-data.csv
33HH20170210-HB1701-data.xls	Gulf of Maine, Georges Bank, Mid-Atlantic Bight	https://www.aoml.noaa.gov/ocd/gcc/shortcruises/HB1701/33HH20170210-HB1701-data.xls

33HH20180523-HB1803-data.csv	Gulf of Maine, Georges Bank, Mid-Atlantic Bight	http://www.aoml.noaa.gov/ocd/gcc/shortcruises/HB1803/33HH20180523-HB1803-data.csv
33H520181102-S11802-data.csv	North Atlantic	https://www.aoml.noaa.gov/ocd/gcc/shortcruises/Delaware_II_1202/Delaware_1202-Discrete-Web.csv
46SL20181115-Transit846-data.csv	North Atlantic	http://www.aoml.noaa.gov/ocd/gcc/shortcruises/Selfoss/46SL20181115-Transit846-data.csv
Reykjafoss_2010-Discrete-Web.csv	North Atlantic	https://www.aoml.noaa.gov/ocd/gcc/shortcruises/Reykjafoss_2010/Reykjafoss_2010-Discrete-Web.csv
PC1207-Discrete.csv	Mid Atlantic	https://www.aoml.noaa.gov/ocd/gcc/shortcruises/PC1207/PC1207-Discrete.csv
PC1405-Discrete.csv	Mid Atlantic	https://www.aoml.noaa.gov/ocd/gcc/shortcruises/PC1405/PC1405-Discrete.csv
PC1607-PC1609-data.xls	Mid Atlantic	https://www.aoml.noaa.gov/ocd/gcc/shortcruises/PC1607_PC1609/PC1607-PC1609-data.xls
MLCE-EQUINOX-2015-2016-Data.csv	Mid Atlantic	https://www.aoml.noaa.gov/ocd/gcc/shortcruises/EQNX_2015_2016/MLCE-EQUINOX-2015-2016-Data.csv
GOMECC1MasterBottle06212013.xls	East Coast	https://www.aoml.noaa.gov/ocd/gcc/GOMECC1/data.php
GOMECC2_discrete_underway_samples.xlsx	East Coast	https://www.aoml.noaa.gov/ocd/gcc/GOMECC2/GOMECC2_discrete_underway_samples.xlsx
GOMECC2_station_data.xlsx	East Coast	https://www.aoml.noaa.gov/ocd/gcc/GOMECC2/GOMECC2_station_data_version4.xlsx
ECOA2015_Discrete_Underway_Data_Final.xlsx	East Coast	https://www.nodc.noaa.gov/oads/data/0157389.xml
ECOA2015_MasterSamplingSheet_vAlk.xlsx	East Coast	https://www.nodc.noaa.gov/oads/data/0157389.xml
BioChem_Query_1801_Data.csv	Northeast, Canadian Maritimes, Labrador Sea	http://www.dfo-mpo.gc.ca/science/data-donnees/biochem/index-eng.html
bats_bottle.xls	Sargasso Sea	http://batsftp.bios.edu/BATS/bottle/bats_bottle.txt
GLODAP	Atlantic	https://www.nodc.noaa.gov/archive/arc0133/0186803/2.2/data/0-data/
OMP	East Coast	Charles Flagg, Pers. Comm.

APPENDIX B

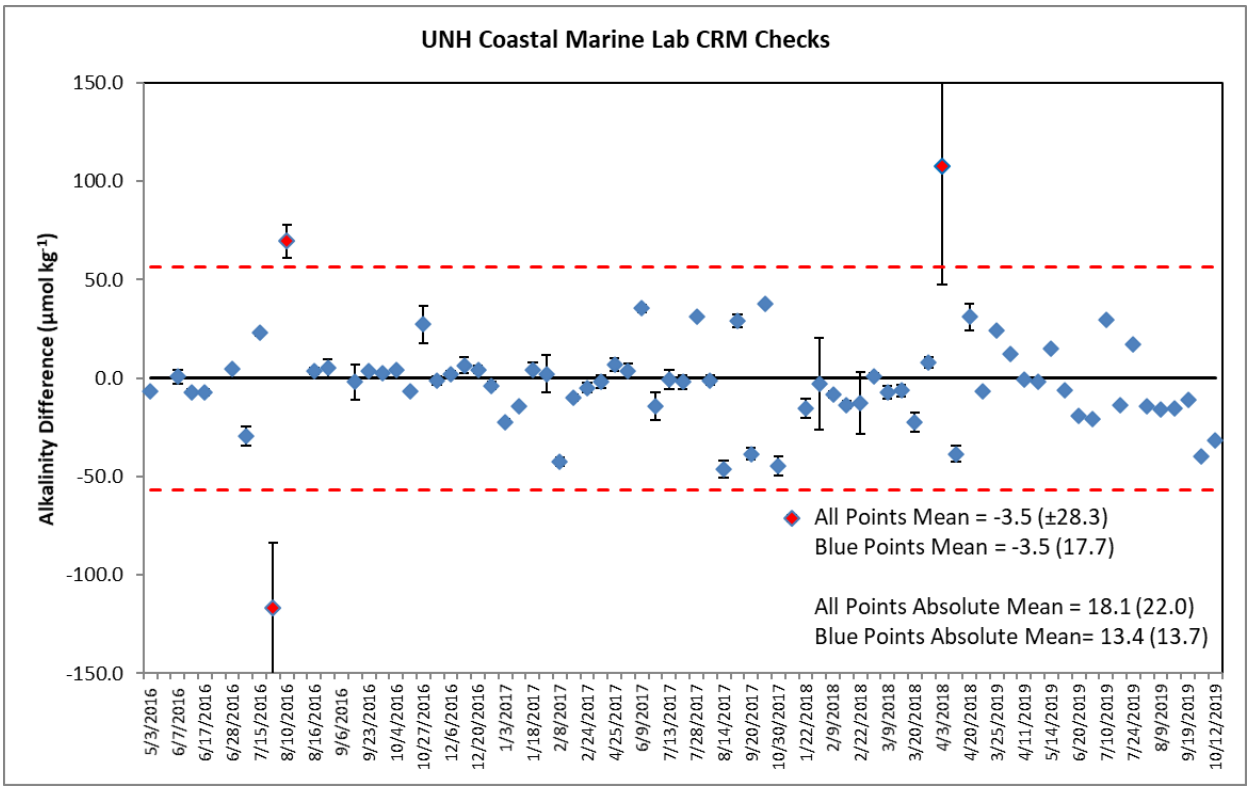

Figure B.1: Differences between measurements of Certified Reference Material at the Coastal Marine Laboratory over the study period and the certified TA. The CRM Batches used were: 124, 125, 151, 156, 159, 162, 163, 164 and 172, with TA ranging from 2213.6-2403.7 µmol kg^{-1}. Horizontal dashed red lines indicate twice the standard deviation of all differences shown (±56.6 µmol kg^{-1}).

	Month	Mean nTA ($\mu mol\ kg^{-1}$)	nTA STD ($\mu mol\ kg^{-1}$)	Mean nDIC ($\mu mol\ kg^{-1}$)	nDIC STD ($\mu mol\ kg^{-1}$)
Jan	1	2071	33	1957	29
Feb	2	2066	26	1955	24
Mar	3	2051	32	1933	29
Apr	4	2018	31	1889	26
May	5	2043	48	1927	46
Jun	6	2068	41	1940	43
Jul	7	2054	46	1922	45
Aug	8	2036	20	1913	24
Sep	9	2046	16	1931	31
Oct	10	2040	23	1929	25
Nov	11	2061	14	1947	13
Dec	12	2060	15	1944	12

Table B.1: Monthly mean nTA and nDIC at CML, with one standard deviation (STD), normalized to a mean dataset salinity of 29.95.

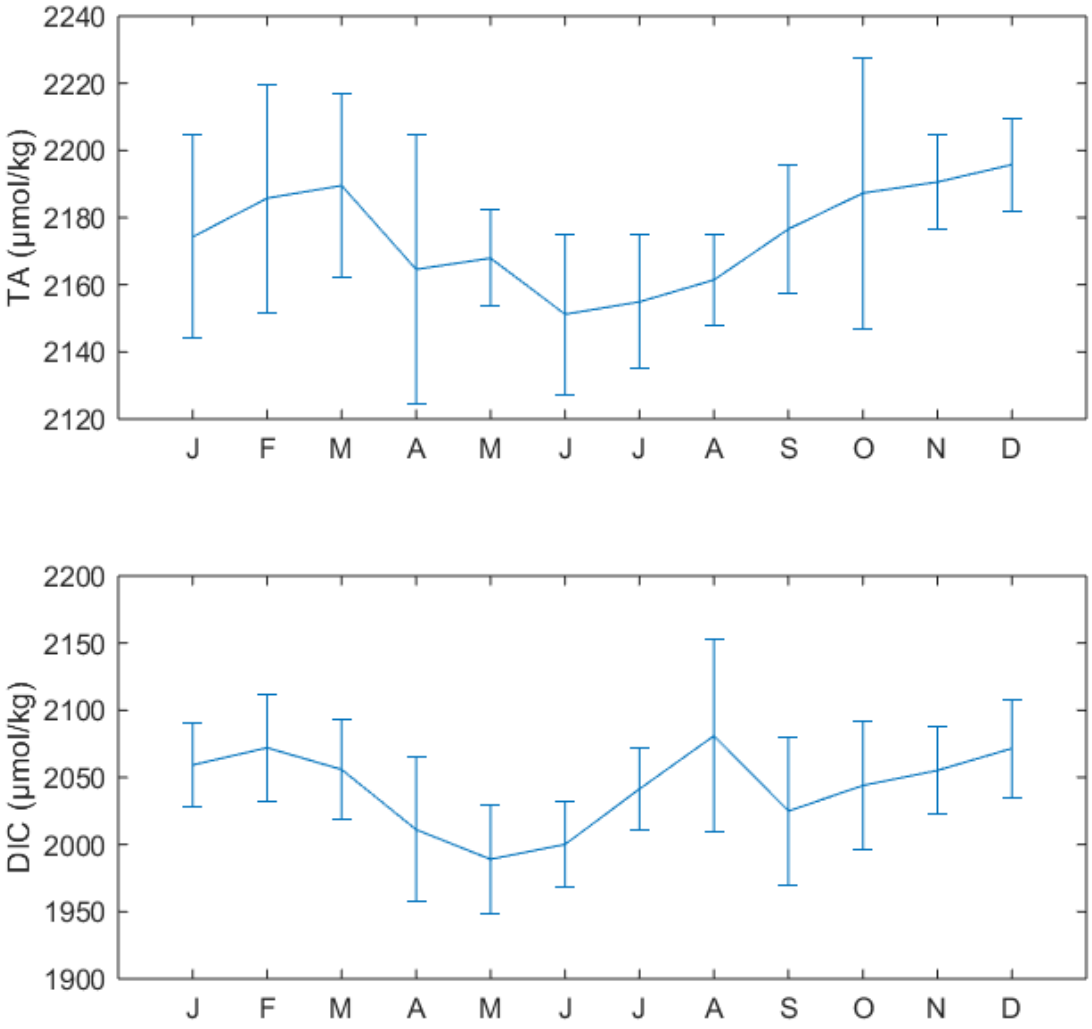

Figure B.2: Monthly mean TA and DIC observed at station WBD, at depths greater than 20m.

Calculation of smoothed climatologies

Smoothed climatologies were prepared according to the following procedure. First, monthly mean values were calculated, incorporating any measurements within a certain month. These mean values were then reproduced twice, to form a 36-month series, repeating annually (see Figure B.2). The Matlab function ‘pchip’ (Mathworks, Natick MA USA) was used to interpolate the monthly means onto a daily time step, and the Matlab function ‘smooth’ was then applied over a 60-day window. The annual climatology was taken as the middle year to avoid smoothing irregularities at the beginning and end of the year.

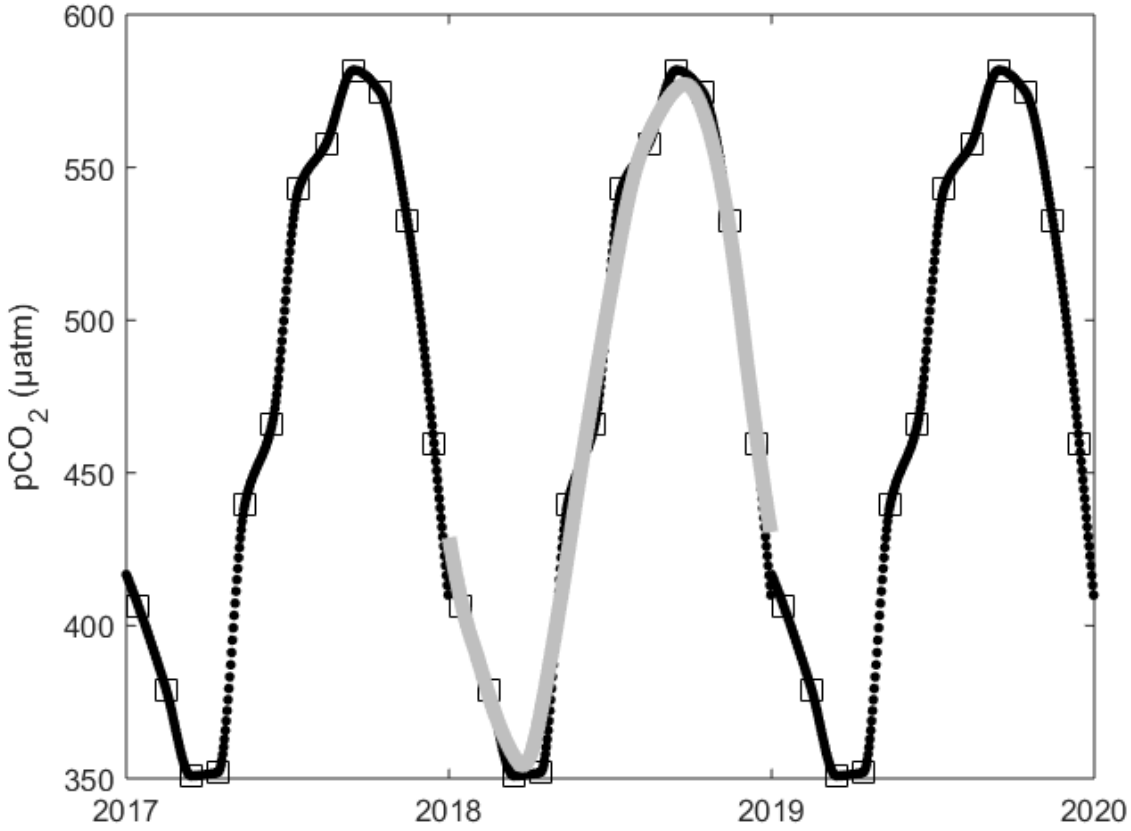

Figure B.3. Example of climatology calculation using pCO_2. Squares are monthly mean values calculated over the entire timeseries (2005-2019). Solid black markers are the interpolated daily values using the ‘pchip’ function. The solid gray line represents the one-year daily climatology of pCO_2 calculated using the ‘smooth’ function on the solid black points.

APPENDIX C

Spectrophotometric Electrode Validation

Briefly, a novel sample holder was constructed from an inert polyetheretherketone (PEEK) block, with a central sample channel and quartz windows on either end, an apparatus derived from the design presented by Easley and Byrne (2012). This sample holder was place in the light path of an Agilent 8454 UV-Vis spectrophotometer. The sample channel was filled with seawater (~100 mL), and a cover, also constructed of PEEK, was placed on top. This cover had openings for the pH electrode, tubing for the addition of mCP, and a stirring apparatus consisting of a small electric motor which stirred the sample with a loop of PEEK tubing. A blank reading of the seawater was taken, and 300 ul mCP was added, followed by simultaneous spectrophotometric pH readings according to Douglas and Byrne (2017) and electrode potential (in mV) readings from the pH electrode. A drop of ~0.1N HCl was added to the sample, and another pair of mCP and electrode readings was recorded. This process continued until 8-10 reading pairs were obtained. The paired spectrophotometric pH and electrode potential readings were used to prepare an electrode calibration curve and resulting electrode response slope.

Preparation and Examination of CO_2-free NaOH Solution

A requirement of OrgAlk measurements is the use of CO_2-free base, typically sodium hydroxide (NaOH), to raise the pH of a titrated sample back to the original, pre-titration

value (e.g., Cai and Wang 1998). This solution should be CO_2-free in order to ensure that no additional carbonate anions are introduced between the first and second titrations. However, the details for preparation of the CO_2-free NaOH have been scarce in the few direct studies of OrgAlk. Cai and Wang (1998) provide no detail; while Yang et al. (2015) describe a test used to quantify the potential trace CO_2 present in their NaOH reagent, they do not describe the actual preparation of the NaOH. Recently, Sharp and Byrne (2021) described a method for the preparation of CO_2-free NaOH; these authors also measured the CO_2 content of their NaOH solution directly, finding a concentration of about 6 nanomoles total inorganic carbon per microliter of NaOH. This translated to a potential CO_2 addition of about 4 µmol kg^{-1} to the titrated sample.

We have adapted the method presented in Sipos et al (2000) for our analyses. Instead of using solid NaOH pellets, which can form sodium carbonate on the surface of the pellets, this method calls for the dilution of a concentrated 50% NaOH solution. At this high concentration, any carbonate forms an insoluble Na_2CO_3 precipitate. To prepare the solution, we filled a Pyrex bottle with distilled/deionized water. A fritted glass tube connected to a tank of ultrapure nitrogen gas was inserted, the top of the bottle sealed with paraffin film, and the water bubbled with nitrogen gas for a minimum of two hours to strip any CO_2 and create a nitrogen headspace in the bottle. Since the concentration of the NaOH solution was not of concern for this method, a 1-mL syringe was filled with the concentrated 50% NaOH solution. A disposable 0.22 µm cartridge filter was then attached to the syringe, followed by a stainless steel needle attached to the filter. The needle was then inserted through the paraffin film, and the 1 mL of 50% NaOH dispensed into the CO_2-free distilled/deionized water. The resulting NaOH solution was

continuously bubbled throughout the analysis to maintain the nitrogen headspace and prevent CO_2 infiltration.

To test the possible addition of CO_3^{2-} from this NaOH solution, a solution of 0.7M NaCl was titrated according to the procedure described in the Methods, resulting in Alk_{Gran2} and $Alk_{3.5}$ values. For three repeated analyses of the NaCl solution, the mean Alk_{Gran2} was -0.1 µmol kg^{-1} (±0.5 µmol kg^{-1}) and the mean $Alk_{3.5}$ was 1.1 µmol kg^{-1} (±0.4 µmol kg^{-1}). Results of this test showed that the NaOH solution may have contributed on the order of 1 µmol kg^{-1} of DIC at the most to the titration of $Alk_{3.5}$, and no detectable alkalinity to the titration of Alk_{Gran2}.